PREPARATION AND CHARACTERIZATION OF CuO_x-BASED PHOTOCATALYST AND NiFeP-BASED ELECTROCATALYST FOR WATER SPLITTING

水分解用 CuO_x 光触媒と NiFeP 電極触媒の製作と特性評価

DEPARTMENT OF ELECTRICAL AND ELECTRONIC ENGINEERING

謝天

March 2020

Abstract

Water splitting for hydrogen evolution is a potential technique to solve the crises of energy shortage and environment pollution. In recent years, this research area has achieved a great progress by the persistent efforts of the researchers.

In this thesis, we reported on two kinds of methods for overall water splitting, include photoelectrochemical water splitting and electrocatalytic water splitting. Solar energy conversion through photoelectrochemical water splitting by semiconductors has becoming one of the most effective ways to solve energy and environmental issues. Electrocatalytic water splitting can be regarded as a promising one for clean energy and renewable. Synthesis of stable and efficient electrocatalysts is paramount importance for hydrogen evolution reaction, and oxygen evolution reaction.

Firstly, the CuO_x composite photocatalyst were deposited on FTO transparent conducting glasses by alternating current magnetron reactive sputtering under different Ar/O_2 ratios. The advantage of this deposited method is that it can deposit a CuO_x photocatalyst uniformly and rapidly with large scale. From the photoelectrochemical properties of these CuO_x photocatalysts, it can be found that the CuO_x photocatalyst with Ar/O_2 30:7 provide a photocurrent density of -3.2 mA/cm^2 under a bias potential -0.5 V (vs. Ag/AgCl), which was found to be twice higher than that of Ar/O_2 with 30:5. A detailed characterization on the structure, morphology and electrochemical properties of these CuO_x photocatalysts were carried out, and it is found that the improved PEC performance of CuO_x photocatalyst with Ar/O_2 30:7 attributed to the less defects in it, indicating that this Ar/O_2 30:7 is an optimized condition for excellent CuO_x photocatalyst fabrication.

Secondly, a CuO_x/WO_3 photocatalyst based on p-n heterojunction proposed as a highly performance and stable photocathode. The CuO_x/WO_3 photocatalyst was deposited by magnetron reactive sputtering layer by layer, followed with slow rate annealing in O_2 ambient. This is an excellent method for high-quality and uniform

composite thin-film deposition with large areas at a high growth rate. The optimized CuO_x/WO_3 photocatalyst after slow rate annealing at 500 °C in O_2 provides an obviously enhanced photoinduced current density of -3.8 mA cm^{-2} at a bias potential of -0.5 V (vs. Ag/AgCl), which value is 1.5 times higher than that of bared CuO_x. This highly enhanced photoelectrochemical performance is attributed to p-n heterojunction, which accelerates the photogenerated electrons and holes transfer to n-WO_3 and p-CuO_x, thereby accelerate the separation of photogenerated carries. In addition, WO_3 layer covered on the surface of CuO_x photocatalyst can improve the stability of Cu_2O in electrolytes.

Lastly, a new highly active and cost-effective nanocomposite electrocatalyst Ni-Fe-P-$FeMnO_3$ supported on nickel foam has been designed and prepared by electroless composite deposition and rapid dealloying. The nanocomposite electrocatalyst Ni-Fe-P-$FeMnO_3$/NF presents a remarkable electrocatalytic activity towards HER, which demands a quite low overpotential of 16.62 mV at -10 mA cm^{-2} current density in 1 M KOH, which behaves better performance than Pt/C noble metal catalysts. Moreover, Ni-Fe-P-$FeMnO_3$/NF electrocatalyst exhibits remarkable OER activity as well, which requires only 297 mV and 219 mV of overpotential at 50 mA cm^{-2} and 10 mA cm^{-2}, respectively. Evidently, its overall water splitting activity used as both anode and cathode performs a low overpotential of 1.63 V to reach 10 mA cm^{-2}. The high performances of the obtained electrocatalyst are mainly due to the unique structure of nano perovskite $FeMnO_3$ as well as the synergistic effect between nickel/iron and phosphorus.

Keywords: Semiconductor; Magnetron reactive sputtering; p-n heterojunction; Photocathode; Nanocomposite; Electroless composite deposition; Perovskite-type oxide; overall water splitting

Outline

Chapter 1: Background of the research

1.1 Background

Due to the rapidly economic development and increasingly serious environmental problems, the energy crisis based on traditional fuels has caused widespread concern. The development of clean, efficient and sustainable energy is an effective method to solve the energy crisis and mitigate environmental pollution. As a zero-emission fuel, hydrogen has the advantages of high energy density and pollution-free from combustion products, it is considered as one of the most important green energy sources. Renewable energy-driven water splitting is a high-purity hydrogen fuel production method with environmental protection prospects. As a result, it is widely regarded as a core clean energy technology critical to hydrogen economy.

Electrocatalytic water splitting method can be regarded as a promising one for clean energy and renewable.[1] Electrocatalysis can divided into electrocatalysis (electrode/solution interface) and photoelectrocatalysis (Fig. 1-1).

(a) Solution-phase Electrocatalysts

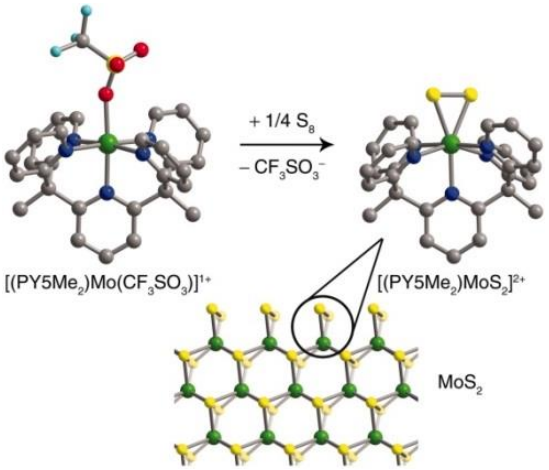

(b) Surface Electrocatalysts

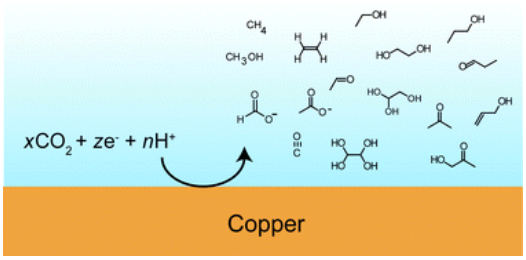

(c) Photocatalysts

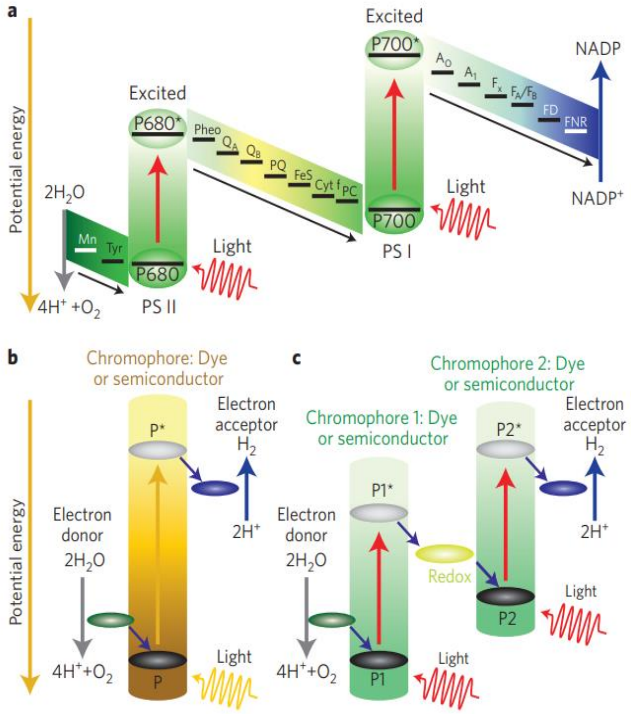

Fig. 1-1 Electrocatalysis comes in different forms: (a) solution-phase electrocatalysts,[2] (b) surface electrocatalysts,[3] (c) photocatalysts.[4]

1.2 Working principle of photoelectrochemical water splitting

1.2.1 Working principle of photoelectrochemical water splitting

Photoelectrochemical (PEC) water splitting for hydrogen evolution is a potential technique to solve the crises of energy shortage and environment pollution.[5] The illustration of traditional PEC water splitting system is shown in Fig. 1-2. The PEC water slitting system includes a photocathode and a cathode. Under light illumination, the photoanode will generate photogenerated electron-hole pairs. The electrons generated on semiconductor conduction band transfer through the external circuit to the counter electrode, and reduce the protons in water to produce hydrogen on the surface of counter electrode. In the electrolyte, the reduction and oxidation reactions occur on the surface of the cathode and anode, respectively. The reaction mechanism shows as

follows:

Photoanode:

$$h\gamma \rightarrow e^- + h$$

$$h + H_2O\ (l) \rightarrow 1/2\ O_2\ (g) + 2H^+$$

Photocathode:

$$2H^+ + 2e^- \rightarrow H_2\ (g)$$

Total reaction:

$$2h\gamma + 2H_2O\ (l) \rightarrow 1/2\ O_2\ (g) + H_2\ (g)$$

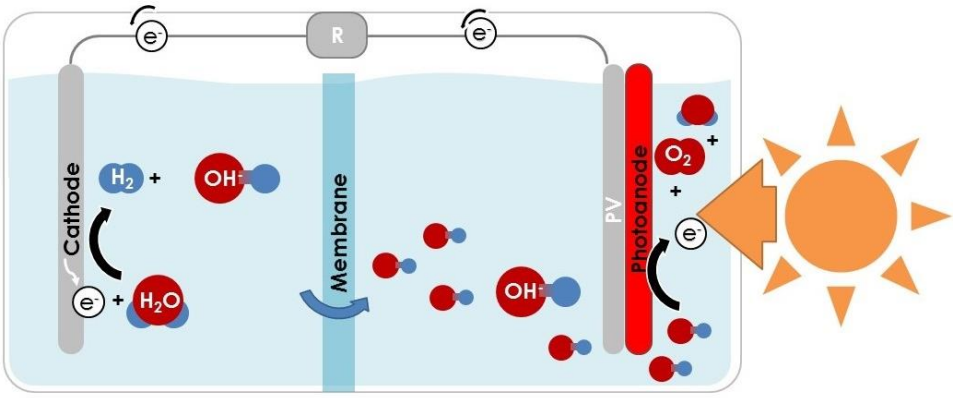

Fig. 1-2 Schematic diagram of PEC water splitting system.

A more extensive illustration of redox reactions occur on the semiconductor surface is shown as Fig. 1-3. The recombination of electron-hole pairs plays a negative role in the photocatalytic process.[6-8] During the PEC water splitting reaction, the photo-generated electron-hole pairs will transfer to the photocatalyst surface and initiate redox reactions.

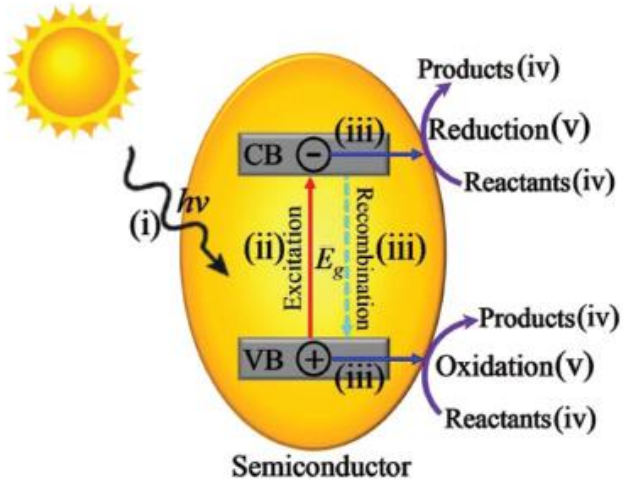

Fig. 1-3 Schematic illustration of typical photocatalytic processes on semiconductor.[9]

1.2.2 Heterojunction system

According to the difference of electron transfer paths between two types of semiconductors, heterojunction system can be divided into p-n heterojunction type and Z-scheme (take the p-n heterojunction type as an example).[10] When two different types of semiconductors (p- or n-type) contact with each other, the energy and positions of two semiconductors will change,[11] thus the electron transfer pathway will be changed. As shown in Fig. 1-4, the n-type semiconductor Fermi level is near the conduction band, and the p-type semiconductor Fermi level is near its valence band. After contact with each other, the p-type semiconductor energy band moves up and the n-type semiconductor energy band moves down, with the diffusion of electrons and holes. When the drift current and the diffusion current offset with each other, a space charge region will be formed near the interface to generate a built-in electric field. Under light illumination, two types of semiconductors are excited at the same time. Under the action of built-in electric field, electrons will transfer to the n-type semiconductor rapidly, while holes will transfer to the p-type semiconductor, simultaneously. This effectively promotes the separation of photo-generated carriers (Fig. 1-4(b)). In addition, in the p-n heterostructure, the photo-generated electrons are enriched on n-type semiconductor conduction band with a higher position (compare

with conduction band position before two types of semiconductors contact), and the photo-generated holes are enriched on p-type semiconductor valence band. As a result, this can not only provide more photo-generated electrons, but also make the photo-generated electrons have strong reduction.

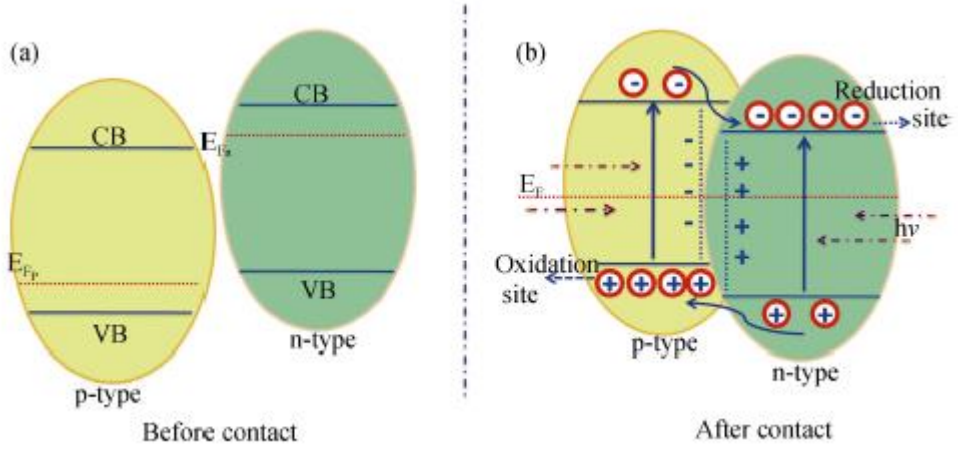

Fig. 1-4 (a) Band alignment of p-type and n-type semiconductors before contact and (b) transportation of the charge carries in p-n type heterostructure.[12]

1.3 Working principle of electrocatalytic water splitting

Electrocatalytic water splitting includes hydrogen reaction evolution (HER) and oxygen reaction evolution (OER), the reaction equations are shown below:

HER (cathode):

$$2H^+ (aq) + 2e^- \rightarrow H_2 (g),\ E^0_{HER} = 0.00\ V$$

OER (anode):

$$2H_2O (l) \rightarrow O_2 (g) + 4H^+ (aq) + 4e^-,\ E^0_{OER} = 1.23\ V$$

Overall:

$$2H_2O (l) \rightarrow O_2 (g) + 2H_2 (g),\ E^0_{overall} = 1.23\ V$$

At standard temperature and pressure, splitting water into hydrogen and oxygen is thermally an ascending reaction. Electrolysis of water requires at least $\Delta G^0 = +237.2$ kJ mol^{-1} standard gibbs free energy, equivalent to $E^0 = 0.00$ V vs. normal hydrogen electrode (NHE). According to Nernst equation, the standard thermodynamic

equilibrium potential of water reduction reaction is E^0_{HER} = 0.00 V, and the standard thermodynamic equilibrium potential of water oxidation reaction is E^0_{OER} = 1.23 V.

However, in the actual process of electrolysis of water, in order to overcome the negative factors, such as high activation energy, hysteresis dynamics and poor energy efficiency, extra energy is required, which is called overpotential. On this basis, the following equation represents the practical application potential of two half-cell reactions:

$$E_{HER} = E^0_{HER} + iR + \eta_{HER}$$

$$E_{OER} = E^0_{OER} + iR + \eta_{OER}$$

Where iR is the ohmic potential drop of the system and n is the overpotential, which directly determines the energy efficiency of the electrolytic cell. The overpotential of HER and OER can be significantly reduced by using active electrocatalysts.[13]

1.3.1 Mechanism analysis of HER in cathode

HER is a half-reaction at the cathode of an electrolytic cell, in which protons (under acidic environment) or water molecules (under alkaline environment) are reduced to hydrogen. HER reaction mechanism under two conditions is shown in Fig. 1-5. The reaction process of HER is Volmer-Heyrovsky mechanism or Volmer-Tafel mechanism, and the specific reaction process is shown is the following equations (the catalytic activity site is expressed as " * "):

In acidic medium:

$$2H^+ + 2e^- \rightarrow H_2\ (g)$$

i. Volmer reaction: protons and electrons combine on the surface of the electrode (proton discharge) to form an adsorbent hydrogen atom.

$$* + H^+ + e^- \rightarrow *H_{ad}$$

ii. Heyrovsky reaction: the electrochemical desorption of hydrogen occurs when the adsorbed hydrogen atom interacts with protons and electrons.

$$*H_{ad} + H^+ + e^- \rightarrow H_2 + *$$

iii. Tafel reaction: coupling of two adsorbed hydrogen atoms produces hydrogen desorption.

$$2*H_{ad} \rightarrow H_2 + 2*$$

In alkaline medium:

$$2H_2O + 2e^- \rightarrow H_2\,(g) + 2OH^-$$

i. Volmer reaction: Due to the large amount of OH^-, H_2O will be coupled with electrons to form an adsorbed hydrogen atom on the surface of the electrode.

$$* + H_2O + e^- \rightarrow *H_{ad} + OH^-$$

ii. Heyrovsky reaction: The adsorbed hydrogen atoms are then combined with H_2O and electrons to cause electrochemical desorption of hydrogen.

$$*H_{ad} + H_2O + e^- \rightarrow H_2 + * + OH^-$$

iii. Tafel reaction: Two adsorbed hydrogen atoms are coupled and hydrogen desorption occurs.

$$2*H_{ad} \rightarrow H_2 + 2*$$

In HER reaction under acidic and alkaline media, the adsorption of hydrogen starts from the Volmer reaction, and the desorption of hydrogen can be carried out by Heyrovsky reaction or Tafel reaction.[14-15]

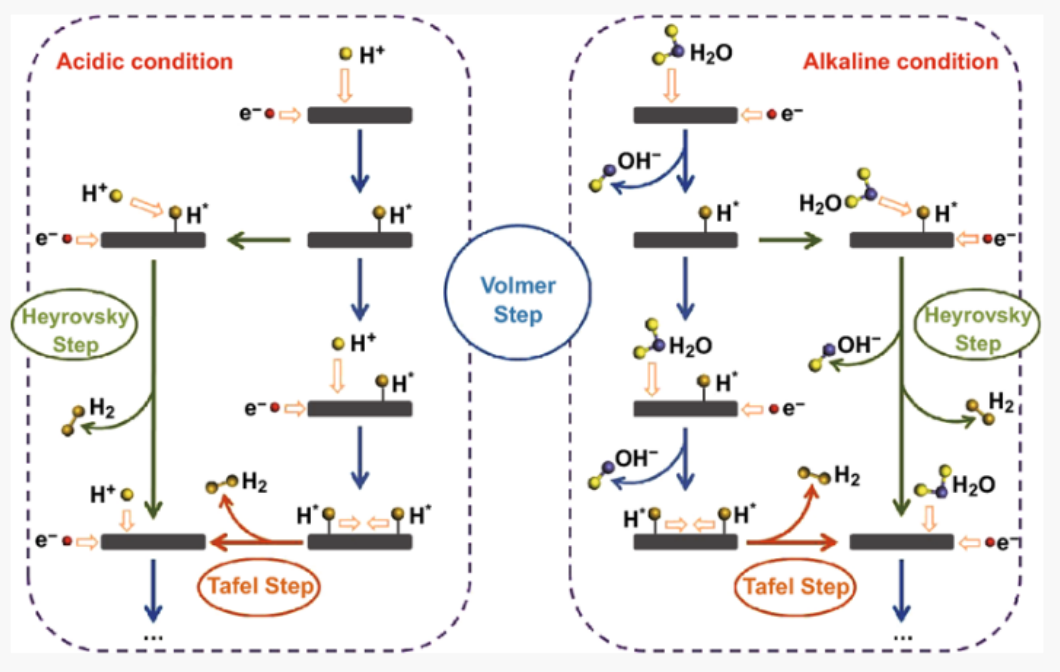

Fig. 1-5 Schematic pathways for HER under acidic and alkaline conditions.[16]

1.3.2 Mechanism analysis of OER in anode

OER kinetics is also a multi-electron charge transfer process in both acidic and alkaline media. In general, the electrochemical reaction occurs at the anode is as follows:

In acidic medium:

$$2H_2O \rightarrow 4H^+ + 4e^- + O_2\ (g)$$

In alkaline medium:

$$4OH^- \rightarrow 2H_2O + 4e^- + O_2\ (g)$$

The OER reaction in both electrolytes involves four electron transfer and deprotonation of water molecules or hydroxide ions. However, the actual reaction mechanism and reaction pathway are more complicated, and single electron transfer is performed in multiple steps. Although the exact mechanism of electron transfer is not well understood, it is generally believed that a basic approach to four-step electron transfer is the best explanation by far, the specific steps are as follows (M stands for the surface active center of the catalyst):

In acidic medium:

$$M + H_2O\ (l) \rightarrow MOH + H^+ + e^-$$

$$MOH + OH^- \rightarrow MO + H_2O\ (l) + e^-$$

$$MO \rightarrow 2M + O_2\ (g)$$

$$MO + H_2O\ (l) \rightarrow MOOH + H^+ + e^-$$

$$MOOH + H_2O\ (l) \rightarrow M + O_2\ (g) + H^+ + e^-$$

In alkaline medium:

$$M + OH^- \rightarrow MOH$$

$$MOH + OH^- \rightarrow MO + H_2O\ (l)$$

$$2MO \rightarrow 2M + O_2\ (g)$$

$$MO + OH^- \rightarrow MOOH + e^-$$

$$MOOH + OH^- \rightarrow M + O_2\ (g) + H_2O\ (l)$$

Fig. 1-6 shows the OER reaction mechanism in different media. The blue line indicates the OER reaction carried out in acidic electrolyte, and the red line indicates the OER reaction mechanism in alkaline electrolyte, both including M-OH and M-O intermediates. The green line produces O_2 through a direct combination of two M-O intermediates, and the black line includes the formation of M-OOH intermediate, which is subsequently decomposed into O_2. The effect of the interaction of all bonds in the intermediate (M-OH, M-O M-OOH) on the electrocatalytic performance is critical during the complex OER reactions. In alkaline electrolyte, first, a hydroxyl radical is adsorbed at the active center, OH^- is oxidized and loses an e^- to obtain M-OH. The protons in M-OH are coupled with electrons to obtain M-O. In addition, OH^- initiates nucleophilic attack on M-OOH and OH^- is oxidative coupled with an e^- to form M-OOH intermediate. Then protons are coupled and electrons are transferred to release O_2 and free active centers.[17]

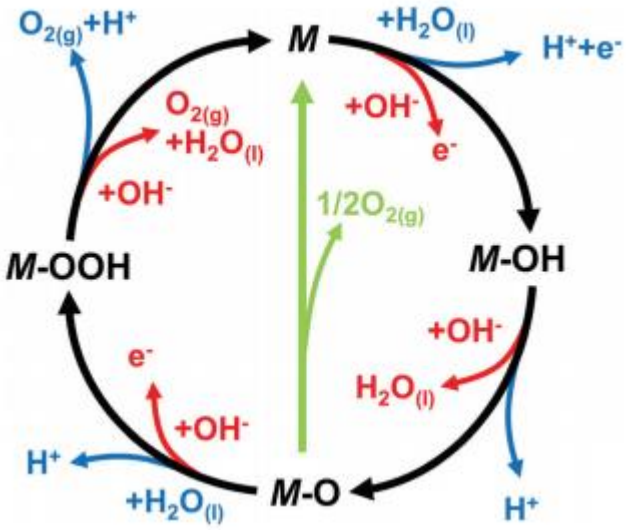

Fig. 1-6 The OER mechanism for acid (blue line) and alkaline (red line) conditions. Two routes of OER: (a) black line indicates that the process involves the formation of a peroxide (M-OOH) intermediate; (b) green line indicates that the direct reaction of two adjacent oxo (M-O) intermediates to produce molecular oxygen.[18]

1.4 Progress research of water splitting

In the recent years, researchers reported on hydrogen production of earth-abundant metal catalysts have exploded. Many researches focused on the construction of heterogeneous interfaces of catalysts, regulation of atoms and electrons. C.-H. Yan used NiS_2 two-dimensional nanosheets and introduced transition metal to construct the nanosheet structure of "M-NiS2".[19] The structure of sulfides was optimized by ions-induced synthesis, interfacial construction and atomic arrangement control, thereby improving the HER catalytic performance. J.-S. Hu has designed the Ni/NiO nano-heterogeneous interface as alkaline HER bicomponent active sites,[20] the regulation of active sites ratios on the reaction steps of hydrogen evolution elementary reaction and its effect on catalytic activity were studied, indicating that the bicomponent active sites need to be balanced to achieve efficient alkaline hydrogen evolution. Q. Yu et al. have deposited two-dimensional TaS_2 on different carriers by chemical vapor deposition,[21] and studied the influence of interfacial lattice mismatch effect, charge transfer effect between catalysts and carriers on the catalytic performance.

It is demonstrated that proper interfacial lattice mismatch and charge transfer are beneficial to improve the HER performance of TaS_2.

1.5 Reference

[1] Z. W. Seh, J. Kibsgaard, C. F. Dickens, I. Chorkendorff, J. K. Nørskov, T. F. Jaramillo, Combining theory and experiment in electrocatalysis: Insight into materials design. Science 355 (2017) 4998-5003.

[2] H. I. Karunadasa, E. Montalvo, Y. Sun, M. Majda, J. R. Long, C. J. Chang, A molecular MoS_2 edge site mimic for catalytic hydrogen generation. Science 335 (2012) 698-702.

[3] K. P. Kuhl, E. R. Cave, D. N. Abram, T. F. Jaramillo, New insights into the electrochemical reduction of carbon dioxide on metallic copper surfaces. Energy Environ. Sci. 5 (2012) 7050-7059.

[4] Y. Tachibana, L. Vayssieres, J. R. Durrant, Artificial photosynthesis for solar water-splitting. Nat. Photonics 6 (2012) 544-518.

[5] J. Cen, Q. Wu, M. Liu, A. Orlov, Developing new understanding of photoelectrochemical water splitting via in-situ techniques: A review on recent progress. Green Energy & Environment 2 (2017) 100-111.

[6] F. E. Osterloh, Inorganic materials as catalysts for photochemical splitting of water. Chem. Mater. 20 (2007) 35-54.

[7] Y. Qu, X. Duan, Progress, challenge and perspective of heterogeneous photocatalysts. Chem. Soc. Rev. 42 (2013) 2568-2580.

[8] A. Kubacka, M. Fernández-García, Gerardo Colón, Advanced nanoarchitectures for solar photocatalytic applications. Chem. Rev. 112 (2011) 1555-1614.

[9] J. Low, J. Yu, M. Jaroniec, S. Wageh, A. A. Al-Ghamdi, Heterojunction photocatalysts. Adv. Mater. 29 (2017) 1601694.

[10] P. Zhou, J. Yu, M. Jaroniec, All-solid-state Z-scheme photocatalytic systems. Adv.

Mater. 26 (2014) 4920-4935.

[11] D. Jiang, L. Chen, J. Zhu, M. Chen, W. Shi, J. Xie, Novel p–n heterojunction photocatalyst constructed by porous graphite-like C_3N_4 and nanostructured BiOI: Facile synthesis and enhanced photocatalytic activity. Dalton Trans. 42 (2013) 15726-15734.

[12] C. Han, Y.-P. Lei, Y.-D. Wang, Recent progress on nano-heterostructure photocatalysts for solar fuels generation. J. Inorg. Mater. 30 (2015) 1121-1130.

[13] X. Li, X. Hao, A. Abudula, G. Quan, Nanostructured catalysts for electrochemical water splitting: Current state and prospects. J. Mater. Chem. A 4 (2016) 11973-12000.

[14] D. Kong, J. J. Cha, H. Wang, H. R. Lee, Y. Cui, First-row transition metal dichalcogenide catalysts for hydrogen evolution reaction. Energy Environ. Sci. 6 (2013) 3553-3558.

[15] S. Anantharaj, S. R. Ede, K. Sakthikumar, K. Karthick, S. Mishra, S. Kundu, Recent trends and perspectives in electrochemical water splitting with an emphasis on sulfide, selenide, and phosphide catalysts of Fe, Co, and Ni: A review. ACS Catal. 6 (2016) 9068-8097.

[16] J. Wei, M. Zhou, A. Long, Y. Xue, H. Liao, C. Wei, Z. J. Xu, Heterostructured electrocatalysts for hydrogen evolution reaction under alkaline conditions. Nano-Micro Lett. 10 (2018) 75.

[17] R. L. Doyle, M. E. G. Lyons, Kinetics and mechanistic aspects of the oxygen evolution reaction at hydrous iron oxide films in base. J. Electrochem. Soc. 160 (2013) H142-H154.

[18] N.-T. Suen, S.-F. Hung, Q. Quan, N. Zhang, Y.-J. Xu, H. M. Chen, Electrocatalysis for the oxygen evolution reaction: Recent development and future perspectives. Chem. Soc. Rev. 46 (2017) 337-365.

[19] J. Yin, J. Jin, H. Zhang, M. Lu, Y. Peng, B. Huang, P. Xi, C.-H. Yan, Atomic arrangement in metal-doped NiS_2 boosts the hydrogen evolution reaction in alkaline media. Angew. Chem. 131 (2019) 18849-18855.

[20] L. Zhao, Y. Zhang, Z. Zhao, Q.-H. Zhang, L.-B. Huang, L. Gu, G. Lu, J.-S. Hu, L.-J. Wan, Steering elementary steps towards efficient alkaline hydrogen evolution via size-dependent Ni/NiO nanoscale heterosurfaces. Natl. Sci. Rev. (2019)

[21] Q. Yu, Y. Luo, S. Qiu, Q. Li, Z. Cai, Z. Zhang, J.Liu, C. Sun, B. Liu, Tuning the hydrogen evolution performance of metallic 2D tantalum disulfide by interfacial engineering. ACS Nano 13 (2019) 11874-11881.

Chapter 2: Preparation of CuO_x composite photocatalyst

2.1 Background

Photoelectrochemical (PEC) water splitting for hydrogen evolution is a potential technique to solve the crises of energy shortage and environment pollution.[1] In recent years, this research area has achieved a great progress by the persistent efforts of the researchers. Related studies indicated that the methods to improve the overall solar-to-hydrogen efficiency in PEC devices mainly include: (1) obtaining better light absorption by engineering the absorber layer morphology of semiconductors;[2-3] (2) improving charge transfer efficiency of the semiconductors by establishing microstructure or nanostructure;[4-5] (3)improving the heterogeneous reaction kinetics by attaching catalysts to the photoelectrodes surfaces;[6-7] (4) protecting the semiconductors from corrosion by building surface passivation layers;[8-9] (5) reducing the rate of electrons-holes recombination by surface state passivation[10] or surface catalyst layers.[11]

2.1.1 Research progress of copper oxide

Copper oxide is considered as one of the most promising photocatalytic materials for water splitting owing to its cost-effective and abundant resources.[12] Yang et al. prepared a Cu_2O/CuO bilayered composite photocathode by electrodeposition and thermal oxidation methods, this photocathode achieved a 3.15 mA cm^{-2} hydrogen evolution reaction photocurrent at a bias potential of 0.4 V (vs. RHE).[13] Cu_2O is a typical p-type semiconductor material, its direct bandgap is approximately 2.0 eV,[14] which has a high corresponding theoretical photocurrent and a high efficiency of light converts to hydrogen.[15] Compared with these hot research visible light responsive PEC materials, such as Ta_2N_3,[16] $BiVO_4$,[17-18] WO_3,[19-20] and Fe_2O_3,[21-22] etc., Cu_2O shows better cost-performance and higher theoretical maximum PEC water splitting

conversion efficiency, it is highly deemed as a potential industry applications material of PEC water splitting. And the conduction band potential of Cu_2O is much negative than the water reduction potential (as shown in Fig. 2-1), the photogenerated electrons can reduce water to hydrogen smoothly. However, the valence band potential of Cu_2O is just near the water oxidation potential, so that the water oxidation process is difficult to drive by this small over potential. Simultaneously, its poor stability and fast carrier recombination rate also limits the photoelectrochemical performance of Cu_2O.[23]

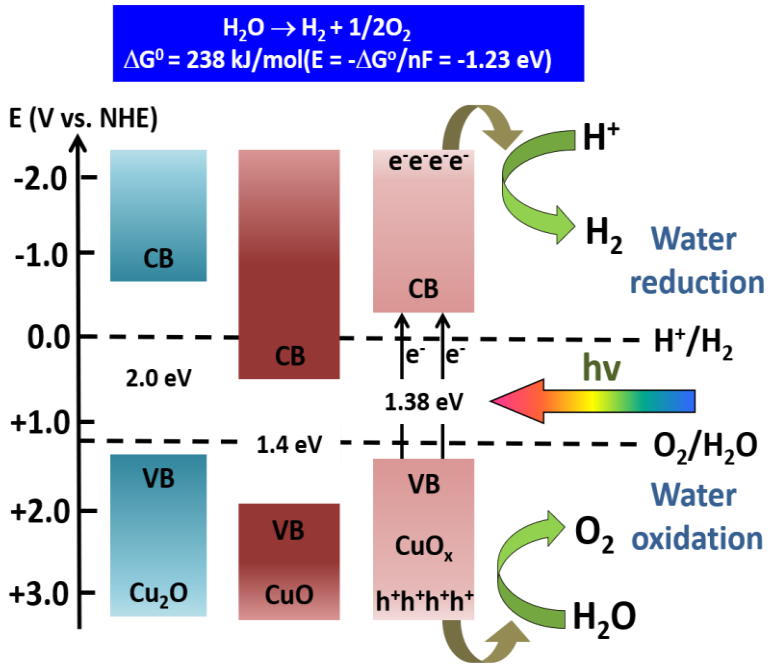

Fig. 2-1 Band diagram of mixed valence copper oxide system.

2.1.2 CuO_x composite photocatalyst

Consider of compounding Cu_2O with other semiconductors, such as CuO,[24-25] which can provide a much positive valence potential and then improve the water oxidation process. CuO is another semiconductor in copper oxide group. It is a kind of p-type semiconductor with a direct bandgap of 1.4 eV,[26] so that the light response range of CuO is much larger than that of Cu_2O, corresponding to a higher PEC performance than that of Cu_2O in theory. In addition, CuO has strong absorption under ultraviolet,[27] which widens the absorption spectra of Cu_2O.[28] Copper oxide

photocatalyst can be prepared by several methods at present, such as magnetron sputtering,[29] sol-gel,[12] metal organic chemical vapor deposition,[30] electrochemical deposition.[31] Among these methods, magnetron sputtering is a simple and easy-to-control deposition method, which can be scaled up to mass-produced for industrial applications.[32] The photocatalyst prepared by magnetron sputtering is uniform and the properties of the photocatalyst can be reproducible.

2.1.3 Deposition methods for composite photocatalyst

Currently, several deposition methods have been utilized to synthesize photocatalyst, such as magnetron reactive sputtering, electrochemical deposition, chemical vapor deposition, pulsed laser deposition, sol-gel, and spray-pyrolysis technology. Compared with these methods, the advantage of thin-film deposition by magnetron reactive sputtering is that it can simply deposit high-quality and uniform thin-film with large areas at a high speed, and the properties of the sputtered photocatalyst can be reproducible.

2.1.4 The motivation and outline of this research

In this study, we report on the PEC performance of CuO_x photoelectrodes prepared by AC magnetron reactive sputtering. The electrochemical properties of the CuO_x photoelectrodes were characterized by electrochemical impedance spectroscopy (EIS), Mott-Schottky and PEC performance measurement. Scanning electron microscope (SEM), X-ray diffraction (XRD), Raman spectrum, X-ray photoelectron spectroscope (XPS) and UV-Vis diffuse reflectance spectrum were utilized to characterize the structures and morphologies of the CuO_x photocatalysts.

2.2 Experimental section

2.2.1 Preparation of CuO_x photocatalyst

FTO glasses (1.2 cm×1.0 cm) were ultrasonically cleaned with ethanol and acetone (1:1) mixed solutions for 5 min firstly, then ultrasonically cleaned with ultrapure water for 5 min, and blow-dried with N_2. The CuO_x s were prepared by AC magnetron reactive sputtering at room temperature in Ar and O_2 ambient, using a target metal of copper. During the process of sputtering, the deposition chamber was pumped down to a pressure of 2×10^{-5} Pa. The target was cleaned by a pre-sputtering in Ar gas atmosphere for 5 min, then followed by a second pre-sputtering with Ar and O_2 mixture ambient for 3 min. In this experiment, the sputtering power was fixed at 30 W, and the Ar gas flow was fixed at 30 sccm. The O_2 gas flow was adjusted from 5 sccm to 9 sccm, in order to analyze the effects of Ar/O_2 gas ratio on PEC performance of the products. The thickness of the CuO_x photocatalyst is approximately 220 nm. After deposition, use a conductive sliver tape to connect copper wires with the conductive parts of FTO glasses. And after the conductive tape dried, isolated the exposed conductive parts of FTO glasses with parafilm (as shown in Fig. 2-2).

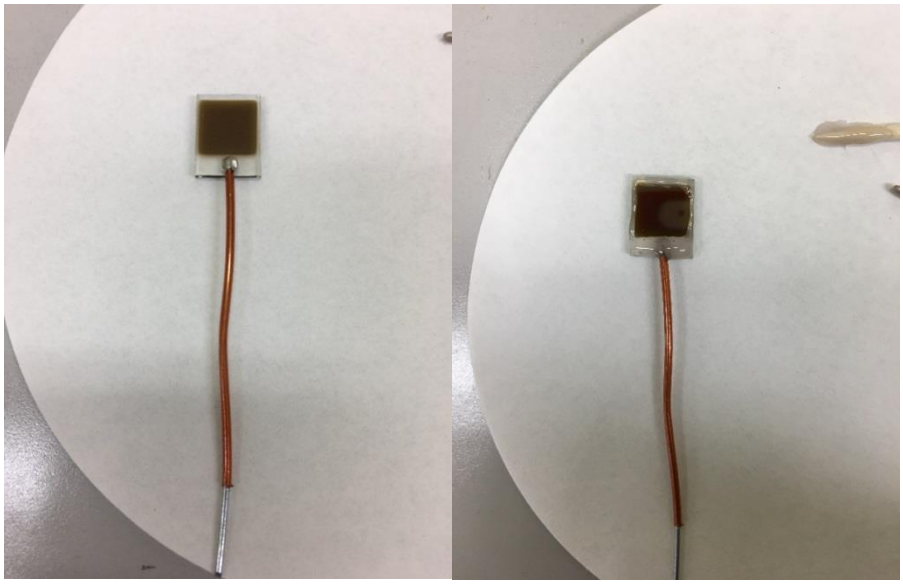

Fig. 2-2 Main steps of PEC photocathode connection.

2.2.2 Characterization of CuO_x photocatalyst

The microstructures of the products were characterized by X-ray diffraction (X'Pert Powder, PANalytical B.V., Almelo, The Netherlands), scanning electron microscope (JSM-6700F, JEOL, Tokyo, Japan), and Raman spectrum (STR-500, Cornes Technologies LTD., Tokyo, Japan). X-ray photoelectron spectroscopy (PHI 5000 Versa Probe, 2ULVAC-PHI, Chigasaki, Japan) was utilized to investigate the element composition, the element chemical and electronic state of the products. Whereas their light absorption capabilities were analyzed by UV-Vis diffuse reflectance spectrophotometer (U-2600, SHIMADZU Co., Kyoto, Japan).

The Photoelectrochemical test was performed on CHI660D Electrochemical Workstation (Shanghai Chenhua Instrument Co., Ltd., Shanghai, China). In which, using a three-electrode system, the prepared CuO_x photocatalyst (1 cm^2), Pt sheet and Ag/AgCl (saturated KCl) electrode were acted as the working electrode, counter electrode and reference electrode, respectively. The three-electrode was immersed into 0.1 mol/L Na_2SO_4 electrolyte solutions. The incident light is from 300 W Xe lamp light source (PLS-SXE300, Beijing bofeilai Technology Co., Ltd., Beijing, China) with a light intensity adjusted to 200 mW/cm^2. The photoinduced current with potential was tested from 0.5 V to -0.5 V (vs Ag/AgCl) with a scan rate of 0.02 V/s, and the photoinduced I-V curve was performed during light on and off in turns with one second respectively. The electrochemical impedance spectroscopy test was measured with frequency range from 10^6 to 10^{-1} Hz, and an AC voltage magnitude of 5 mV, under dark state. Mott-Schottky plots had potential scanning range of -0.5 V to 0.5 V with frequency of 10 Hz and an AC voltage magnitude of 10 mV.

2.3 Results and discussion

2.3.1 Structure and morphology of CuO_x photocatalyst

XRD patterns of the CuO_x photocatalysts are shown in Fig. 2-3. The diffraction patterns for the CuO_x photocatalysts have nine broad peaks at 30.4°, 32.5°, 36.4°, 43.2°, 46.3°, 48.7°,58.3°,74.1° and 77.3° corresponding to Cu_2O (110), CuO (110), Cu_2O (111), Cu (222), CuO (-112), CuO (-202), CuO (202), Cu (220) and Cu_2O (222), respectively. The crystal system of Cu_2O and CuO can be confirmed to be cubic and monoclinic. The XRD results show that the Cu_2O (111), CuO (-200) and Cu_2O (222) crystal planes develop on the photocatalyst Ar/O_2 30:7, and the Cu (111) and Cu (220) crystal planes develop on the CuO_x photocatalysts Ar/O_2 30:5 and 30:6. The CuO (110) and (202) crystal planes widely develop on the photocatalyst Ar/O_2 30:5, due to the decrease of O_2 gas flow. The XRD results indicate that a mixture of cuprite (Cu_2O) and tenorite (CuO) was produced under different atmosphere.

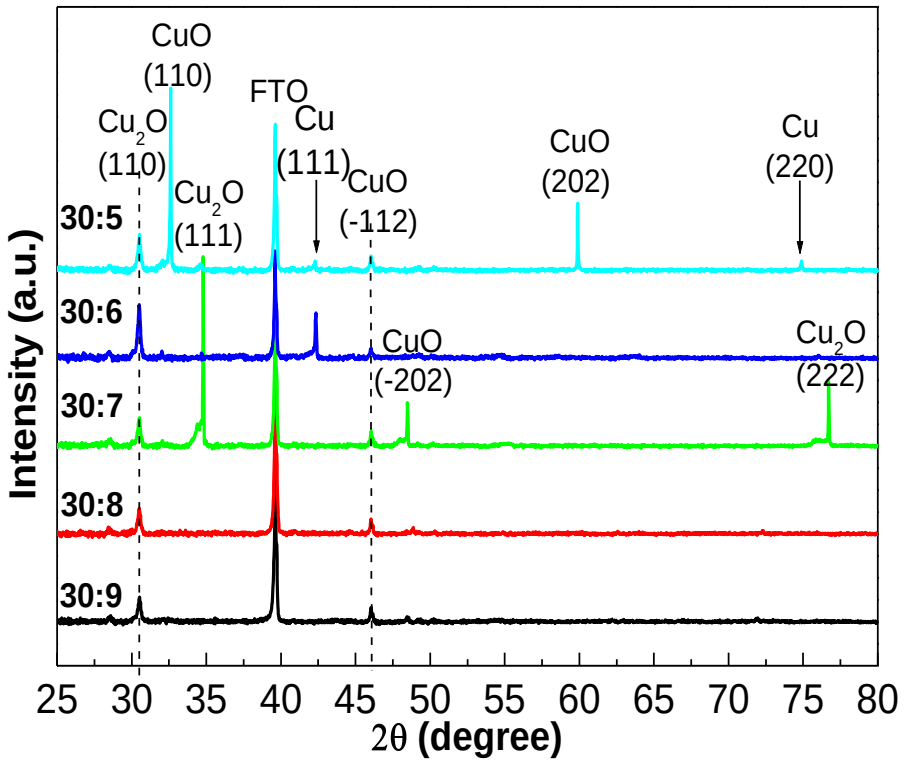

Fig. 2-3 XRD patterns of CuO_x composite with different Ar/O_2 ratios.

Fig. 2-4 shows the SEM images of the top views of the CuO_x photocatalyst. Fig. 2-4a to Fig. 4-4e shows the morphologies of the CuO_x photocatalysts surfaces in a lower magnification. As we can see from Fig. 2-4a and Fig. 2-4b, the CuO_x photocatalysts consist of low crystallinity roughly 100 nm in diameter. With the increase of Ar/O_2, the CuO_x particles grow to 150 nm in diameter, and seem to higher crystallinity, as shown in Fig. 2-4c to Fig. 2-4e. To study the microstructure of the CuO_x particles under high Ar/O_2 ratios, we recorded SEM images in a higher magnification. As we can see form Fig. 2-4f to Fig. 2-4h, it clearly shows the cubic shapes of the CuO_x particles, indicating that with the increase of Ar/O_2, the CuO_x turns to higher crystallinity, finally forms cubic shapes. According to the results, the as-deposited photocatalysts were quite evenly distributed on the surface of the FTO glasses, and crack was not found on the CuO_x surfaces.

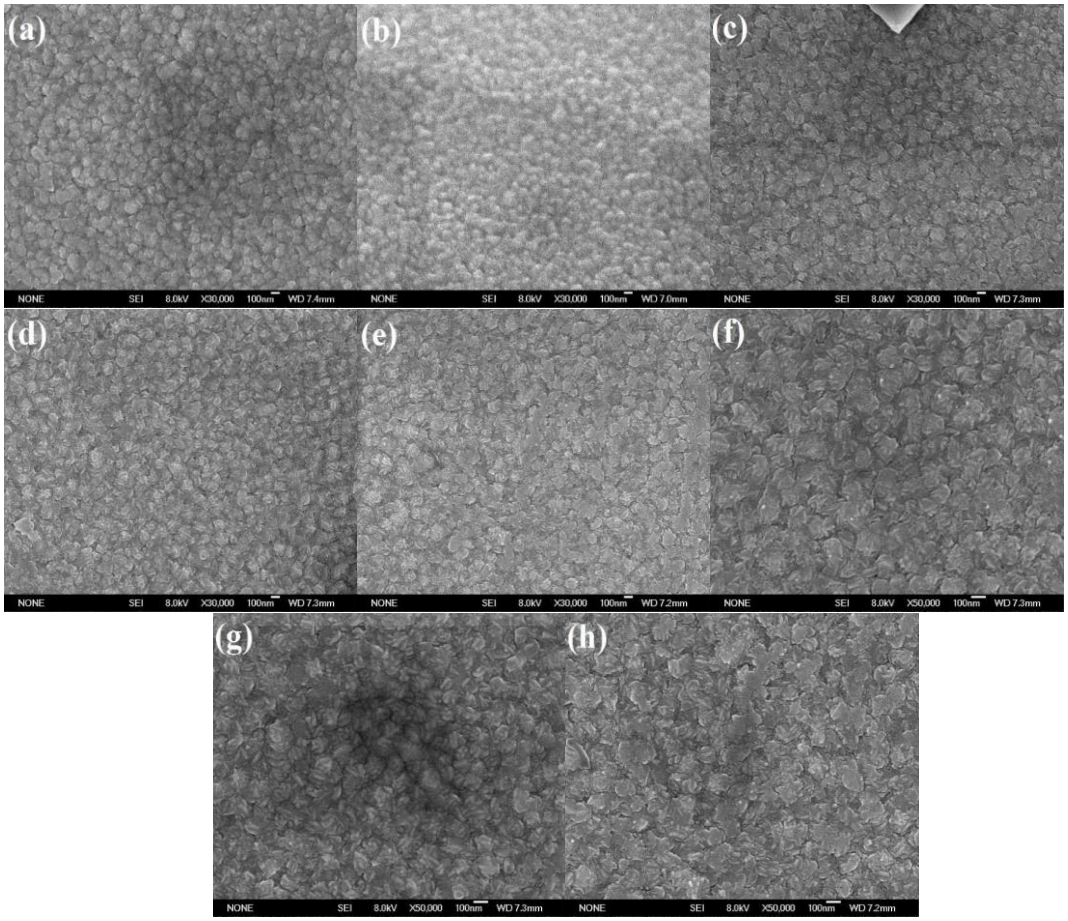

Fig. 2-4 Typical SEM images of the CuO_x photocatalysts with Ar/O_2 (a) 30:5 (×30,000), (b) 30:6 (×30,000), (c) 30:7 (×30,000), (d) 30:8 (×30,000), (e) 30:9 (×30,000), (f) 30:7 (×50,000), (g) 30:8 (×50,000), (h) 30:9 (×50,000).

Fig. 2-5 shows the Raman spectra of CuO_x photocatalysts. As we can see from the Raman spectra, a weak peak at 217 cm^{-1} and a stronger peak at 294 cm^{-1} belong to Cu_2O and CuO. It is difficult to notice the weak peak of Cu_2O at 217 cm^{-1}, demonstrating the content of CuO is higher than Cu_2O synthesized in these samples. The results of Raman spectra show that the products of sputtered photocatalysts are Cu_2O and CuO, which are in agreement with the XRD results.

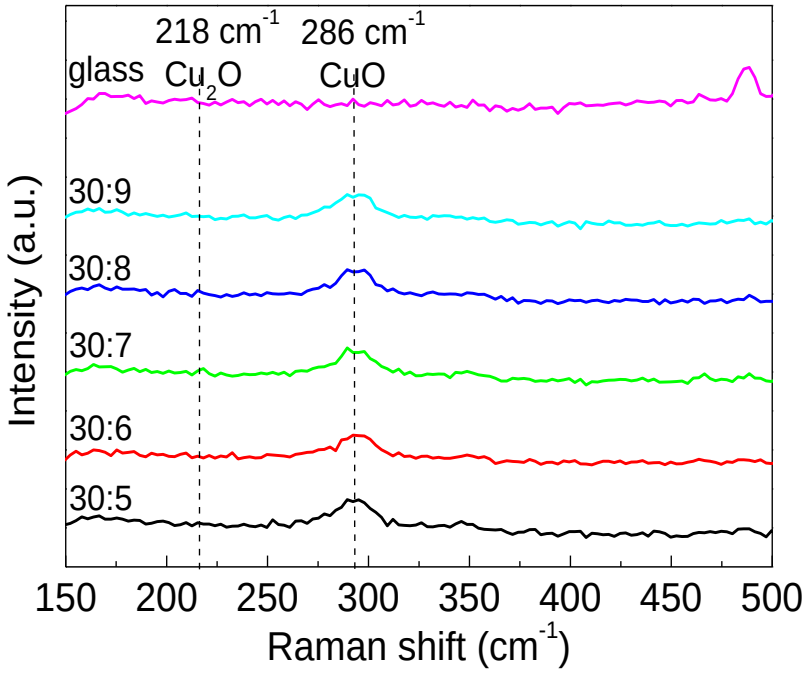

Fig. 2-5 Raman spectra of CuO_x composite with different Ar/O_2 ratios.

2.3.2 XPS and optical characterization of CuO_x photocatalyst

XPS was further used to evaluate the chemical and electronic states of CuO_x photocatalysts. Fig. 2-6 shows the XPS spectra of the CuO_x composite with different Ar/O_2 ratios. As we can see from Fig. 2-6, there is no difference in the shape of the spectrum between these three gas ratios of the samples. The total survey spectrum is shown in Fig. 2-6A, scans of the prepared where performed in a binding energy range from 0 to 1100 eV. Fig. 2-6B and Fig. 2-6C show the XPS spectra of Cu 2p and O 1s, where peaks at 932.9 eV and 952.8 eV represent the characteristic peaks of Cu $2p_{3/2}$ and Cu $2p_{1/2}$, indicating that Cu element existed in the form of Cu^{2+} in the compound.

The strong Cu^{2+} satellite peaks at 943.7 eV and 962.2 eV indicate that the main component of these photocatalysts is Cu^{2+}. 529.6 eV represents the O 1s characteristic peak. These results disclose that most of the products prepared by magnetron reactive sputtering are CuO, which are consistent with the results of Raman spectra.

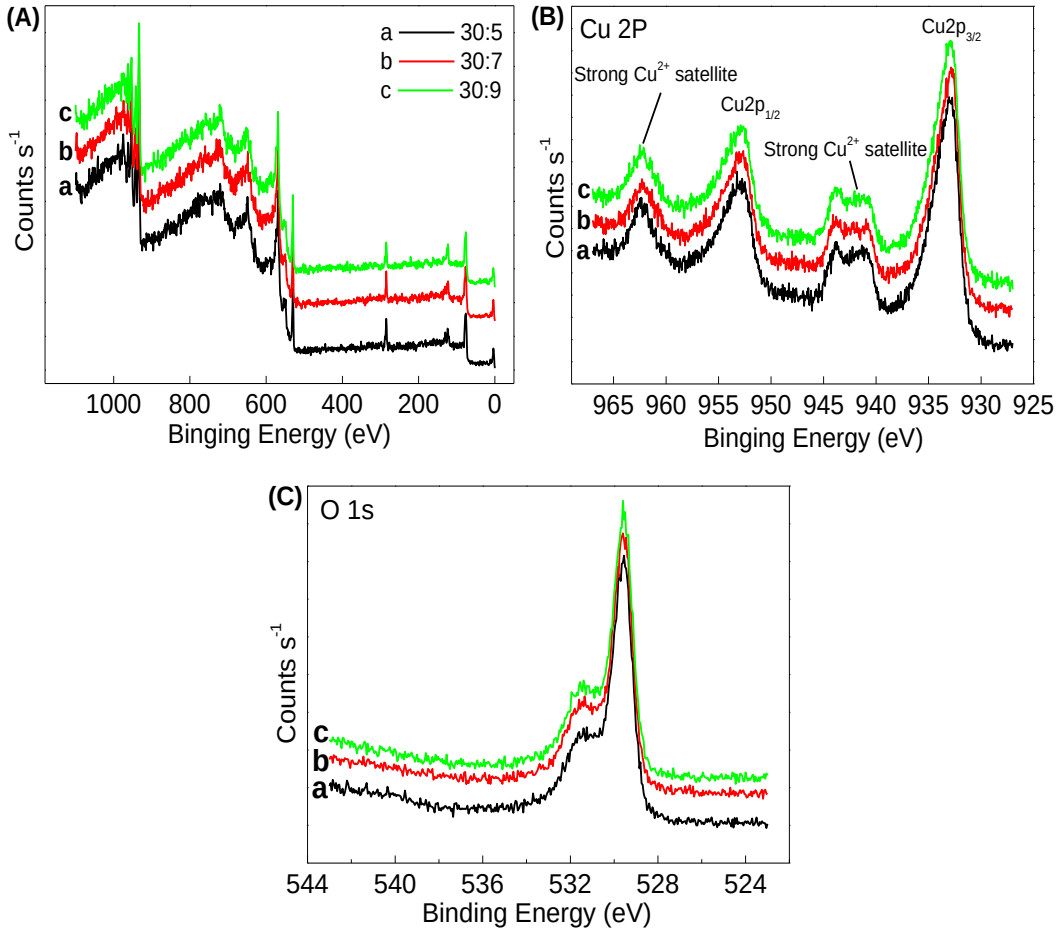

Fig. 2-6 XPS spectra of CuO_x composite with different Ar/O_2 ratios. (A) Wide scan result; (B) Cu 2p; (C) O 1s.

The UV-Vis absorption spectra of CuO_x photocatalysts are shown in Fig. 2-7 The absorption wavelength of the CuO_x photocatalysts can be calculated by the intercept of the tangent and wavelength axis. According to Fig. 2-7d and Fig. 2-7e, the absorption wavelength is 490 nm and 590 nm, respectively, indicating that the CuO_x photocatalysts possessed the ability to respond to visible light. However, the light absorptions of the samples are not strong in the visible light region. Fig. 2-7a to Fig. 2-7c show that the absorption wavelength is 880 nm, and the light absorptions of these

photocatalysts are very strong in the whole wavelength range. It can be seen that the optical absorption intensity of CuO_x is obviously lower with the increase of O_2 gas flow. The UV/Vis results indicate that the CuO_x photocatalysts under lower O_2 gas flow (Ar/O_2=30:5, 30:6, 30:7) have strong light absorption capability in the whole wavelength range (ultraviolet and visible light region).

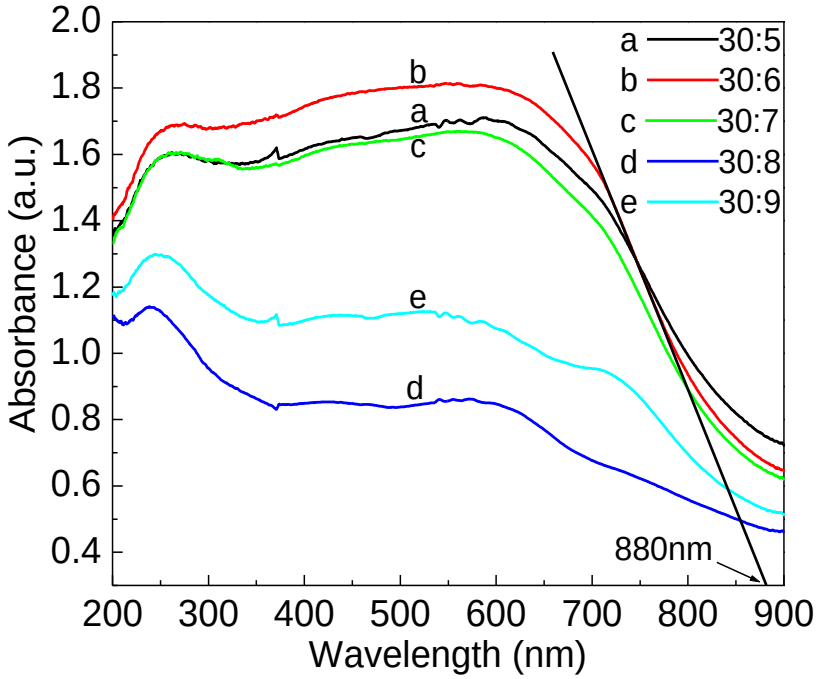

Fig. 2-7 UV-Vis absorption spectra of CuO_x composite with different Ar/O_2 ratios.

2.3.3 PEC performance of CuO_x photocatalyst

Fig. 2-8A to Fig. 2-8E. As shown in Fig. 2-8A and Fig. 2-8B, compared with these CuO_x photocatalysts, the impedance arc of the 30:7 CuO_x photocatalyst increased dramatically, indicating that the 30:7 CuO_x photocatalyst has strong semiconductor properties. In addition, the impedance arc of the 30:5 and 30:6 CuO_x photocatalysts are very small, it can be declared that 30:5 and 30:6 CuO_x photocatalysts have metalloid properties, that means there is a small amount of Cu in the sputtered products of these photocatalysts. Because of the huge change of the EIS data, different fit circuits should be employed to simulate different CuO_x photocatalysts. The corresponding fit circuits and fit data are shown in Fig. 2-8C to Fig. 2-8E,

respectively. In Fig. 2-8C, R_{sol} was the solution resistance; R_t and C_t were the resistance and capacitance of electrons transfer in the photocatalysts; CPE_{ss} was constant phase angle element. R_{ss} was used to describe the charge transfer resistance between the semiconductor and the electrolyte interface. The fit circuits show a good simulation of the EIS curve of CuO_x photocatalysts as shown in Fig. 2-8C to Fig. 2-8E. Table 1-1 shows the corresponding fit data, in which two key parameters R_t and R_{ss} are 5.206×10^3 and 42.25 Ω cm^{-2}. Fig. 2-8D shows the fit circuit and fit data of the CuO_x photocatalyst at 30:6, compared with Fig. 2-8C, a C_{ss} was used to replace CPE_{ss}, and CPE_t was used to replace C_t. As shown in Table 1-1, the R_t and R_{ss} are 1.077×10^{-4} and 33.31 Ω cm^{-2}. Fig. 2-8E shows the fit circuits and fit data of the CuO_x photocatalysts at 30:7, 30:8 and 30:9. Compared with Fig. 2-8C, C_{ss} was used to replace CPE_{ss}, R_t and R_{ss} are shown in Table 1. Compared with these values, we can find the R_t of CuO_x photocatalyst at 30:5 increased near 10^7 orders of magnitude than that of other CuO_x photocatalysts. Meanwhile, the R_{ss} of CuO_x photocatalysts at 30:7 and 30:8 increased 100 orders of magnitude than that of other photocatalysts.

Fig. 2-8F shows the Mott-Schottky plots of the CuO_x photocatalyst photoelectrodes in 0.1 M Na_2SO_4 under dark condition. According to the Mott-Schottky plots shown in Fig. 2-8F, both of the CuO_x photocatalysts exhibit the characteristics of p-type semiconductors. Mott-Schottky is a mathematical equation (as shown in followed equation), which describes the relationship between the capacitance of semiconductor space charge layer and the applied potential.

$$\frac{1}{C^2} = \frac{2}{\varepsilon\varepsilon_0 q N_q} \cdot (E - E_{fb} - \frac{kT}{q})$$

where C is the capacitance of semiconductor space charge layer, ε is the relative permittivity of the semiconductor, ε_0 is the permittivity of vacuum (8.85×10^{-14} F·cm^{-1}), q is the elemental charge (electron is +e, hole is -e, $e=1.602\times10^{-19}$ C), N_q is the carrier concentration, E_{fb} is the flat band potential, E is the applied potential, k is the Boltzmann constant ($k=1.38\times10^{-23}$ J/K), and T is the temperature. According to the

negative tangent slopes in Fig. 2-8F, all of the CuO_x photoelectrodes exhibited the characteristics of p-type semiconductors. According to the Equation above, $\frac{1}{C^2}$ and E is linear relation, the carrier concentration can be obtained from the tangent slope, and the flat band potential of the semiconductor material can be got by the intercept of the tangent and the potential axis. The flat band potential of the CuO_x photoelectrode at 30:5 is approximately 0.69V (vs. Ag/AgCl), after the increasing of Ar/O_2 ratio, the flat band potentials of the CuO_x photoelectrodes are negatively shifted to 0.61, 0.64 and 0.66V, respectively. According to the Equation, the negative shift of the tangent slope will increase the carrier concentration, therefore, improving the photoelectrochemical performance of the CuO_x photoelectrodes.

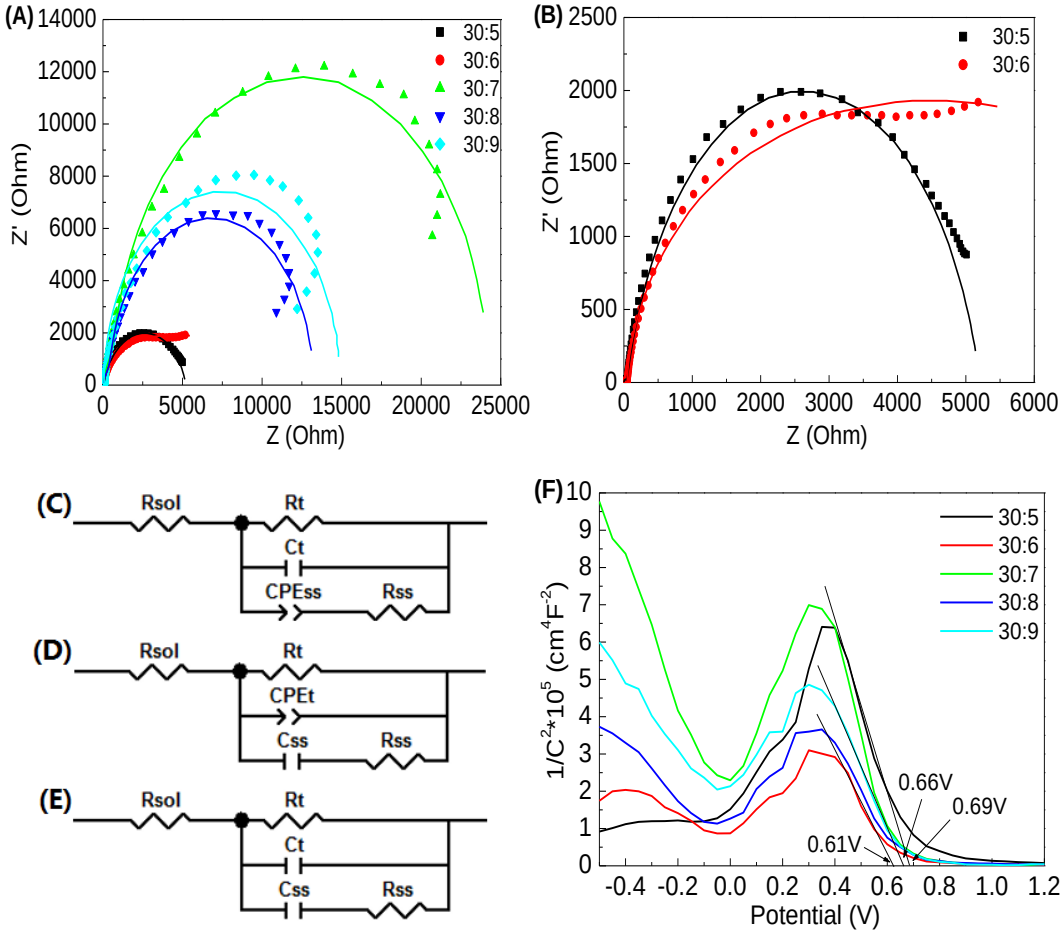

Fig. 2-8 (A) EIS spectra of CuO_x photocatalysts under different Ar/O_2 ratios in 0.1M Na_2SO_4 electrolyte. (B) Enlarged view of 30:5 and 30:6. (C) The fit circuit of 30:5 EIS curves. (D) The fit circuit of 30:6 EIS curves. (E) The fit circuit of 30:7, 30:8 and 30:9 EIS curves. (F) Mott-Schottky plots of CuO_x composite with different Ar/O_2 ratios.

Table 2-1 Fitted parameters of the EIS of CuOx photocatalysts based on the circuits shown in Fig. 7C-7E.

Sample	R_{sol} [Ω cm^2]	R_t [Ω cm^2]	CPE [Ω^{-1} cm^2 sn]	n	C_t [F cm^{-2}]	C_{ss} [F cm^{-2}]	R_{ss} [Ω cm^2]
30:5	1.706	5.206×10^{3}	1.23×10^{-5}	0.8361	7.696×10^{-8}	-	42.25
30:6	21.4	1.077×10^{-4}	1.051×10^{-4}	0.3935	-	1.004×10^{-5}	33.31
30:7	54.32	2.417×10^{-4}	-	-	4.173×10^{-6}	3.52×10^{-6}	2797
30:8	45.48	1.316×10^{-4}	-	-	5.956×10^{-6}	6.309×10^{-6}	1420
30:9	14.74	1.489×10^{-4}	-	-	8.921×10^{-9}	7.812×10^{-6}	53.1

The photoinduced volt-ampere characteristic curve (i-V curve) of CuO_x photocatalyst photoelectrodes are shown in Fig. 2-9A. Current-potential characteristics in 0.1 M Na_2SO_4 solution, under chopped AM 1.5 light illumination to study the photoelectrochemical response. The photoinduced current with potential was tested from 0.5 V to -0.5 V (vs Ag/AgCl) with a scan rate of 0.02 V/s, and the photoinduced I-V curve was performed during light on and off in turns with one second respectively. The cathodic photocurrent feature of the photocatalysts confirmed that the CuO_x is p-type, which agreed with those from the results of Mott-Schottky. The photoinduced current densities of these photoelectrodes start at approximately 0.2 V and increase with the negative shift of the bias potential. The CuO_x photocatalyst with Ar/O_2 30:7 generated a photoinduced current density of -3.2 mA/cm^2 at the bias potential of -0.5 V vs RHE, which was about twice that of the Ar/O_2 30:5. However, the photoinduced current densities become lower with the increase of O_2 gas flow after Ar/O_2=30:7. The results show that the most suitable Ar/O_2 ratio is 30:7 for the photoelectrochemical performance. The Incident photon-to-current conversion Efficiency (IPCE) results of the CuO_x with Ar/O_2 30:5, 30:7 and 30:9 were showed in Fig. 2-9B. The IPCE values of all samples decline rapidly since the wavelength larger than 700 nm, and terminate near 900 nm. In addition, CuO_x 30:7 photocatalyst shows the highest IPCE value in all photo response range, which value is near twice higher than CuO_x 30:5 and 1.5 times higher

than CuO_x 30:9, respectively. The photoinduced i-t curve of the well-defined CuO_x photocatalyst photoelectrode (Ar/O_2 30:7) is shown in Fig. 2-9C. The bias potential for measuring the i-t curve is 0 V. According to the i-t curve, the CuO_x with Ar/O_2 30:7 photoelectrode is stable under the bias potential of 0 V. In addition, a negative current peak appeared after turning on the light, demonstrating that there are some defects in the CuO_x photoelectrode. The formation of the strong current peak is due to an instantaneous photoelectron charging process. Compare with the SEM images (the insets of Fig. 2-9C) of the CuO_x photoelectrode before and after i-t test, the morphologies of the CuO_x have some varieties, indicating that CuO_x has a certain degree of corrosion in the process of i-t measurement. Therefore, we decided to make a protective layer coating on the surface of the CuO_x to protect it from corrosion in the future.

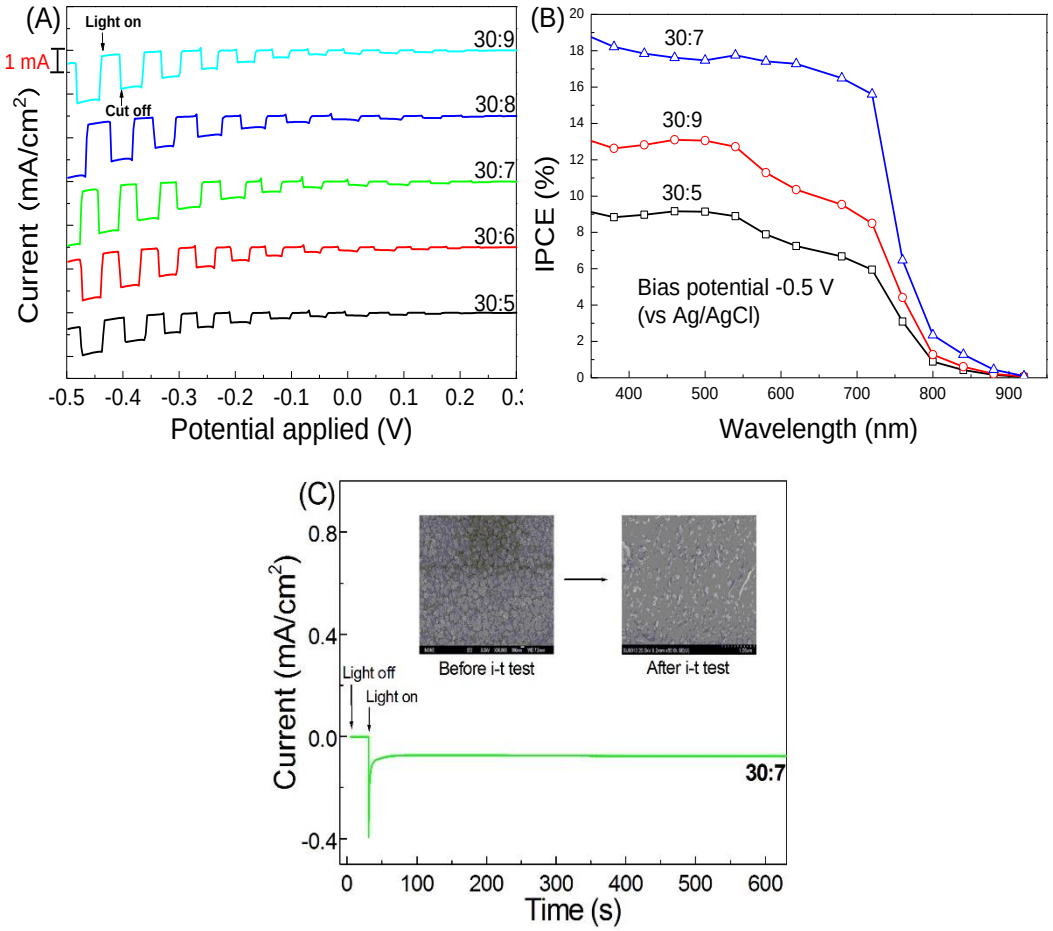

Fig. 2-9 (A) The photoinduced volt-ampere characteristic curve (i-V curve), (B) the Incident Photon-to-current conversion Efficiency (IPCE) results, (C) the photoinduced i-t curve (the

insets show the SEM images of the CuO_x photocatalyst photoelectrode before and after i-t test) of the CuO_x photocatalyst photoelectrode.

2.4 Principle of the CuO_x system

Fig. 2-10 shows the mechanism of the CuO_x photocatalyst grown on the FTO substrate. Under light illumination, the photovoltaic effect of CuO_x semiconductor material resulted in the generation of electrons and holes. With the extra applied negative bias potential, the conduction band potential of CuO_x will more negative than that of water reduction potential, the photogenerated electrons with strong reduction capacity can shift to the surface of CuO_x photocatalyst and reduce water to hydrogen. The photogenerated holes will transfer to the FTO substrate. On the other hand, the photogenerated electrons from Pt counter will also transfer to the CuO_x photocatalyst, meanwhile, the photogenerated holes will shift to the surface of Pt counter, and finally oxidize water to oxygen.

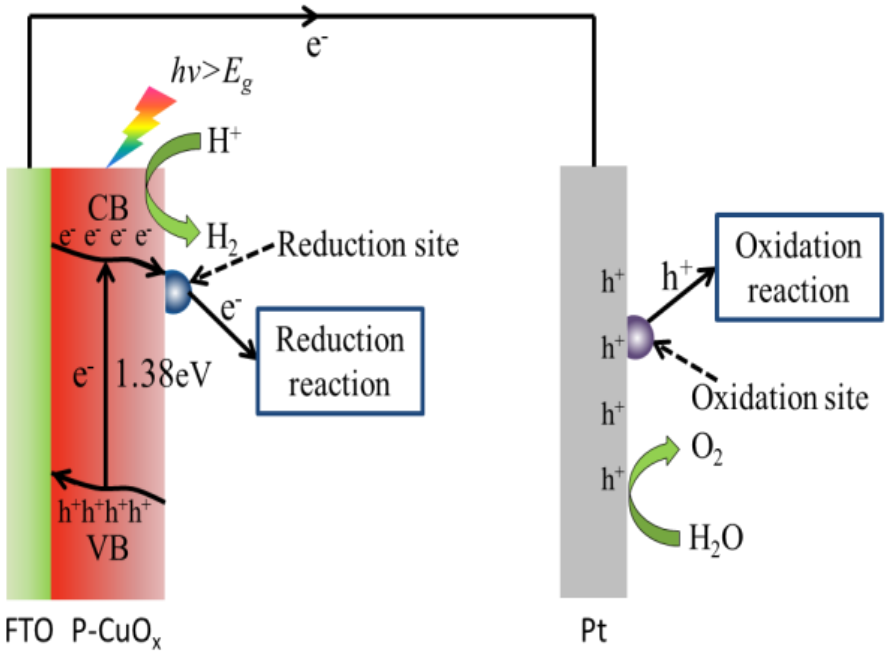

Fig. 2-10 Schematic illustration of the mechanism of the CuO_x photocatalyst

2.5 Conclusion

In summary, the CuO_x photocatalysts with different Ar/O_2 gas ratios were

successfully prepared by magnetron reactive sputtering on the FTO glasses. The deposited products have been demonstrated to be mixtures of Cu_2O and CuO, and the content of CuO is higher than Cu_2O synthesized in these photocatalysts. Compared with different Ar/O_2 gas ratios, the well-defined CuO_x photocatalysts with Ar/O_2 ratio 30:7, are demonstrated to display much better photoelectrochemical performance. Subsequently, UV/Vis diffuse reflectance spectroscopy, EIS, Mott-Schottky tests were carried out. It was found that the CuO_x photocatalysts under lower O_2 gas flows (Ar/O_2=30:5, 6, 7) have strong light absorption capability in ultraviolet and visible light region. The CuO_x photocatalyst under the gas ratio of 30:7 has the biggest impedance value and fewer defects, indicating that the CuO_x photocatalyst under the gas ratio of 30:7 has strong semiconductor properties.

2.6 Reference

[1] J. Cen, Q. Wu, M. Liu, A. Orlov, Developing new understanding of photoelectrochemical water splitting via in-situ techniques: A review on recent progress. Green Energy Environ. 2 (2017) 100-111.

[2] S.K. Mohapatra, S.E. John, S. Banerjee, M. Misra, Water photooxidation by smooth and ultrathin a-Fe_2O_3 nanotubes arrays. Chem. Mater. 21 (2009) 3048-3055.

[3] S.W. Boettcher, J.M. Spurgeon, M.C. Putnam, E.L. Warren, D.B. Turner-Evans, M.D. Kelzenberg, J.R. Maiolo, H.A. Atwater, N.S. Lewis, Energy-conversion properties of vapor-liquid-solid-grown silicon wire-array photocathodes. Science 327 (2010) 185-187.

[4] Y. Lin, S. Zhou, S.W. Sheehan, D. Wang, Nanonet-based hematite heteronanostructures for efficient solar water splitting. J. Am. Chem. Soc. 133 (2011) 2398-2401.

[5] Y. Lin, G. Yuan, S. Sheehan, S. Zhou, D. Wang, Hematite-based solar water splitting: challenges and opportunities. Energy Environ. Sci. 4 (2011) 4862-4869.

[6] B. Klahr, S. Gimenez, F. Fabregat-Santiago, J. Bisquert, T.W. Hamann, Photoelectrochemical and impedance spectroscopic investigation of water oxidation with “Co-Pi”-coated hematite electrodes. J. Am. Chem. Soc. 134 (2012) 16693-16700.

[7] B. Seger, A.B. Laursen, P.C.K. Vesborg, T. Pedersen, O. Hansen, S. Dahl, I. Chorkendorff, Hydrogen production using a molybdenum sulfide catalyst on a titanium-protected n^+p-silicon photocathode. Angew. Chem. Int. Ed. 51 (2012) 9128-9131.

[8] Y.W. Chen, J.D. Prange, S. Du¨hnen, Y. Park, M. Gunji, C.E.D. Chidsey, P.C. Mclntyre, Atomic layer-deposited tunnel oxide stabilizes silicon photoanodes for water oxidation . Nat. Mater. 10 (2011) 539-544.

[9] Y. Bu, J.-P. Ao, A review on photoelectrochemical cathodic protection semiconductor thin films for metals. Green Energy Environ. 2 (2017) 331-362.

[10] F. Le Formal, N. T_etreault, M. Cornuz, T. Moehl, M. Gr€atzel, K. Sivula, Passivating surface states on water splitting hematite photoanodes with alumina overlayers. Chem. Sci. 2 (2011) 737-743.

[11] M. Barroso, A.J. Cowan, S.R. Pendlebury, M. Gr€atzel, D.R. Klug, J.R. Durrant, The role of cobalt phosphate in enhancing the photocatalytic activity of α-Fe_2O_3 toward water oxidation. J. Am. Chem. Soc. 133 (2011) 14868-14871.

[12] Y.F. Lim, C.S. Chua, C.J.J. Lee, D. Chi, Sol-gel deposited Cu_2O and CuO thin films for photocatalytic water splitting. Phys. Chem. Chem. Phys. 16 (2014) 25928-25934.

[13] Y. Yang, D. Xu, Q. Wu, P. Diao, Cu_2O/CuO Bilayered Composite as a high-efficiency photocathode for photoelectrochemical hydrogen evolution reaction. Sci. Rep. 6 (2016) 35158.

[14] C. Li, T. Hisatomi, O. Watanabe, M. Nakabayashi, N. Shibata, K. Domen, J.J. Delaunay, Positive onset potential and stability of Cu_2O-based photocathodes in water splitting by atomic layer deposition of a Ga_2O_3 buffer layer. Energy Environ. Sci. 8 (2015) 1493-1500.

[15] A. Paracchino, V. Laporte, K. Sivula, M. Gr€atzel, E. Thimsen, Highly active oxide photocathode for photoelectrochemical water reduction. Nat. Mater. 10 (2011) 456-461.

[16] G. Liu, S. Ye, P. Yan, F. Xiong, P. Fu, Z. Wang, Z. Chen, J. Shi, C. Li, Enabling an integrated tantalum nitride photoanode to approach the theoretical photocurrent limit for solar water splitting. Energy Environ. Sci. 9 (2016) 1327-1334.

[17] T.W. Kim, K.S. Choi, Nanoporous $BiVO_4$ photoanodes with dual-layer oxygen evolution catalysts for solar water splitting. Science 343 (2014) 990-994.

[18] Y.H. Ng, A. Iwase, A. Kudo, R. Amal, Reducing graphene oxide on a visible-light $BiVO_4$ photocatalyst for an enhanced photoelectrochemical water splitting. J. Phys. Chem. Lett. 1 (2010) 2607-2612.

[19] M. Higashi, R. Abe, T. Takata, K. Domen, Photocatalytic overall water splitting under visible light using $ATaO_2N$ (A=Ca, Sr, Ba) and WO_3 in a IO_3^-/I^- shuttle redox mediated system. Chem. Mater. 21 (2009) 1543-1549.

[20] V. Cristino, S. Caramori, R. Argazzi, L. Meda, G.L. Marra, C.A. Bignozzi, Efficient photoelectrochemical water splitting by anodically grown WO_3 electrodes. Langmuir 27 (2011) 7276–7284.

[21] A. Kay, I. Cesar, M. Gr€atzel, New benchmark for water photooxidation by nanostructured α-Fe_2O_3 films. J. Am. Chem. Soc. 128 (2006) 15714-15721.

[22] K. Sivula, F. Le Formal, M. Gr€atzel, Solar water splitting: Progress using hematite (α-Fe_2O_3) photoelectrodes. ChemSusChem 4 (2011) 432-449.

[23] A.A. Dobale, A.G. Tamirat, H.M. Chen, T.A. Berhe, C.J. Pan, W.N. Su, B.J. Hwang, A highly stable CuS and CuS-Pt modified Cu_2O/CuO heterostructure as an efficient photocathode for the hydrogen evolution reaction. J. Mater. Chem. A 4 (2016) 2205-2216.

[24] Q. Huang, F. Kang, H. Liu, Q. Li, X. Xiao, Highly aligned Cu_2O/CuO/TiO_2 core/shell nanowire arrays as photocathodes for water photoelectrolysis. J. Mater. Chem. A 1 (2013) 2418-2425.

[25] Z. Zhang, P. Wang, Highly stable copper oxide composite as an effective photocathode for water splitting via a facile electrochemical synthesis strategy. J. Mater. Chem. 22 (2012) 2456-2464.

[26] K. Nakaoka, J. Ueyama, K. Ogura, Photoelectrochemical behavior of electrodeposited CuO and Cu_2O thin films on conducting substrates. J. Electrochem. Soc. 151 (2004) C661-C665.

[27] N. Mukherjee, B. Show, S.K. Maji, U. Madhu, S.K. Bhar, B.C. Mitra, G.G. Khan, A. Mondal, CuO nano-whiskers: Electrodeposition, raman analysis, photoluminescence study and photocatalytic activity. Mater. Lett. 65 (2011) 3248-3250.

[28] Y. Bessekhouad, D. Robert, J.-V. Weber, Photocatalytic activity of Cu_2O/TiO_2, Bi_2O_3/TiO_2 and $ZnMn_2O_4/TiO_2$ heterojunctions. Catal. Today 101 (2005) 315-321.

[29] S. Masudy-Panah, R.S. Moakhar, C.S. Chua, H.R. Tan, T.I. Wong, D. Chi, G.K. Dalapati, Nanocrystal engineering of sputter-grown CuO photocathode for visible-light-driven electrochemical water splitting. ACS Appl. Mater. Interfaces 8 (2016) 1206-1213.

[30] G. Malandrino, S.T. Finocchiaro, R.L. Nigro, C. Bongiorno, C. Spinella, Free-standing copper(II) oxide nanotube arrays through an MOCVD template process. Chem. Mater. 16 (2004) 5559-5561.

[31] Y. Yang, Y. Li, M. Pritzker, Control of Cu_2O film morphology using potentiostatic pulsed electrodeposition. Electrochim. Acta 213 (2016) 225-235.

[32] G.K. Dalapati, S. Masudy-Panah, A. Kumar, C.C. Tan, H.R. Tan, D. Chi, Aluminium alloyed iron-silicide/silicon solar cells: A simple approach for low cost environmental-friendly photovoltaic technology. Sci. Rep. 5 (2015) 17810.

Chapter 3: Fabrication of CuO_x/WO_3 p-n heterojunction composite photocatalyst

3.1 Background

Solar energy conversion through photoelectrochemical (PEC) water splitting by semiconductors has becoming one of the most effective ways to solve energy and environmental issues.[1-5] To date, methods such as controlling band structure,[6-8] constructing semiconductor heterojunction[9-12] and homojunction[13] structure, preparing crystal facet,[14-16] loading cocatalysts,[17-19] tuning active sites and interfaces interactions,[20] and constructing hole transfer layer[21] have been widely used to expand the light absorption range of semiconductor material and improve its photocatalytic activity. Compared with p-type semiconductors, photocatalyst of n-type semiconductors have weak oxygen adsorption capacity.[22] This leads to that the photogenerated electrons cannot combine with the absorbed oxygen rapidly, which results in a high probability of recombination of photogenerated holes and electrons and low photocatalytic efficiency.

3.1.1 Heterojunction composite system

Cu_2O is a typical p-type semiconductor material, which has a high theoretical maximum PEC conversion efficiency.[23] In the photocatalytic system of Cu_2O, the valence band potential of Cu_2O is much lower than the water oxidation potential.[24] Therefore, it is difficult for Cu_2O to oxidize water to oxygen. We have successfully fabricated the p-CuO_x thin-film photocathode contains of CuO and Cu_2O, which solved the problem of its lower valence band potential and provide a photocurrent density of -3.2 mA cm^{-2} under a bias potential of -0.5V (vs. Ag/AgCl).[25] To get higher photoinduced current, the use of n-type semiconductor for composite modification of p-type semiconductor is expected to improve its defects. Heterojunction is formed by

successively depositing two or more layers of different semiconductor materials on the same substrate.[26] The fabrication of heterojunction structure can prolong the lifetime of charge carriers and enhance the separation of electron-hole, hence increase its PEC performance.[27-28] When two different types of semiconductor come into contact with each other, their respective energy band position will change, causing the change of the electrons transfer pathway.[29] In a p-n heterojunction, photogenerated electrons transfer to n-type semiconductor and photogenerated holes transfer to p-type semiconductor rapidly, resulting in the promoting of the separation of photogenerated electrons and holes.[30] In addition, in p-n heterojunction, the photogenerated electrodes enrich on the conduction band of n-type semiconductor with higher position, and the photogenerated holes enrich on the valence band of p-type semiconductor, which providing more photogenerated electrons, consequently the photogenerated electrons have stronger reduction capacities.

3.1.2 CuO_x/WO_3 p-n heterojunction structure

WO_3 is an n-type semiconductor with a bandgap of 2.5~2.8 eV.[31-32] Its valence band potential is higher than the water oxidation potential,[33-34] which can drive the water oxidation process smoothly. Consider of compounding p-CuO_x with n-WO_3 to employ p-n heterojunction to design a CuO_x/WO_3 photocatalyst. In the p-n heterojunction, photogenerated electrons transfer to the conduction band of n-WO_3 with higher position, and photogenerated holes transfer to the valence band of p-CuO_x, thus proving photogenerated electrons with stronger reduction capabilities. For the construction of CuO_x/WO_3, it can not only increase the hydrogen production of water reduced by the photoinduced electrons, but also promote the water oxidation process driven by the photoinduced holes. Thereby, improve its PEC conversion efficiency. Meanwhile, the photoinduced electrons can transfer from narrow bandgap semiconductor to wide bandgap semiconductor, which benefits to the charge separation and promotes the

photocatalytic activity of the heterojunction structure.[35] In order to improve the stability of the CuO_x/WO_3 structure and fully oxidize WO_3, treat the compound by annealing at a high temperature. Cu_2O is chemically unstable in the working environment that negative potential applied.[36] The addition of WO_3 can not only improve the photogenerated carrier separation efficiency, but also improve the stability of the Cu_2O photocathode. Currently, several deposition methods have been utilized to synthesize thin-film photoelectrode, such as magnetron reactive sputtering,[37] electrochemical deposition,[38] chemical vapor deposition,[39] pulsed laser deposition,[40] sol-gel,[41] and spray-pyrolysis.[42] Compared with these methods, the advantage of thin-film deposition by magnetron sputtering is that it can simply deposit high-quality and uniform thin-film with large areas at a high speed, and the properties of the sputtered thin-film photoelectrode can be reproducible.

3.1.3 The motivation and outline of this research

In the present work, we employed the p-n heterojunction to design a novel CuO_x/WO_3 photocatalyst overall water splitting device, and report on the effects of annealing on the CuO_x/WO_3 photocatalyst and its PEC performance. The CuO_x/WO_3 photocatalyst was synthesized by magnetron reactive sputtering and followed with thermal annealing under different conditions. The microstructure, morphology, element composition, element chemical and electronic state, optical properties and electrochemical properties were measured to characterize the performance of the CuO_x/WO_3 photocatalyst.

3.2 Experimental section

3.2.1 Preparation of CuO_x/WO_3 photocatalyst

F-doped SnO_2 transparent conducting glass (FTO) was used as a substrate of the CuO_x/WO_3 thin-film, which was firstly cleaned by ultrasonic cleaner with 1:1 of

acetone (99.8 % purity purchased from Kanto Chemical CO., INC., Japan) and ethanol (99.9 % purity purchased from Kanto Chemical CO., INC., Japan) mixed solutions for 5 min, followed by a second ultrasonically-cleaned with deionized water for 5 min, and blow-dried by N_2. The CuO_x/WO_3 photocatalyst was fabricated by magnetron reactive sputtering at room temperature, using the target of Cu and W (99.99 % purity) under Ar and O_2 atmospheres. The first program started with depositing CuO_x. The Cu target was firstly cleaned by a pre-sputtering in Ar ambient for 5 min to remove the impurities of the target surface, followed with a second pre-sputtering in Ar and O_2 ambient to reach the sputtering pressure. During the sputtering process, the sputtering chamber was pumped down to 2×10^{-5} Pa, the sputtering power was fixed at 30 W, Ar and O_2 flow was fixed at 30 sccm and 7 sccm. After 2 hours of depositing CuO_x, the second program came with depositing WO_3. The W target was also cleaned by a pre-sputtering in Ar ambient and a second pre-sputtering in Ar and O_2 ambient for 5 min and 3 min, respectively. The sputtering power of depositing WO_3 was fixed at 75 W, and the Ar and O_2 flow was fixed at 15 sccm and 50 sccm, the deposition time was 40 min.

3.2.2 Annealing of CuO_x/WO_3 photocatalyst

After depositing of CuO_x/WO_3 thin-film, a stable structure of the CuO_x/WO_3 thin-film was formed by annealing. In order to analyze the effects of different annealing conditions on CuO_x/WO_3 thin-film, we employed 4 groups of comparative experiments. The sample of first group was not treated with annealing. The second group was treated by rapid thermal annealing (RTA) with a temperature of 500 °C for 30 min in O_2 ambient, in which the heating rate was 10 °C s^{-1}. The samples of third and fourth group were treated by slow rate annealing (SRA) with a temperature of 300 °C and 500 °C for 30 min in O_2 ambient, respectively. And the heating rate of slow rate annealing was 1 °C s^{-1}.

After annealing, copper wire was connected with the conductive part of the FTO substrate without touching sputtered thin-film using a conductive sliver tape, and the exposed conductive parts of the FTO substrate were isolated with a parafilm to ensure that the photoelectrode has no leakage in electrolyte.

3.2.3 Characterization of CuO_x/WO_3 photocatalyst

X-ray diffraction (XRD, D/max-500, Rigaku Co., Tokyo, Japan) was used to analyze the crystalline structures the sputtered CuO_x/WO_3. Raman (InVia Confocal Raman Microscope, Renishaw, UK) spectroscopy was utilized to record in the spectral range of 20-1400 cm^{-1} with 633 nm excitation wavelength. The morphology and element mapping of the CuO_x/WO_3 photocatalyst was characterized by scanning electron microscope (SEM, Ultra 55, Zeiss, Germany). Atomic force microscope (AFM) was used to further analyze the surface roughness of the CuO_x/WO_3 photocatalyst. The element composition, chemical and electronic state of the CuO_x/WO_3 was analyzed via X-ray photoelectron spectroscopy (XPS, PHI 5000 Versa Probe, 2ULVAC-PHI, INC., Chigasaki, Japan). Furthermore, the optical properties of the CuO_x/WO_3 photocatalysts were investigated by UV-Vis spectrophotometer (TU-1901, PERSEE, Beijing, China).

The photoelectrochemical test was performed on an electrochemical workstation (CHI660D, Shanghai Chenhua Instrument Co., Ltd., Shanghai, China). The test was used of a three-electrode system, which used the CuO_x/WO_3 photocatalyst as a working electrode, used Pt sheet and Ag/AgCl electrode as a counter electrode and reference electrode, respectively. The three-electrode was immersed into 0.1 mol L^{-1} Na_2SO_4 electrolytes (99.0% purity purchased from Kanto Chemical CO., INC., Japan). The incident light source was from a Xe lamp (PLS-SXE300, Beijing Changtuo Co., Ltd., Beijing, China) of 150 W with a sunlight intensity of 100 mW cm^{-2}. The photoinduced volt-ampere curve (i-V curve) was measured from -0.5 V to 0.1 V (vs. Ag/AgCl) with an applied potential scan rate of 0.02 V s^{-1}. The photoinduced i-V

curve was performed during light on-off in turns with 1 second, respectively. The Mott-Schottky plots was performed at an applied potential scanning from -0.2 V to 2 V (vs. Ag/AgCl) in dark, with a frequency of 10 Hz and an AC voltage magnitude of 10 mV. The EIS test was measured with a frequency range from 10^6 to 10^{-1}, and an AC voltage magnitude of 5 mV. The EIS spectra were measured in dark and under illumination, respectively. All of the electrochemical tests were carried out in 0.1 mol L^{-1} Na_2SO_4 electrolytes.

3.3 Results and discussion

3.3.1 Structure and morphology of CuO_x-WO_3 photocatalyst

Fig. 3-1 shows the XRD patterns of the CuO_x/WO_3 samples. The diffraction patterns for the sputtered films have six WO_3 peaks at 15.62°, 23.38°, 24.58°, 29.10°, 31.14° and 56.11°, corresponding to (020), (001), (110), (200), (031) and (113) of WO_3, respectively. The WO_3 peaks tend to stronger obviously on curve d and e, especially at (020), (001) and (110), indicating that monoclinic WO_3 formed after annealing at a high temperature about 500 °C. Peak appearing in 42.20° and 61.57° can be indexed to monoclinic CuO (200) and (-113), and the (200) peak only formed on curve d and e, due to the high temperature of annealing. The Cu_2O (222) peak at 77.32° turns to smaller as the annealing temperature increasing. Simultaneously, the intensity of WO_3 (001) and (110) peaks after SRA 500 ℃ tends to stronger than that after RTA 500 °C, indicating that WO_3 shows a better crystallinity as the proceeding of slow rate annealing.

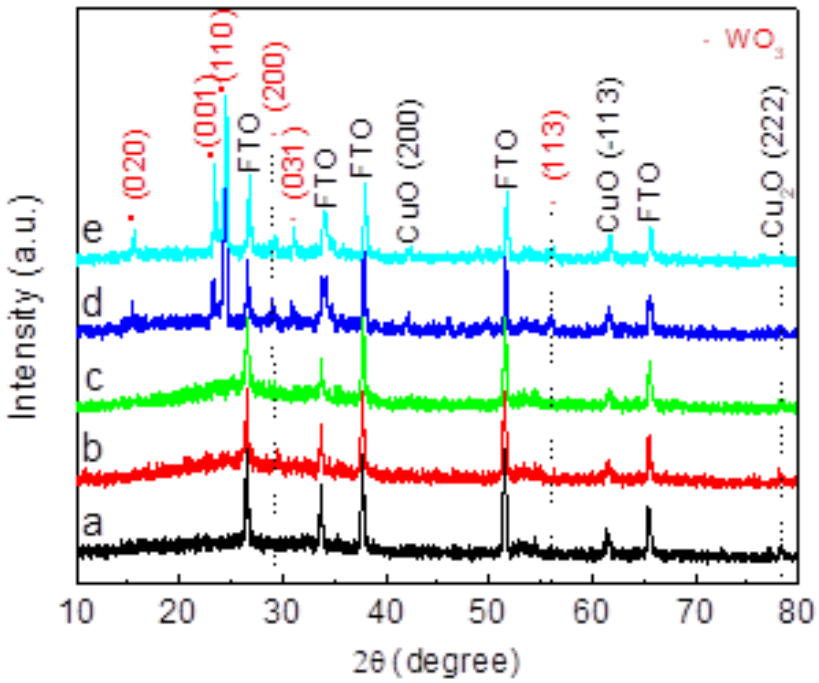

Fig. 3-1 XRD patterns of (a) CuO_x, (b) CuO_x/WO_3 without annealing, (c) CuO_x/WO_3 SRA 300 °C, (d) CuO_x/WO_3 RTA 500 °C, (e) CuO_x/WO_3 SRA 500 °C.

As the Raman spectrum of the samples shows in Fig. 3-2, the CuO peak at 286 cm^{-1} shows a small peak on CuO_x sample, then turns to stronger as the increasing of annealing temperature. On the other side, the Cu_2O peak at 903 cm^{-1} becomes stronger after annealing, and tends to weaker obviously, owing to SRA of 500 °C. However, the Cu_2O peak do not appear on curve a and b. The WO_3 peaks are formed at 125 cm^{-1}, 706 cm^{-1} and 806 cm^{-1}. It can be clearly seen that, the WO_3 peaks of 706 cm^{-1} and 806 cm^{-1} turn to particularly stronger after SRA 500 °C for the sample, and all of the WO_3 peaks do not appear clearly on the un-annealed sample.

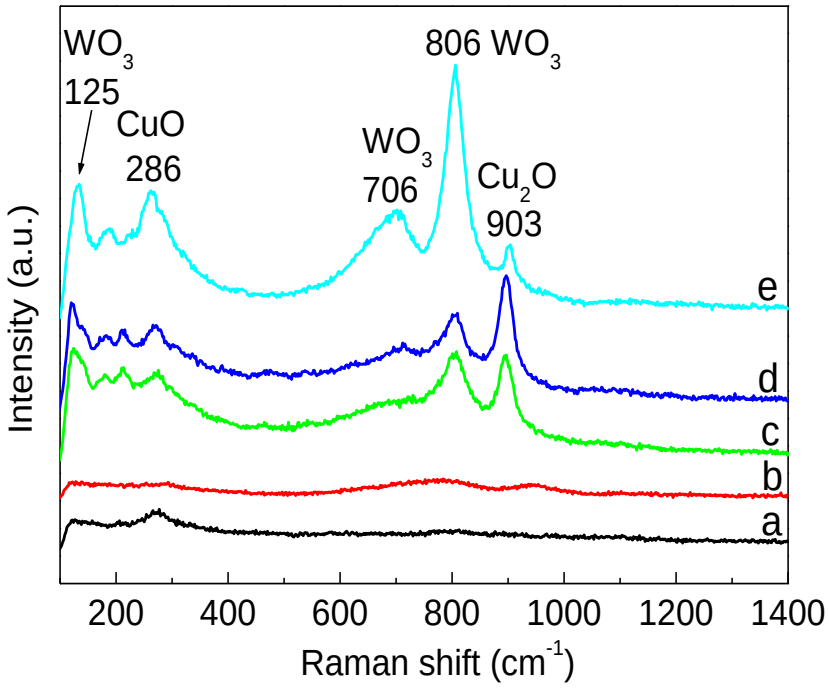

Fig. 3-2 Raman spectra of (a) CuO_x, (b) CuO_x/WO_3 without annealing, (c) CuO_x/WO_3 SRA 300 °C, (d) CuO_x/WO_3 RTA 500 °C, (e) CuO_x/WO_3 SRA 500 °C.

The surface morphologies of the CuO_x/WO_3 photocatalyst under different annealing conditions are analyzed using AFM and SEM. The AFM images of the sample after RTA 500 °C and SRA 500 °C are shown in Fig. 3-3. It can be seen clearly, the CuO_x/WO_3 after SRA 500 °C is relatively smoother than that after RTA 500 °C. Table 2-1 shows the image statistics results of AFM. According to the results, the root-mean-square (RMS) roughness (R_q) value is found to be 19.2 nm and 11.5 nm for RTA 500 °C and SRA 500 °C, respectively. This phenomenon indicates that slow rate annealing is more appropriate to oxidize the CuO_x/WO_3 photocatalyst with a smooth surface.

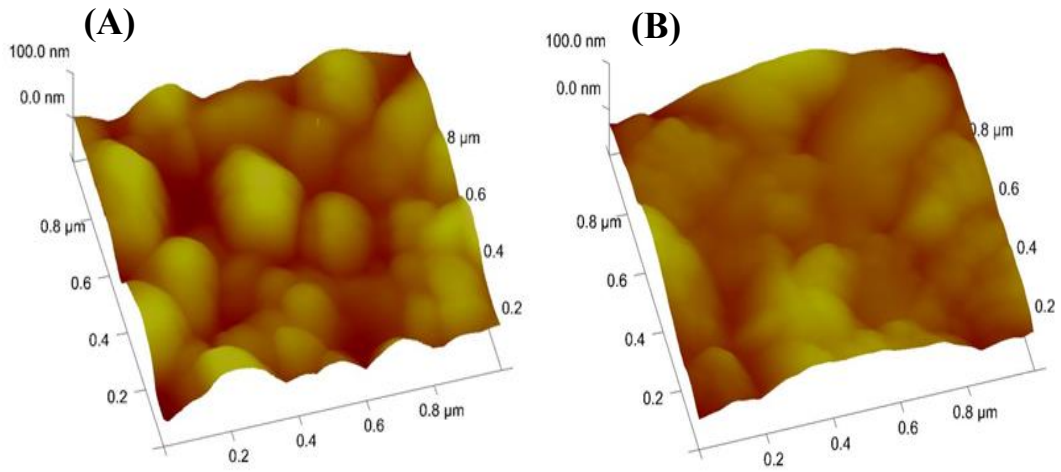

Fig. 3-3 AFM images of (A) CuO_x/WO_3 RTA 500 °C, (B) CuO_x/WO_3 SRA 500 °C.

Table 3-1 The image statistics results of AFM

Sample	Image Raw Mean	Image Mean	Image Z Range	Image RMS (R_q)	Image R_a
CuO_x/WO_3 RTA 500 °C	-638 nm	-0.000001 nm	130 nm	19.2 nm	15.3 nm
CuO_x/WO_3 SRA 500 °C	173 nm	-0.000001 nm	77.9 nm	11.5 nm	9.03 nm

The SEM images of the surface of the sample after RTA 500 °C and SRA 500 °C are shown in Fig. 3-4A and Fig. 3-4B. According to the results, the surface WO_3 consist of large particles roughly 200 nm in diameter. After RTA of 500 °C, particles on the surface of WO_3 present floating state, explaining that rapid thermal annealing makes the thin-film surface non-uniform. The cross-section SEM image of the CuO_x/WO_3 photocatalyst is shown in Fig. 3-4C. As shown in the cross-section image of the sample, the thin-film divides into two layers, obviously. The first layer deposited on FTO substrate is CuO_x, which has a thickness of 500 nm, and the thickness of the second layer of WO_3 is about 200 nm. Fig. 3-4D shows the elemental maps of CuO_x/WO_3 SRA 500 °C composite, which was performed by SEM. The results of O, Cu, and W element

can be confirmed that CuO_x/WO_3 evenly distributes on the surface of FTO substrate, indicating that the positions of CuO_x layer and WO_3 layer are significantly staggered.

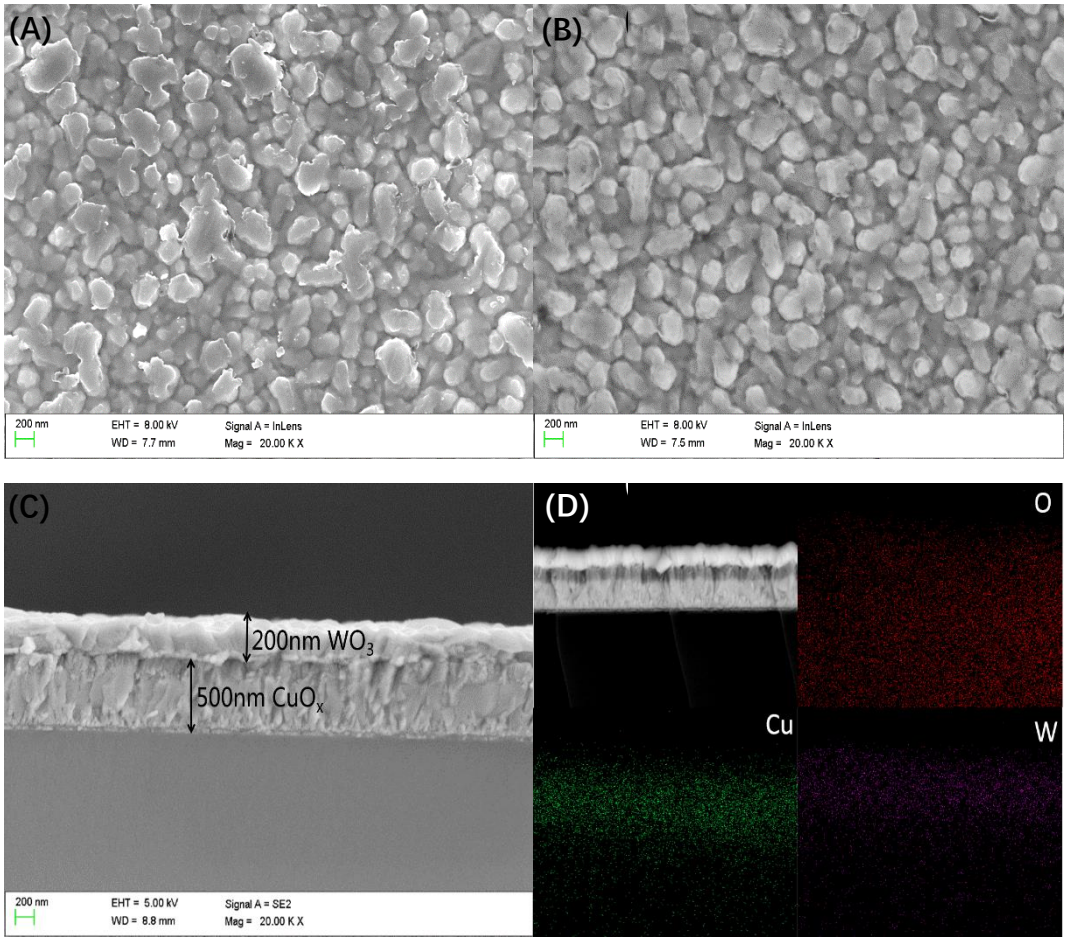

Fig. 3-4 Typical SEM images of the surface of (A) CuO_x/WO_3 RTA 500 °C, (B) CuO_x/WO_3 SRA 500 °C; (C) the cross-section SEM image of CuO_x/WO_3 SRA 500 °C; (D) SEM elemental maps (O, Cu, W) of CuO_x/WO_3 SRA 500 °C.

3.3.2 XPS and optical characterization of CuO_x-WO_3 photocatalyst

XPS can be further utilized to assess the chemical and electronic states of a sample. Figure 3-5 shows the XPS spectra of the samples. Fig. 3-5A, Fig. 3-5B and Fig. 3-5C show the full-spectra scan, O 1s and Cu 2p of CuO_x photocatalyst, respectively. As Fig. 3-5B shows, there is a strong O 1s peak at 529.5 eV and a small peak at 531.6 eV, which correspond to binding energy of O^{2-} in CuO and Cu_2O, respectively. As the Cu 2p of the Fig. 3-5C shows, the binding energy at 932.9 eV and 952.5 eV are indicative of Cu $2p_{3/2}$ and Cu $2p_{1/2}$, which belong to Cu^{2+} and Cu^{+}, respectively. Meanwhile, the main

component of CuO_x is bivalent copper, because there are two strong satellite peaks in the Cu 2p spectrum.[43] The XPS survey spectrum of CuO_x/WO_3 is shown in Fig. 3-5D, demonstrating that the distinctive as well as the Auger peaks of Cu, O and W in the sputtered sample confirmed the presence of copper, oxygen and tungsten elements. Fig. 3-5, Fig. 3-5F and Fig. 3-5G shows the O 1s spectra and the peak fitting of CuO_x/WO_3 photocatalyst under different annealing conditions. The O 1s spectra indicate the presence of WO_3 and CuO. The main peak at 530.7 eV is related to O^{2-} in WO_3 (Fig. 3-5E), which has been reported.[44] However, the O 1s peak of CuO_x/WO_3 after RTA 500 °C shifts to 530.0 eV which also belongs to WO_3, indicating that rapid thermal annealing changes the chemical bond of WO_3. In addition, the small peak of O^{2-} at 531.6 (Fig. 3-5B) disappears with the addition of WO_3, indicating that the O^{2-} of CuO_x covered by WO_3 cannot be detected by XPS. The Cu 2p of CuO_x/WO_3 photocatalyst XPS spectra is analyzed in Fig. 3-5F, the binding energies of 932.7 eV and 952.5 eV are indicative of Cu $2p_{3/2}$ and Cu $2p_{1/2}$, which correspond to CuO and Cu_2O, respectively. Compare with the Cu 2p peaks of CuO_x shown in Fig. 3-5C, the Cu $2p_{3/2}$ of CuO_x/WO_3 right shifts from 932.9 eV to 932.7 eV. However, strong Cu^{2+} satellites disappear in the CuO_x/WO_3, owing to the incorporation of WO_3. In the case of W 4f spectra of CuO_x/WO_3 shown in Fig. 3-5G, two peaks can be distinguished, which indicated the W 4f binding energies were 35.7 eV and 37.9 eV, respectively. Usually the peaks at 35.7 eV and 37.9 eV correspond to W $4f_{7/2}$ and W $4f_{5/2}$ clear assigned to WO_3, which is in agreement with the findings reported by X. Ding.[45] The W 4f spectrum of CuO_x/WO_3 after RTA 500 °C right shift to 35.2 eV and 37.4 eV, which also related to WO_3, testifying that the high temperature of rapid thermal annealing changes the chemical bond of WO_3, which accords with the O 1s result.

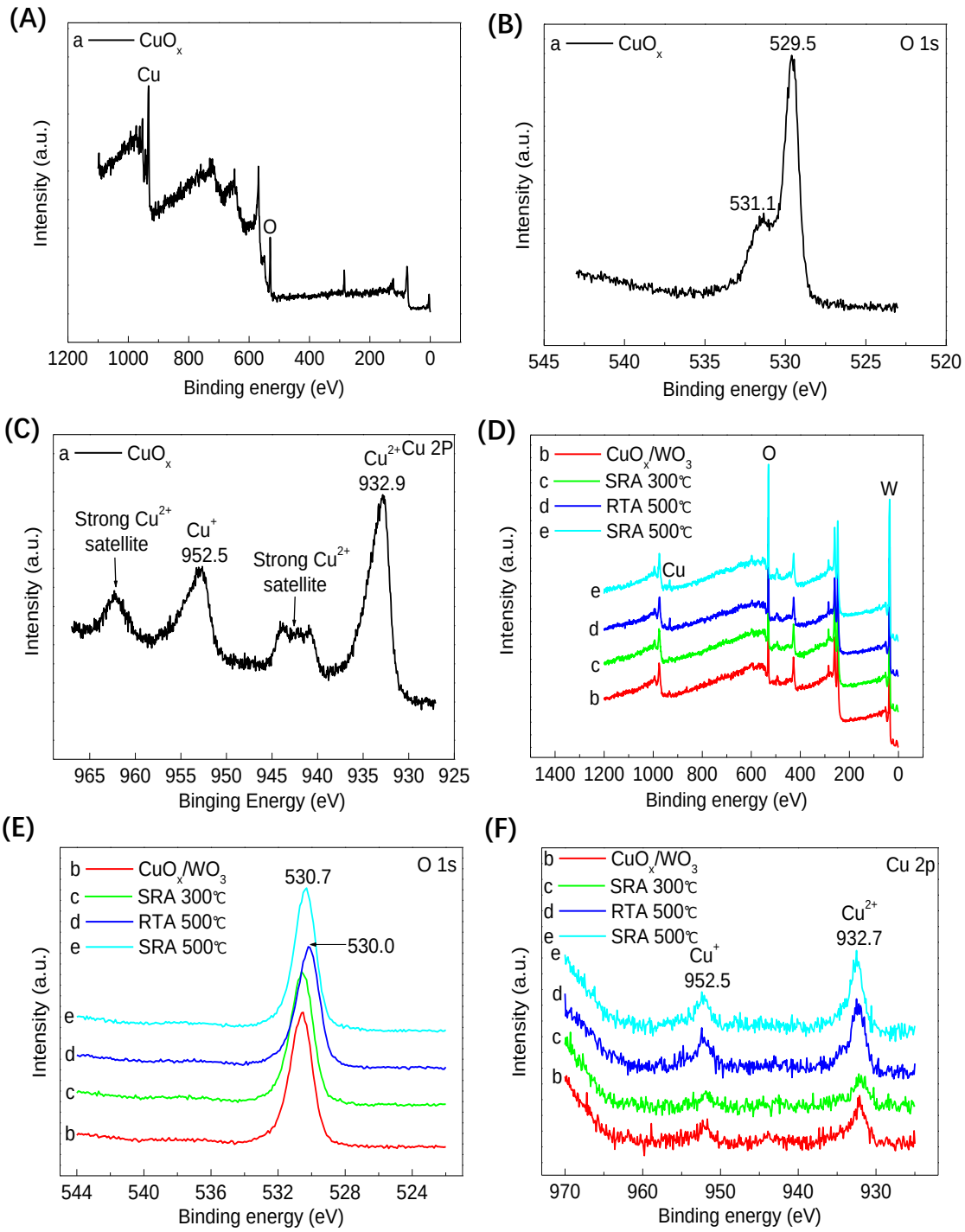
(A)
a —— CuO$_x$
Cu
O
Intensity (a.u.)
1200 1000 800 600 400 200 0
Binding energy (eV)
(B)
a —— CuO$_x$
529.5
O 1s
531.1
Intensity (a.u.)
545 540 535 530 525 520
Binding energy (eV)
(C)
a —— CuO$_x$
Cu^{2+}Cu 2P
932.9
Strong Cu^{2+} satellite
Cu^{+} 952.5
Strong Cu^{2+} satellite
Intensity (a.u.)
965 960 955 950 945 940 935 930 925
Binging Energy (eV)
(D)
b —— CuO$_x$/WO$_3$
c —— SRA 300℃
d —— RTA 500℃
e —— SRA 500℃
O
W
Cu
e
d
c
b
Intensity (a.u.)
1400 1200 1000 800 600 400 200 0
Binding energy (eV)
(E)
b —— CuO$_x$/WO$_3$
c —— SRA 300℃
d —— RTA 500℃
e —— SRA 500℃
O 1s
530.7
530.0
e
d
c
b
Intensity (a.u.)
544 540 536 532 528 524
Binding energy (eV)
(F)
b —— CuO$_x$/WO$_3$
c —— SRA 300℃
d —— RTA 500℃
e —— SRA 500℃
Cu 2p
Cu^{2+} 932.7
Cu^{+} 952.5
e
d
c
b
Intensity (a.u.)
970 960 950 940 930
Binding energy (eV)

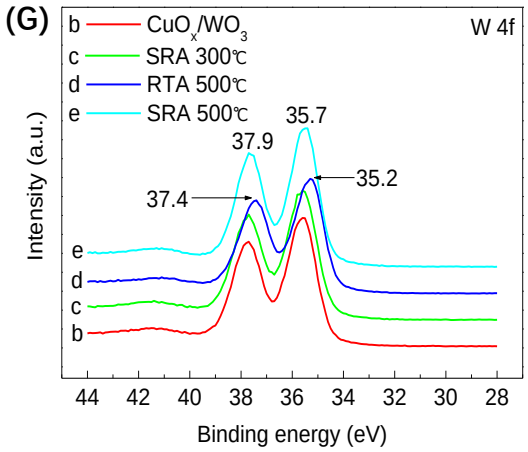

Fig. 3-5 XPS spectra of (A) full-spectra scan, (B) O 1s, and (C) Cu 2p of CuO_x; (D) full-spectra scan, (E) O 1s, (F) Cu 2p, and (G) W 4f of the CuO_x/WO_3 under different annealing conditions.

Fig. 3-6A shows the UV-Vis DRS of the samples. UV-Vis absorption edge is relevant to the energy band of the semiconductor material. The absorption band-edges of the CuO_x/WO_3 photoelectrode shows a small red shift after annealing of 500 °C, suggesting that the photoelectrode after SRA 500 °C can absorb larger wavelength range of visible light. The bandgap energy of the prepared photoelectrode can be estimated from the tangent line in the plot of Kubelka-Munk function versus the photon energy, as shown in Fig. 3-6B, according to the following equation:[46]

$$A = C\left(hv - E_g\right)^{n/2}/hv$$

In which, A is the absorption coefficient, C is the proportionality constant, h is the Planck constant, v is the light frequency, and E_g is the bandgap. Based on the equation, the E_g value of the prepared CuO_x, CuO_x/WO_3, CuO_x/WO_3 SRA 300 °C, CuO_x/WO_3 RTA 500 °C, CuO_x/WO_3 SRA 500 °C photoelectrode are 2.46, 3.10, 3.33, 3.71, 2.83 eV, respectively, indicating that the addition of WO_3 without annealing increases the bandgap of the composite photoelectrode, and the treatment of SRA 500 °C can greatly shorten its bandgap.

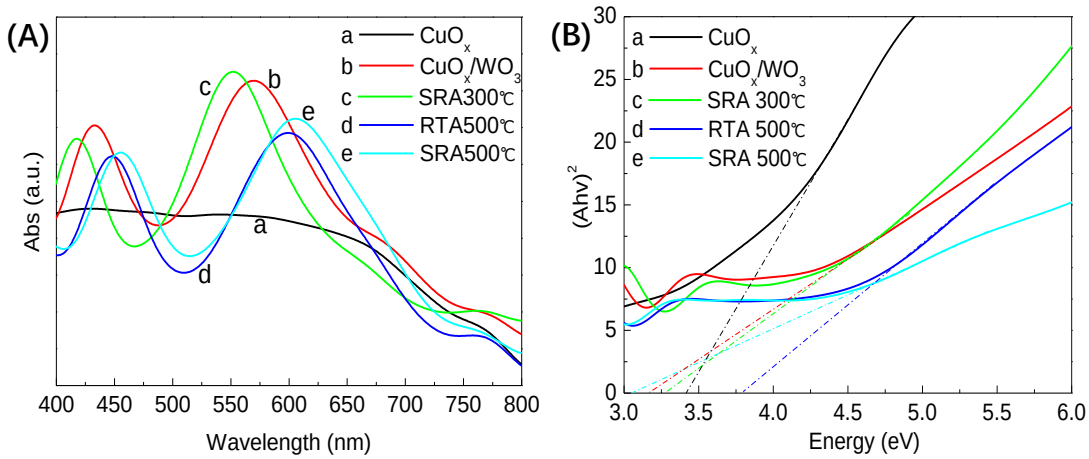

Fig. 3-6 (A) UV-Vis absorption spectra of the prepared photoelectrodes; (B) the plot of transformed Kubelka-Munk function versus the photon energy, where the dot line is the tangent of the linear part.

3.3.3 PEC performance of CuO_x/WO_3 photocatalyst

Mott-Schottky equation describes the relationship between semiconductor space charge capacitance and applied potential. Mott-Schottky equation shows in followed equation,

$$\frac{1}{C^2} = \frac{2}{\varepsilon\varepsilon_0 q N_q} \cdot \left(E - E_{fb} - \frac{kT}{q}\right)$$

Where C is semiconductor space charge capacitance; ε is semiconductor relative permittivity; ε_0 is vacuum permittivity, which is equal to 8.85×10^{-14} F cm^{-1}; q is elemental charge, e is equal to 1.602×10^{-19} C; N_q is carrier concentration; E_{fb} is semiconductor flat band potential; E is applied potential; k is Boltzmann constant, which is equal to 1.38×10^{-23} $J \cdot K^{-1}$; and T is temperature. Fig. 3-7A and Fig. 3-7B shows the Mott-Schottky plots of the samples in 0.1 mol L^{-1} Na_2SO_4 electrolytes under a dark condition. According to the equation, the carrier concentration N_q can be calculated by tangent slope, due to the linear relationship between $\frac{1}{C^2}$ and applied potential E. The flat band potential of the semiconductor sample can be obtained by the intercept of tangent and potential axis. The flat band potential of CuO_x is approximately 0.96 V. The flat band potential of CuO_x/WO_3 is about 1.46 V, and its flat band potential

is negative shifted to 1.36 V after annealing. This phenomenon indicates that the increasing of semiconductor Fermi level and electron energy level,[47] which causes the electrons from conduction band easily lost to participate in the water reduction reaction. In addition, according to thermodynamics, the negative shift of the flat band potential means that the electrons of conduction band excited by light illumination have stronger reduction capacities,[48] as a result of that the photogenerated electrons are easily obtained by H_2O to generated hydrogen, thereby improves the photocatalytic hydrogen production activity. EIS can be used to evaluate the interface charges transfer rate of a semiconductor photocatalyst and the reaction degree of its interfacial electron, which is tightly related to its electrochemical properties. Fig. 3-7C shows the EIS result of CuO_x/WO_3 SRA 500 °C measured in dark. Fig. 3-7D shows the EIS results and the relevant equivalent circuit of the CuO_x/WO_3 SRA 500 °C under illumination. In which, R_{sol} is the solution resistance, Q and Q_{dl} represents the double layer capacitance,[49-50] R_f and R_t corresponds to the charge carriers transfer resistance in the photocatalyst, R_{ct} and C describes the electrons transfer resistance and the capacitance of the interface, respectively. The fitting values of the circuit elements are shown in Table 3-2. The R_f value of CuO_x/WO_3 SRA 500 °C is found to be 6538 Ω cm^2 in dark, which is approximately 10 times larger than that under illumination. The sample shows an R_t value of 953.3 Ω cm^2 in dark, and this value of R_t decreases to 372.8 Ω cm^2 under illumination. The decrease of R_f and R_t is due to the injection of photogenerated electrons, which promotes the electrochemical reaction. Moreover, CuO_x/WO_3 SRA 500 °C shows a R_{ct} value of 27580 Ω cm^2 in dark, while that of the sample decreases to 6418 Ω cm^2 under illumination, indicating that with the injection of illumination, the interfacial reaction capability of the photocatalyst is enhanced significantly. The EIS test illustrates that under illumination, the electrochemical reaction and the interfacial reaction capability of the photocathode are promoted, owing to the injection of photogenerated electrons.

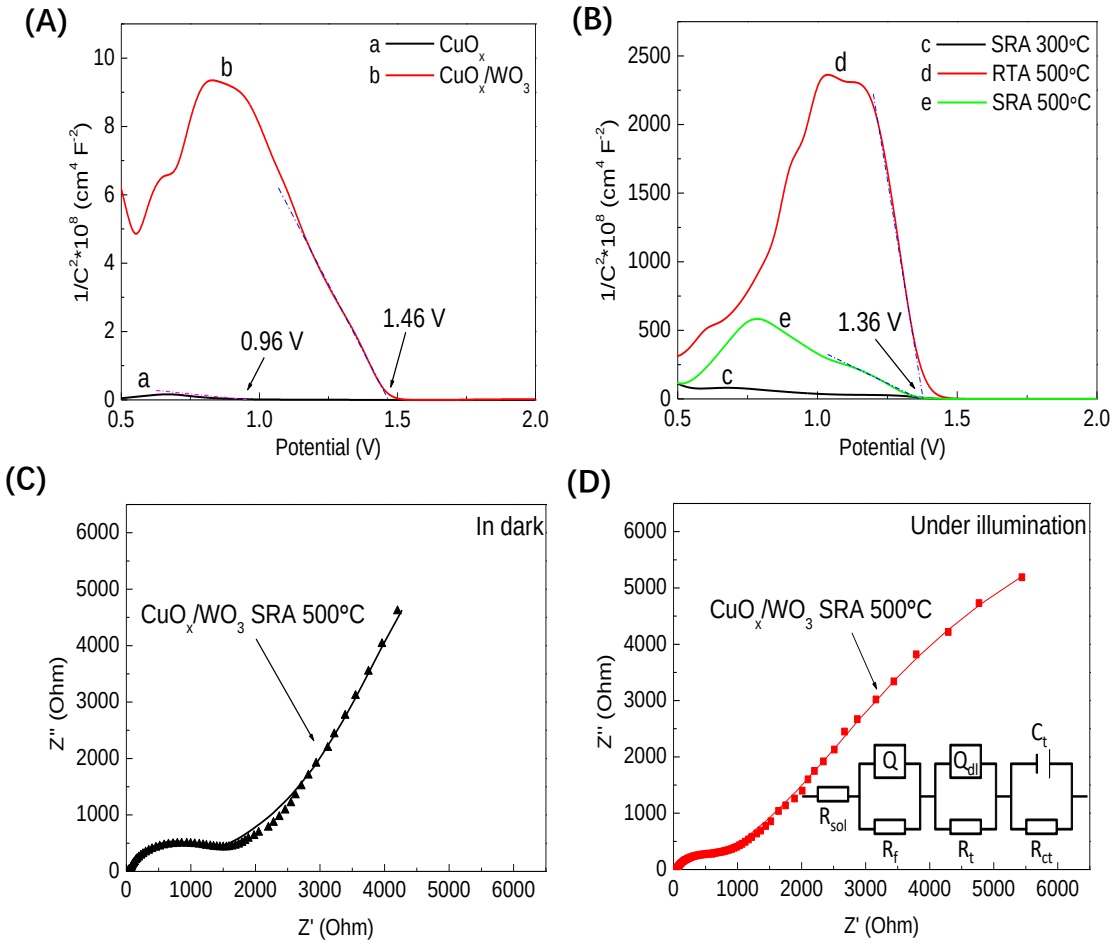

Fig. 3-7 (A) Mott-Schottky plots of (a) CuO_x, (b) CuO_x/WO_3 without annealing; (B) Mott-Schottky plots of (c) CuO_x/WO_3 SRA 300 °C, (d) CuO_x/WO_3 RTA 500 °C, (e) CuO_x/WO_3 SRA 500 °C; (C) EIS spectra of CuO_x/WO_3 SRA 500 °C test in dark; (D) EIS spectra and the equivalent circuit for fitting EIS results of CuO_x/WO_3 SRA 500 °C under illumination.

Table 2-2 The fitting EIS values of the CuO_x/WO_3 SRA 500 °C photocatalyst.

Sample	R_{sol}/Ω cm^2	Q_c/Ω^{-1} cm^{-2} s^n	R_c/Ω cm^2	Q_{dl}/Ω^{-1} cm^{-2} s^n	R_t/Ω cm^2	C/μF cm^{-2}	R_{ct}/Ω cm^2	Condition
CuO_x/WO_3 SRA 500 °C	35.68	2.382×10^{-4}	6538	1.713×10^{-6}	953.3	4.415×10^{-4}	27580	In dark
CuO_x/WO_3 SRA 500 °C	32.12	2.699×10^{-4}	588.6	2.413×10^{-6}	372.8	4.728×10^{-4}	6418	Under illumination

Fig. 3-8A shows the photoinduced volt-ampere characteristic curves (i-v curve) of the CuO_x/WO_3 photocatalysts. The three-electrode was immersed into 0.1 mol L^{-1} Na_2SO_4 electrolytes under a chopped AM 1.5 light illumination to evaluate its PEC response. The photoinduced i-V curves were tested under applied potential scanning from -0.5 V to 0.1 V, with a scan rate of 0.02 V. The photoinduced volt-ampere characteristics were performed during incident light on-off in turns with 1 second, respectively. Fig. 3-8B shows the photoinduced current of the photoelectrodes under a bias potential of -0.5 V. The CuO_x photocatalyst generated a photoinduced current of -2.5 mA cm^{-2} at -0.5 V bias potential. After compounding with WO_3, it generated a photoinduced current of -2.0 mA cm^{-2}, with a very large dark current. The photoinduced current of CuO_x/WO_3 after rapid thermal annealing of 500 °C was about -3.4 mA cm^{-2}. The sample after slow rate annealing of 300 °C still has a large dark current. After slow rate annealing of 500 °C, the CuO_x/WO_3 generated a photoinduced current of -3.8 mA cm^{-2}, which was about 1.5 times higher than CuO_x, and 2 times higher than CuO_x/WO_3 without annealing, which benefits from its small dark current. The photoinduced time-current curve (i-t curve) of the CuO_x and CuO_x/WO_3 SRA 500 °C is shown in Fig. 3-8C, and the inset of Fig. 3-8C shows the surface morphology characterized by SEM of the photoelectrode before and after i-t test. The photoinduced i-t test was measured under a bias potential of -0.2 V. According to i-t curve, after turning on the light, a strong negative current peak appears, indicating that there are some defects formed owing to the process of instantaneous photoelectrons charging. The CuO_x photoelectrode shows a quite small photocurrent after light on for 350 seconds, and the SEM images of the CuO_x surface morphology shows that the CuO_x particles have reduced obviously after i-t test. This phenomenon indicates that the CuO_x photoelectrode is unstable in the electrolytes under light illumination. In addition, the CuO_x/WO_3 SRA 500 °C photoelectrode shows a relatively stable photocurrent curve after 600 seconds i-t test, compare with the SEM images, the surface morphology of the CuO_x/WO_3 SRA 500 °C photoelectrode has not changed after i-t test, demonstrating

that the CuO_x/WO_3 SRA 500 °C photoelectrode is stable under -0.2 V bias potential.

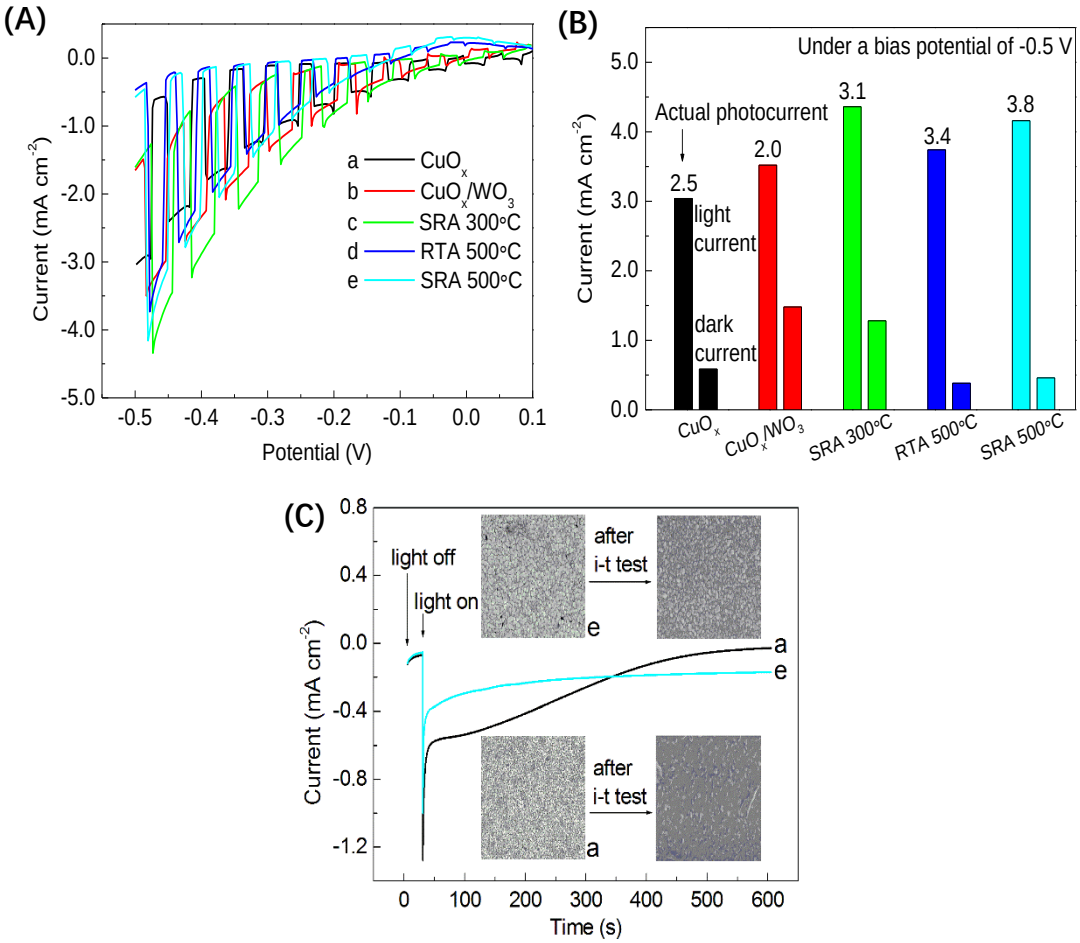

Fig. 3-8 (A) The photoinduced volt-ampere characteristic curves (i-v curve), (B) and the photoinduced current (under a bias potential of -0.5 V) of a: CuO_x, b: CuO_x/WO_3 without annealing, c: CuO_x/WO_3 SRA 300 °C, d: CuO_x/WO_3 RTA 500 °C and e: CuO_x/WO_3 SRA 500 °C; (C) the photoinduced time-current curve (i-t curve) of a: CuO_x and b: CuO_x/WO_3 after SRA 500 °C, the inset shows the surface morphology of the photoelectrode before and after i-t test.

3.4 Principle of p-n heterojunction system

The transportation of the charge carries in CuO_x/WO_3 photoelectrode with p-n heterojunction is shown in Fig. 3-9.[51] After two different types of semiconductors contact with each other, the p-type CuO_x energy band will shift upward while the n-WO_3 energy band will move downward with the respective diffusion of electrons and holes. When drift current and diffusion current counteract, a space charge region will be formed near the interface to generate built-in electric field. Under light illumination,

p-CuO_x and n-WO_3 will be excited at the same time. Under the effect of the built-in electric field, the electrons will transfer to n-WO_3 and holes will transfer to p-CuO_x rapidly, thereby promoting the separation of the photogenerated carriers effectively. In addition, in the p-CuO_x/n-WO_3 heterojunction, the photogenerated electrons will enrich in the conduction band of n-WO_3 with a higher position, and the photogenerated holes will enrich in the valence band of p-CuO_x, which providing more photogenerated electrons with stronger reduction capacities. Therefore, by the p-n heterojunction assistant, the reduction energy of the photogenerated electrons can be increased, and the light absorption range can be extended with the induction of two types of semiconductor in that enhance the theoretical PEC water reduction efficiency, sequentially. Fig. 3-10 shows the schematic illustration of the mechanism of FTO/CuO_x/WO_3 photocatalyst overall water splitting device. Under light illumination, photogenerated electrons and holes are transfer to the surface of WO_3 for hydrogen evolution reaction and FTO for oxygen evolution reaction, respectively. Thereby, effectively restraining the recombination of photogenerated carriers, and providing more photogenerated electrons. The band potential of semiconductor material determines the degree of PEC water splitting. For Cu_2O, its valence band potential is lower than water oxidation potential, therefore the water oxidation process is different to drive. In addition, the conduction band potential of WO_3 is positive than the water reduction potential, as result of the water reduction process for H_2 production is different to carry out. The formation of ohmic contact by heterojunction can change the carries transfer pathway, which can solve this problem effectively.[52]

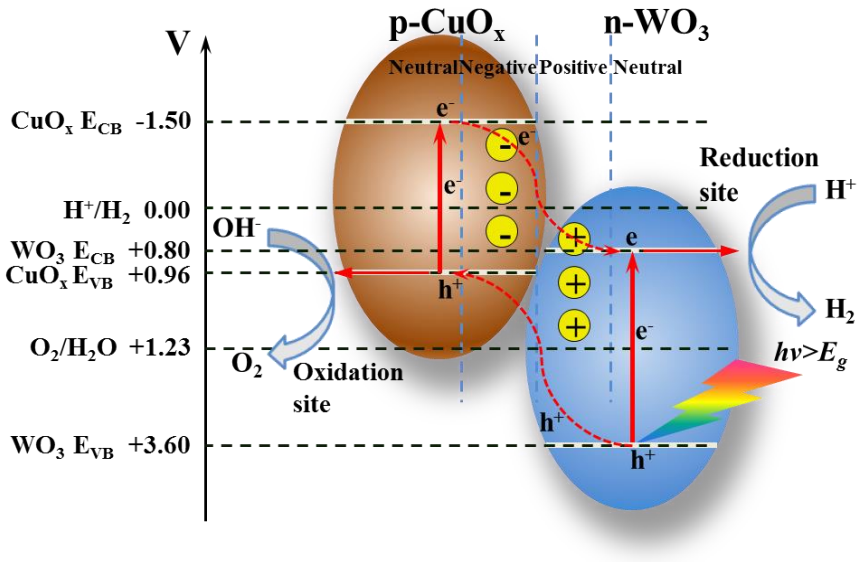

Fig. 3-9 Transportation of the charge carries in CuO_x/WO_3 photoelectrode with p-n heterojunction.

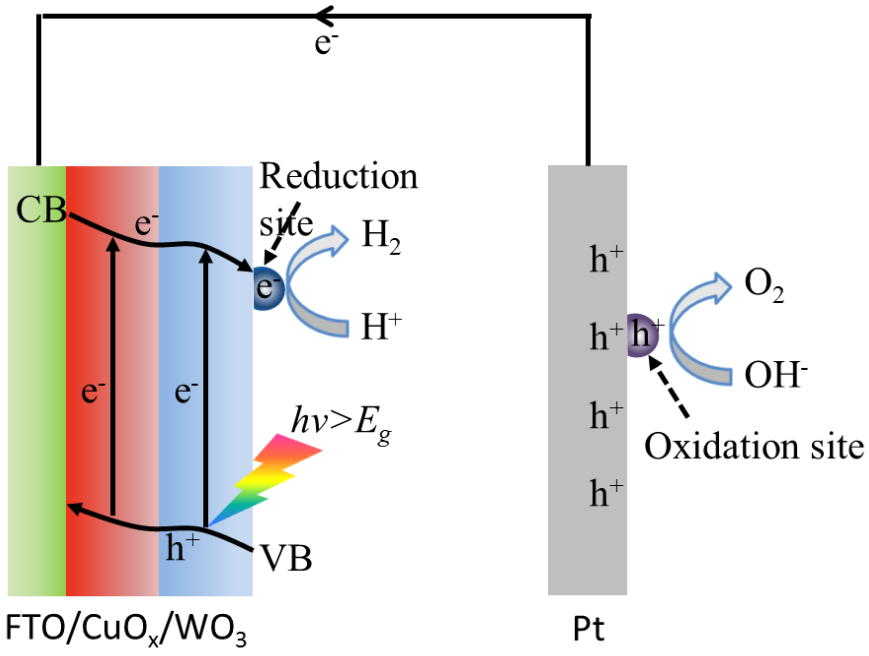

Fig. 3-10 Schematic illustration of the mechanism of FTO/CuO_x/WO_3 photocatalyst overall water splitting device.

3.5 Conclusion

To summarize, we demonstrated a promising CuO_x/WO_3 photocatalyst with p-n

heterostructure for PEC water reduction using a simple and easy-to-control deposition method, reactive magnetron sputtering and slow rate annealing. The photoinduced current density and photostability enhanced by the assistant of p-n heterojunction and slow rate annealing. The optimal annealing condition is determined to be slow rate annealing of 500 °C (the heating rate is 1 °C s^{-1}), and the photocatalyst (-3.8 mA cm^{-2}) shows approximately 1.5 times and 2 times increase in photogenerated current density, compared with the CuO_x (-2.5 mA cm^{-2}) and CuO_x/WO_3 without annealing (-2.0 mA cm^{-2}), respectively. It is believed that the light illumination causes the interfacial charge transfer, by the p-n heterojunction assistant, reduction capabilities of the photogenerated electrons can be increased, thus promotes the PEC water reduction process. The assist in slow rate annealing causes the upper WO_3 layer better crystallized and oxidized completely, resulting in a stable structure of the CuO_x/WO_3 photocatalyst. Furthermore, the EIS results indicate that the improved PEC performance of the sample under illumination is due to the promoting of the interfacial reaction capability by photoinduced electrons.

3.6 Reference

[1] A. Fujishima, K. Honda, Electrochemical photolysis of water at a semiconductor electrode. Nature 238 (1972) 37-38.

[2] A. Mills, S. Le Hunte, An overview of semiconductor photocatalysis. J. Photochem. Photobiol. A 108 (1997) 1-35.

[3] M. G. Walter, E. L. Warren, J. R. McKone, S. W. Boettcher, Q. Mi, E. A. Santori, N. S. Lewis, Solar water splitting cells. Chem. Rev. 110 (2010) 6446-6473.

[4] T. Hisatomi, J. Kubota, K. Domen, Recent advances in semiconductors for photocatalytic and photoelectrochemical water splitting. Chem. Soc. Rev. 43 (2014) 7520-7535.

[5] I. Roger, M. A. Shipman, M. D. Symes, Earth-abundant catalysts for

electrochemical and photoelectrochemical water splitting. Nat. Rev. Chem.1 (2017) 0003.

[6] E. Borgarello, J. Kiwi, M. Graetzel, E. Pelizzetti, M. Visca, Visible light induced water cleavage in colloidal solutions of chromium-doped titanium dioxide particles. J. Am. Chem. Soc. 104 (1982) 2996-3002.

[7] R. Asahi, T. Morikawa, T. Ohwaki, K. Aoki, Y. Taga, Visible-light photocatalysis in nitrogen-doped titanium oxides. Science 293 (2001) 269-271.

[8] P. Niu, L.-C. Yin, Y.-Q. Yang, G. Liu, H.-M. Cheng, Increasing the visible light absorption of graphitic carbon nitride (melon) photocatalysts by homogeneous self-modification with nitrogen vacancies. Adv. Mater. 26 (2014) 8046-8052.

[9] S. Yan, T. Liu, Y. Zhang, D. Sun, X. Li, G. Xie, C. Feng, L. Xu, Enhanced photoelectrochemical performance of hydrogen-treated $SrTiO_3/TiO_2$ nanotube arrays heterojunction composite. J. Electroanal. Chem. 807 (2017) 213-219.

[10] Y. Bu, J. P. Ao, A review on photoelectrochemical cathodic protection semiconductor thin films for metals. Green Energy Environ. 2 (2017) 331-362.

[11] J. Low, J. Yu, M. Jaroniec, S. Wageh, A. A. Al-Ghamdi, Heterojunction photocatalysts. Adv. Mater. 29 (2017) 1601694.

[12] Z. Liu, J. Zhang, W. Yan, CdTe/CdS core/shell quantum dots cocatalyzed by sulfur tolerant $[Mo_3S_{13}]^{2-}$ nanoclusters for efficient visible-light-driven hydrogen evolution. ACS Sustainable Chem. Eng. 6 (2018) 3565-3574.

[13] T. Wang, Y. Wei, X. Chang, C. Li, A. Li, S. Liu, J. Zhang, J. Gong, Homogeneous Cu_2O p-n junction photocathodes for solar water splitting. Appl. Catal. B Environ 226 (2018) 31-37.

[14] Y. L. Qi, Y. F. Zheng, H. Y. Yin, X. C. Song, Enhanced visible light photocatalytic activity of AgBr on {001} facets exposed to BiOCl. J. Alloy. Compd. 712 (2017) 535-542.

[15] Y. Bu, J. Tian, Z. Chen, Q. Zhang, W. Li, F. H. Tian, J.-P. Ao, Optimization of the photo-electrochemical performance of Mo-doped $BiVO_4$ photoanode by controlling the

metal-oxygen bond state on (020) facet. Adv. Mater. Interfaces 4 (2017) 1601235.

[16] J. Zhang, P. Zhang, T. Wang, J. Gong. Monoclinic WO_3 nanomultilayers with preferentially exposed (002) facets for photoelectrochemical water splitting. Nano Energy 11 (2015) 189-195.

[17] K. Maeda, K. Teramura, D. Lu, T. Takata, N. Saito, Y. Inoue, K. Domen, Photocatalyst releasing hydrogen from water. Nature 440 (2006) 295.

[18] W. Li, C. Feng, S. Dai, J. Yue, F. Hua, H. Hou, Fabrication of sulfur-doped g-C_3N_4/Au/CdS Z-scheme photocatalyst to improve the photocatalytic performance under visible light. Appl. Catal. B Environ. 168-169 (2015) 465-471.

[19] K. Maeda, K. Domen, Development of novel photocatalyst and cocatalyst materials for water splitting under visible light. Bull. Chem. Soc. Jap. 89 (2016) 627-648.

[20] X. Chang, T. Wang, Z.-J. Zhao, P. Yang, J. Greeley, R. Mu, G. Zhang, Z. Gong, Z. Luo, J. Chen, Y. Cui, G. A. Ozin, J. Gong, Tuning Cu/Cu_2O interfaces for the reduction of carbon dioxide to methanol in aqueous solutions. Angew. Chem. Int. Edit. 57 (2018) 15415-15419.

[21] Y. Wei, X. Chang, T. Wang, C. Li, J. Gong. A low-cost NiO hole transfer layer for ohmic back contact to Cu_2O for photoelectrochemical water splitting. Small 13 (2017) 1702007.

[22] J. Li, L. Liu, Y. Yu, Y. Tang, H. Li, F. Du, Preparation of highly photocatalytic active nano-size TiO_2-Cu_2O particle composites with a novel electrochemical method. Electrochem. Commun. 6 (2004) 940-943.

[23] X. Zhang, J. Song, J. Jiao, X. Mei, Preparation and photocatalytic activity of cuprous oxides. Solid State Sci. 12 (2010) 1215-1219.

[24] Z. Zheng, B. Huang, Z. Wang, M. Guo, X. Qin, X. Zhang, P. Wang, Y. Dai, Crystal faces of Cu_2O and their stabilities in photocatalytic reactions. J. Phys. Chem. C 133 (2009) 14448-14453.

[25] T. Xie, T. Zheng, R. Wang, Y. Bu, J.-P. Ao, Fabrication of CuO_x thin-film

photocathodes by magnetron reactive sputtering for photoelectrochemical water reduction. Green Energy Environ. 3 (2018) 239-246.

[26] A. G. Milnes, D. L. Feucht, Heterojunctions and metal-semiconductor junctions, ACADEMIC PRESS, New York, (1972).

[27] M.-K. Lee, T.-H. Shih, High photocatalytic activity of nanoscaled heterojunction of ZnS grown on fluorine and nitrogen Co–doped TiO_2. J. Electrochem. Soc. 154 (2007) 49-51.

[28] Y. Bassekhouad, D. Robert, J.-V. Weber, Photocatalytic activity of Cu_2O/TiO_2, Bi_2O_3/TiO_2 and $ZnMn_2O_4/TiO_2$ heterojunctions. Catal. Today 101 (2005) 315-321.

[29] D. Jiang, L. Chen, J. Zhu, M. Chen, W. Shi, J. Xie, Novel p-n heterojunction photocatalyst constructed by porous graphite-like C_3N_4 and nanostructured BiOI: Facile synthesis and enhanced photocatalytic activity. Dalton Trans. 42 (2013) 15726-15734.

[30] C. Han, Y.-P. Lei, Y.-D. Wang, Recent progress on nano-heterostructure photocatalysts for solar fuels generation. J. Inorg. Mater. 30 (2015) 1121-1130.

[31] A. M. Mohamed, S. A. Shaban, H. A. EI Sayed, B. E. Alanadouli, N. K. Allam, Morphology-photoactivity relationship: WO_3 nanostructured films for solar hydrogen production. Int. J. Hydrog. Energy 41 (2016) 866-872.

[32] S. Yao, F. Qu, G. Wang, X. Wu, Facile hydrothermal synthesis of WO_3 nanorods for photocatalysts and supercapacitors. J. Alloy. Compd. 724 (2017) 695-702.

[33] J. A. Seabold, K.-S. Choi, Effect of a cobalt-based oxygen evolution catalyst on the stability and the selectivity of photo-oxidation reactions of a WO_3 photoanode. Chem. Mater. 23 (2011) 1105-1112.

[34] A. Kudo, Y. Miseki, Heterogeneous photocatalyst materials for water splitting. Chem. Soc. Rev. 38 (2009) 253-278.

[35] M. Santamaria, G. Conigliaro, F. Di Franco, F. Di Quarto, Photoelectrochemical evidence of Cu_2O/TiO_2 nanotubes hetero-junctions formation and their physicochemical characterization. Electrochim. Acta. 144 (2014) 315-323.

[36] M. J. Siegfried, K.-S. Choi, Elucidating the effect of additives on the growth and stability of Cu_2O surfaces via shape transformation of pre-grown crystals. J. Am. Chem. Soc. 128 (2006) 10356-10357.

[37] J. Deuermeier, J. Gassmann, J. Brötz, A. Klein, Reactive magnetron sputtering of Cu_2O: Dependence on oxygen pressure and interface formation with indium tin oxide. J. Appl. Phys. 109 (2011) 113704.

[38] T. G. Kim, H. Oh, H. Ryu, W.-J. Lee, The study of post annealing effect on Cu_2O thin-films by electrochemical deposition for photoelectrochemical applications. J. Alloy. Comp. 612 (2014) 74-79.

[39] L. Bergerot, C. Jiménez, O. Chaix-Pluchery, L. Rapenne, J.-L. Deschanvres, Growth and characterization of Sr-doped Cu_2O thin films deposited by metalorganic chemical vapor deposition. Phys. Status Solidi A 212 (2015) 1735-1741.

[40] W. Niu, L. Zhu, Y. Wang, Z. Lou, Z. Ye, Interfacial study of $Cu_2O/Ga_2O_3/AZO/TiO_2$ photocathode for water splitting fabricated by pulsed laser deposition. Catal. Sci. Technol. 7 (2017) 1602-1610.

[41] Y.-F. Lim, C. S. Chua, C. J. J. Lee, D. Chi, Sol–gel deposited Cu_2O and CuO thin films for photocatalytic water splitting. Phys. Chem. Chem. Phys. 16 (2014) 25928-25934.

[42] C.-Y. Chiang, K. Aroh, N. Franson, V. R. Satsangi, S. Dass, S. Ehrman, Copper oxide nanoparticle made by flame spray pyrolysis for photoelectrochemical water splitting-Part II. Photoelectrochemical study. Int. J. Hydrog. Energy 36 (2011) 15519-15526.

[43] M. C. Biesinger, L. W. M. Lau, A. R. Gerson, R. S. C. Smart, Resolving surface chemical states in XPS analysis of first row transition metals, oxides and hydroxides: Sc, Ti, V, Cu and Zn. Appl. Surf. Sci. 257 (2010) 887-898.

[44] G. Wang, Y. Ling, H. Wang, X. Yang, C. Wang, J. Z. Zhang, Y. Li, Hydrogen-treated WO_3 nanoflakes show enhanced photostability. Energy Environ. Sci. 5 (2012) 6180-6187.

[45] X. Ding, D. Zeng, S. Zhang, C. Xie, C-doped WO_3 microtubes assembled by nanoparticles with ultrahigh sensitivity to toluene at low operating temperature. Sens. Actuator B-Chem. 155 (2011) 86-92.

[46] Y. Sun, C. J. Murphy, K. R. Reyes-Gil, E. A. Reyes-Garcia, J. M. Thornton, N. A. Morris, D. Raftery, Photoelectrochemical and structural characterization of carbon-doped WO_3 films prepared via spray pyrolysis. Int. J. Hydrog. Energy 34 (2009) 8476-8484.

[47] J.-M. Zhao, F. Gu, X.-H. Zhao, Y. Zuo, Semiconductor properties of anodic oxide film formed on aluminum. Acta Phys.-Chim. Sin. 24 (2008) 147-151.

[48] T.-H. Wang, Y.-X. Li, S.-Q. Peng, G.-X. Lv, S.-B. Li, Activity of rare earth doped TiO_2 deposited with Pt for photocatalytic hydrogen generation. Acta. Chimica. Sinica. 63 (2005) 797-801.

[49] N. K. Allam, A. J. Poncheri, M. A. El-Sayed, Vertically oriented Ti-Pd mixed oxynitride nanotube arrays for enhanced photoelectrochemical water splitting. ACS Nano 5 (2011) 5056-5066.

[50] J. Li, C.-J. Lin, J.-T. Li, Z.-Q. Lin, A photoelectrochemical study of CdS modified TiO_2 nanotube arrays as photoanodes for cathodic protection of stainless steel. Thin Solid Films 519 (2011) 5494-5502.

[51] M.T. Nenadovic, T. Rajh, O. I. Micic, A. J. Nozik, Electron transfer reactions and flat-band potentials of tungsten(VI) oxide colloids. J. Phys. Chem. 88 (1984) 5827-5830.

[52] P. Zhou, J. Yu, M. Jaroniec, All-solid-state Z-scheme photocatalytic systems. Adv. Mater. 26 (2014) 4920-4935.

Chapter 4: Synthesis of nanocomposite electrocatalyst

4.1 Background

Electrocatalytic water splitting method can be regarded as a promising one for clean energy and renewable.[1] Synthesis of stable and efficient electrocatalysts is paramount importance for hydrogen evolution reaction (HER),[2-3] and oxygen evolution reaction (OER).[4] To date, many researchers have devoted to manufacture earth-abundant catalysts to displace the noble metal catalysts (Pt/Pd for HER,[5-7] IrO_2 for OER[8]), such as phosphides,[9-11] carbides,[12-14] transition-metal oxides/hydroxides/sulfides,[15-20] metal alloys,[21-24] nitrides,[25] and selenides.[26]

4.1.1 Ni-Fe-P bifunctional electrocatalyst

It has been demonstrated that bimetallic phosphide has higher performance for overall water splitting than that of monometallic phosphide as it can serve for acceptor of proton and hydride, which benefits for hydrogen evolution and proton discharging process.[27] On the other band, phosphate can be produced as an active center, therefore the catalytic activity towards OER can be improved by the existence of phosphate.[28] Besides, Ni-Fe-P materials have been reported as a superior electrocatalyst for water splitting.[29-30] This is mainly due to the introduction of Ni-Fe bimetallic system further improved the catalytic activities.[31] Recently, numbers of researches indicated the outstanding electrocatalytic preformation of transition-metal phosphide synthesized by electrodeposition, electroless plating, and phosphating.[32] Though some progress has been made in this field, there are still some problems to find a simple approach for manufacturing a catalyst with stable and highly efficient for overall water splitting instead of noble metal.

4.1.2 Advantages of doped-perovskite

Perovskite-type oxides have the general formula ABO_3 (A and B are unequal cations). It can produce minute particles with high metallic dispersion when subjected to the redox process,[33-34] as a result of providing a better matrix for the transition metal electrocatalysts.[35] Recent years, perovskite-type oxides have been reported as highly efficient catalysts towards and OER,[36-38] which is attributed to the flexible structure of perovskite-type oxide that can provide disorder-free channels of oxygen vacancies to improve the oxygen ions mobility.[39] In addition, a $Pr_{0.5}$BSCF perovskite oxide as highly active catalyst for HER were reported in 2016,[40] which owes to the tunable electronic structure of perovskite oxide providing surface redox chemistry and oxygen deficiency. The iron manganese oxide ($FeMnO_3$) has been remarked displaying very favorable electrochemical properties for lithium-ion batteries anode material due to its intrinsically high capacity, small bandgap and excellent ion diffusivity.[41] Moreover, $FeMnO_3$ has been reported as a supercapacitor electrode,[42] which has favorable specific capacitance and excellent recycling durability. At present, $FeMnO_3$, its promising potential in such fields as catalysis and electrochemical engineering has not been applied to catalytic hydrogen evolution.

4.1.3 The motivation and outline of this research

Herein, we prepared a nanocomposite electrocatalyst Ni-Fe-P-$FeMnO_3$ on Ni foam for overall water splitting through a facile method of electroless plating and rapid dealloying. The as-prepared Ni-Fe-P-$FeMnO_3$/NF presents a quite high HER catalytic performance, with the assistance of the synergistic effect between nickel/iron and phosphorus, as well as Ni foam substrate endows more active sites for the electrocatalyst. The unique structure of perovskite material gives it many advantages, which benefit for almost every step of the electrocatalytic process.

4.2 Experimental section

4.2.1 Chemicals and materials

Ammonium bicarbonate (NH_4HCO_3, 99.5%) and manganese sulfate ($MnSO_4 \cdot H_2O$, 99.5%) were purchased from Tianjin BASF Chemical Co., Ltd. Ferrous sulfate ($FeSO_4 \cdot 7H_2O$, 99.5%) and nickel foam (99.9%) were purchased from Tianjin Zhiyuan Chemical Reagent Co., Ltd. Nickel sulfate ($NiSO_4 \cdot 6H_2O$, 99.0%), ammonium iron sulfate ($(NH_4)_2Fe(SO_4)_2 \cdot 6H_2O$, 99.0%) were purchased from Shanghai Tongya Chemical Technology Development Co. Ltd. Sodium citrate ($Na_3C_6H_5O_7 \cdot 2H_2O$, 99.0%), sodium hypophosphite ($NaH_2PO_2 \cdot H_2O$, 99.0%) and ammonium fluoride ($NH_4F \cdot H_2O$, 99.0%) were purchased from Tianjin kwangfu Fine Chemical Industry Research Institute. All reagents were used directly without further purification.

4.2.2 Preparation of Ni-Fe-P-$FeMnO_3$/NF electrocatalyst

The Ni foam was used as a substrate which was firstly ultrasonic cleaned by acetone for 30 min, followed by ultrasonic cleaned by 5% HCl for 30 min to wipe off the oxide forming on the surface. The Ni foam was finally rinsed with deionized water until the pH=7 and dried in vacuum atmosphere of 60 ºC. The $FeMnO_3$ nanoparticles used in our experiments were prepared in the following process: 255.2 g L^{-1} ammonia solution and 7.9 g L^{-1} ammonium bicarbonate solution were added into a mixed solution of 16.9 g L^{-1} manganese sulfate and 64.9 g L^{-1} ferrous sulfate. The above mixed solution was standing for 2 h, and then the precipitate was filtered out and washed for several times and dried in drying oven under 60 ºC for 8 h. It was calcined in the air at 850 ºC for 4 h to obtain the $FeMnO_3$ solid. Finally, the $FeMnO_3$ solid was grinded into nanoparticles. The Ni-Fe-P-$FeMnO_3$ electrocatalyst was deposited onto Ni foam in the alkaline solution containing of 7.5 g L^{-1} nickel (II) sulfate, 17.5 g L^{-1} ammonium iron (II) sulfate, 20 g L^{-1} sodium citrate, 40 g L^{-1}

sodium hypophosphite, 10 g L^{-1} ammonium fluoride and 0-15 g L^{-1} $FeMnO_3$ nanoparticles. The Ni-Fe-P-1g $FeMnO_3$/NF, Ni-Fe-P-2g $FeMnO_3$/NF and Ni-Fe-P-3g $FeMnO_3$/NF electrocatalyst were obtained by adding 1g, 2g and 3 g $FeMnO_3$ nanoparticles into 200 mL electroless solution respectively. The electroless composite plating process was carried out for 1 h under the water-bath temperature of 90 ºC, and the pH of the electroless plating solution was controlled at 9 by ammonia solution. The as-prepared precursor was immersed in 5% HCl for 20, 30 and 40 seconds to adjust the atomic ratio of nickel and iron. Then the dealloyed Ni-Fe-P-$FeMnO_3$/NF was ultrasonic cleaned with deionized water and dried under 60 ºC for 8 h.

4.2.2 Structural characterization

The morphology structure of the prepared electrocatalysts was observed by scanning electron microscopy (SEM, JSM-6700F, JEOL). The phase structure of the prepared $FeMnO_3$ nanoparticles and the Ni-Fe-P-$FeMnO_3$/NF was further characterized via X-ray diffraction (XRD, X'Pert Powder, PANalytical B. V.) The compositions and the chemical states of Ni, Fe, P and Mn on the Ni-Fe-P-$FeMnO_3$/NF were analyzed through X-ray photoelectron spectroscopy (XPS, PHI 5000 Versa Probe, 2ULVAC-PHI). The interface morphologies between $FeMnO_3$ nanoparticles and Ni-Fe-P matrix were investigated via high-resolution transmission electron microscopy (HRTEM, JEM-2000EX, JEOL)

4.2.3 Electrocatalytic measurements

The linear sweep voltammetry (LSV) towards HER and electrochemical impedance spectra (EIS) were performed on an electrochemical workstation (CHI66B, Shanghai Chenhua Instrument Co., Ltd.). The electrocatalytic tests were used a three-electrode system, in which the custom-made Ni-Fe-P-$FeMnO_3$/NF(1 cm × 1 cm), Hg/HgO electrode and Pt sheet were performed as working electrode, reference electrode and

counter electrode, respectively. The three-electrode was immersed into 1 M KOH electrolyte during the test. The LSV test was carried out 5 times at 1 mV s^{-1} scan rate with 90 % compensation, and the analysis curve used the final sweep result. In addition, the LSV polarization curves towards HER were IR-corrected according to the following equations:

$$E_{corrected} = E_{RHE} - iR_s \times 90\%$$

$$E_{RHE} = E_{vs.\ Hg/HgO} + 0.098 + 0.059 \times \mathrm{pH}$$

Where $E_{corrected}$ is the iR-corrected potential, E_{RHE} is the calculated reversible hydrogen electrode (RHE) potential, $E_{vs.\ Hg/HgO}$ is the measured potential through Hg/HgO reference electrode, i is the measured current density, pH is equal to 14 as the use of 1 M KOH electrolyte, and R_s is the equivalent series resistance measured by EIS. The EIS was recorded at a constant potential of -1.0268 V (vs. RHE), the EIS was measured under the frequency range from 0.01 Hz to 10^5 Hz, and an AC voltage of 5 mV.

4.3 Results and discussion

4.3.1 Structure and morphology of Ni-Fe-P-$FeMnO_3$/NF

The electroless plating process results in a brown thin film deposited on the Ni foam substrate. Fig. 1a and 1b show the cross-sectional images of the Ni-Fe-P-$FeMnO_3$/NF observed by SEM. It can be seen from Fig. 1a, porous nanostructures with unequal pore sizes were obtained after fast dealloying. The porous nanostructure could fully contact with the electrolyte, which promotes the effect of electrocatalysis. The energy dispersive X-ray spectroscopy (EDX) mapping of the Ni-Fe-P-$FeMnO_3$/NF (Fig. 1c) confirms the existence of Ni, Fe, P, Mn and O elements.

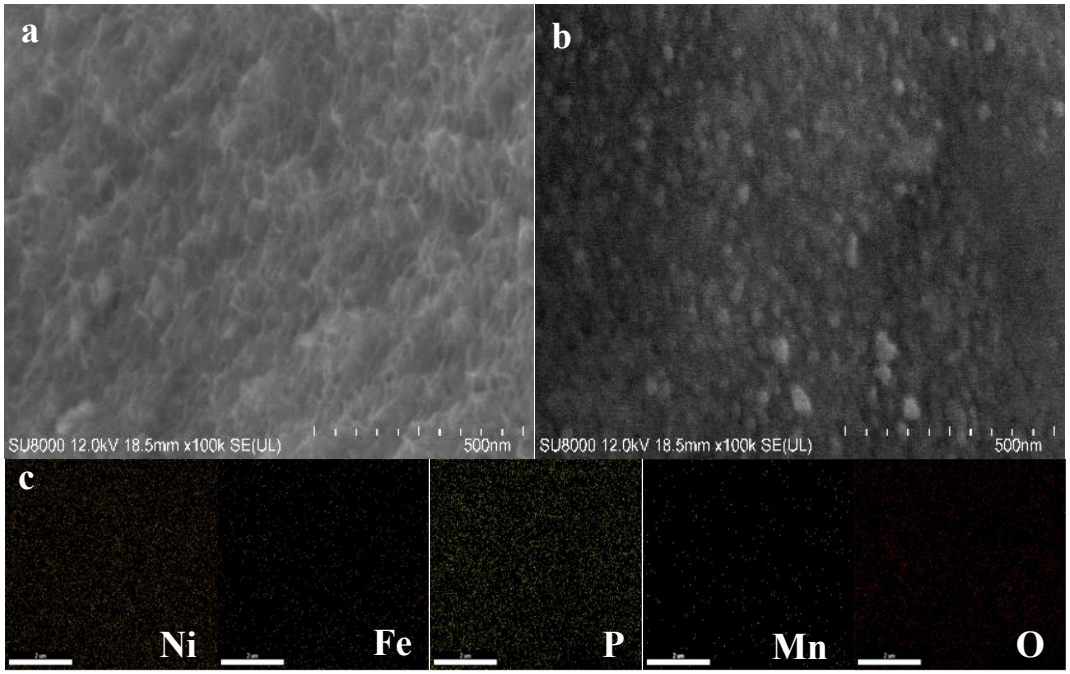

Fig. 4-1 (a) and (b) SEM images of Ni-Fe-P-$FeMnO_3$/NF; (c) Corresponding EDX mapping of the Ni-Fe-P-$FeMnO_3$/NF.

Fig 1b and Fig. 2a shows the $FeMnO_3$ nanoparticles composited in the electroless coating by SEM and TEM, respectively. The diameters of $FeMnO_3$ nanoparticles are ranged from 3 nm to 10 nm. The well-resolved lattice features of the electrocatalysts are shown in HRTEM image (Fig. 2b and 2c). The fringes with lattice spacing of d = 0.272, 0.162 and 0.251 nm can be assigned to be the (222), (440) and (123) facets of $FeMnO_3$ (PDF #75-0894). Moreover, the $FeMnO_3$ nanoparticles are surrounded by amorphous Ni-Fe-P to form heterojunction structure.

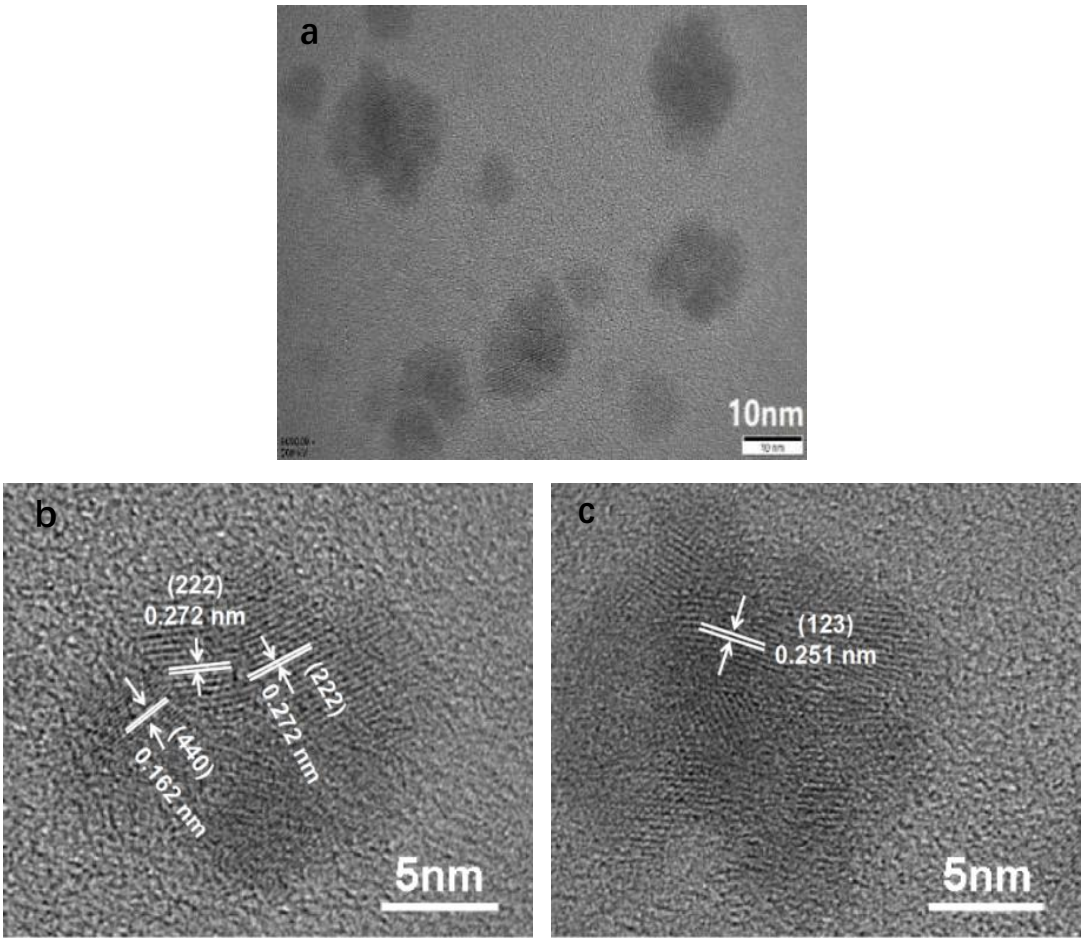

Fig. 4-2 HRTEM images of the Ni-Fe-P-$FeMnO_3$/NF towards different facets.

The phase structure of $FeMnO_3$ nanoparticles and Ni-Fe-P-$FeMnO_3$/NF was evaluated via XRD. The XRD patterns of the $FeMnO_3$ nanoparticles (Fig. 3a) have a number of peaks that can be well-indexed to $FeMnO_3$ (PDF #75-0894). As shown in Fig 3b, with the addition of $FeMnO_3$, the diffraction peaks of Ni-Fe-P alloy decrease significantly, indicating that the addition of $FeMnO_3$ decreases the crystallinity of the electroless composite coating. When the addition amount of $FeMnO_3$ nanoparticles reaches 2g in 200 mL electroless solution, the crystallization of Ni-Fe-P-$FeMnO_3$ is already inconspicuous, indicating that the Ni-Fe-P alloy gradually turns from crystalline state to amorphous state, which is consistent with the HRTEM results. This illustrates the promotion of the catalysis process. It is attributed to the short-rang order and activity sites of the amorphous materials. [43, 44] Due to the $FeMnO_3$ nanoparticles dispersed in the Ni-Fe-P matrix, the diffraction peak of $FeMnO_3$ could not be detected

by XRD. The diffraction peaks at 45.62°, 53.02°, and 77.87° corresponding to the (111), (200), and (220) planes of Ni-Fe (PDF #38-0409), respectively. It is observed that the diffraction peaks shift to the pure Ni peaks slightly, since the Ni-Fe-P-$FeMnO_3$/NF is rich in nickel atoms. This small shift indicates that Fe is consolidated into the Ni lattice. [45]

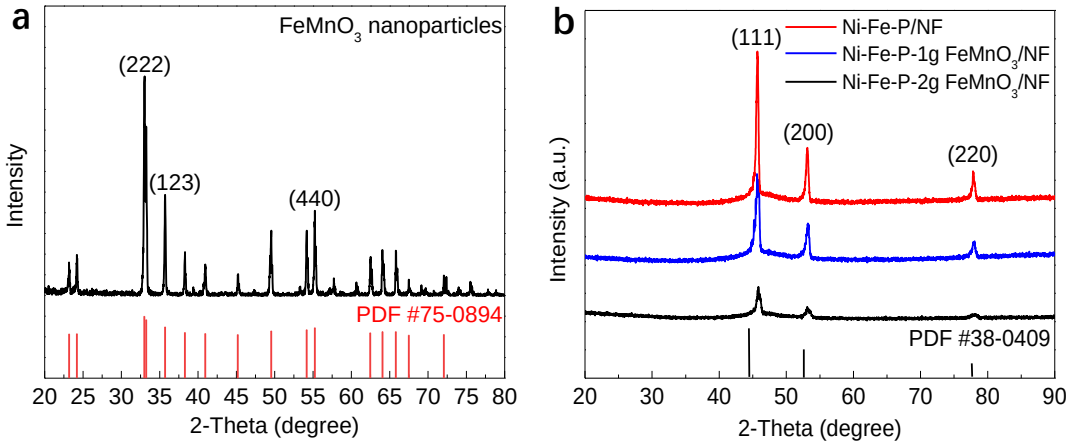

Fig. 4-3 XRD patterns of (a) $FeMnO_3$ nanoparticles, (b) Ni-Fe-P/NF and Ni-Fe-P-$FeMnO_3$/NF.

4.3.2 XPS characterization of Ni-Fe-P-$FeMnO_3$/NF

The compositions and the chemical states of nickel, iron, phosphorus and manganese on Ni-Fe-P-$FeMnO_3$/NF were further determined by XPS. From Ni 2p spectrum (Fig.4a), two obvious peaks at about 874.2 eV and 856.3 eV can be satellite peaks at 880.5 eV and 861.8 eV, [46, 47] respectively. The peaks located at 870.3 eV and 853.0 eV belong to Ni^{2+} of Ni-P bond.[46, 48] The Fe 2p spectrum (Fig. 4b) presents a peak at 713.0 eV, which corresponds to the Fe species existing in the iron phosphate.[49] The peak detected at 724.0 eV is attributed to Fe $2p_{1/2}$, which belongs to Fe^{2+} that confirms the existence of Fe^{2+} in the $FeMnO_3$.[42] As displayed in Fig. 4c, a clear peak at 133.3 eV belongs to oxidized phosphate species, due to the surface passivation.[50, 51] The other peak at 129.8 eV can be assigned to $P^{\delta-}$ in the form of metal phosphide.[50] Fig. 4d shows the Mn 2p spectrum, the peak of Mn 2p3/2 centered at 642.0 eV is observed, indicating that the Mn element in the prepared

sample is present in the chemical state of Mn^{4+}, which further confirms the existence of $FeMnO_3$.[42]

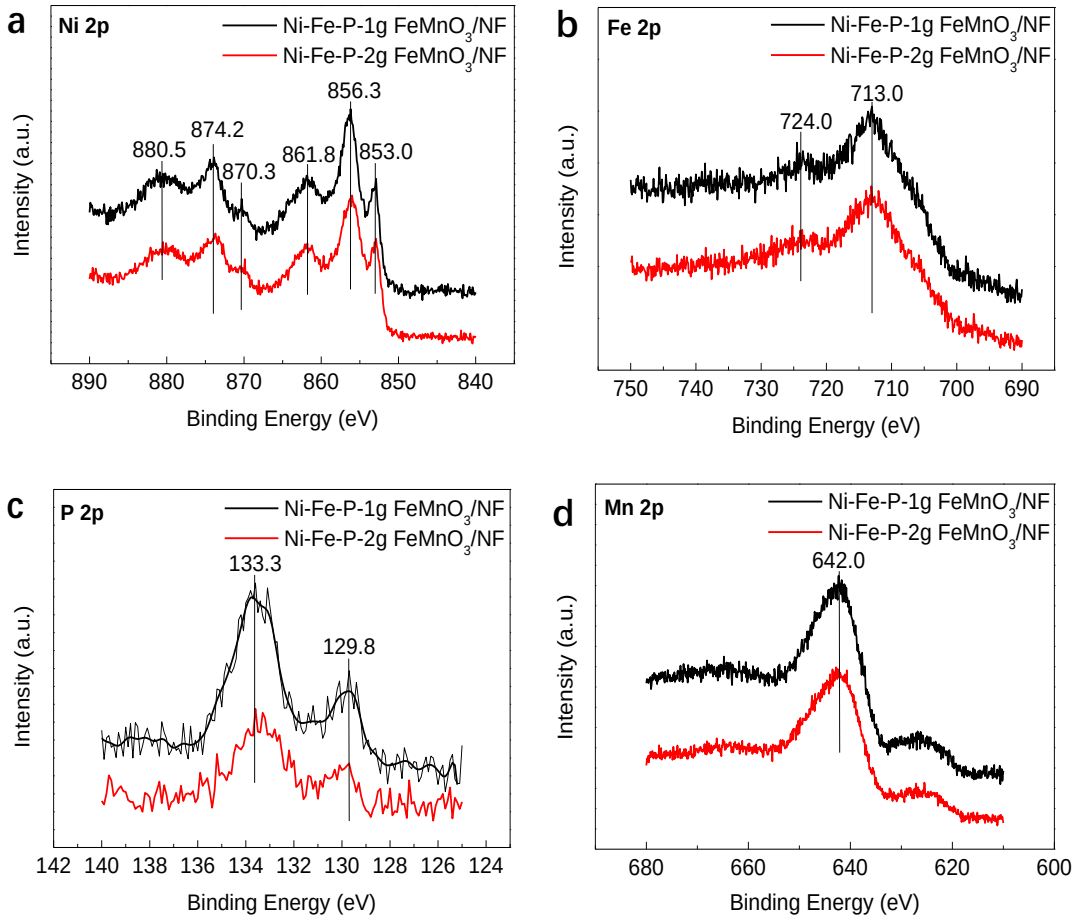

Fig. 4-4 XPS spectra of (a) Ni 2p, (b) Fe 2p, (c) P 2p and (d) Mn 2p for Ni-Fe-P-$FeMnO_3$/NF.

4.3.3 Electrocatalytic performance of Ni-Fe-P-$FeMnO_3$/NF

The electrocatalytic activity towards HER was examined by polarization curves at 1 mV s^{-1} sweep rate in 1 M KOH electrolyte. According to Fig. 5a, the Ni-Fe-P-$FeMnO_3$/NF electrocatalyst presents much higher electrocatalytic activity for HER than that of Ni-Fe-P/NF, indicating that the addition of $FeMnO_3$ dominates its electrocatalytic performance. Compared to the Ni-Fe-P/NF and Pt/C/NF catalyst in Fig. 5a, the Ni-Fe-P-2g $FeMnO_3$/NF presents a better HER performance than that of Pt/C/NF (16.9 mV), which requires only 16.62 mV (with iR compensation) overpotential to reach -10 mA cm^{-2} current density. However, Pt/C/NF shows a

remarkable HER performance after -20 mA cm^{-2}, which means our samples need to be improved at high current density in the future. On the other hand, Ni-Fe-P-1g $FeMnO_3$/NF, Ni-Fe-P-3g $MnFeO_3$, and Ni-Fe-P/NF electrode needs the overpotential of 28.87 mV, 32.13 mV, and 69.91 mV at the same current density, respectively. When the amount of $FeMnO_3$ nanoparticles exceeds 2 g in 200 mL electroless solution, the HER performance of the obtained electrocatalyst decreases gradually. In order to evaluate the reaction kinetics of the as-prepared electrode, the EIS measurements were performed in 1 M KOH solution and at a constant potential of -1.0268 V vs. RHE under the frequency range from 10^5 Hz to 0.01 Hz at an AC voltage of 5 mV. The semicircles in high- and low- frequency range of the Nyquist plots are ascribed to the charge transfer resistance and solution resistance.[27] As shown in Fig. 5b, in contrast with Ni-Fe-P/NF, Ni-Fe-P-1g $FeMnO_3$ and Ni-Fe-P-3g $FeMnO_3$, the Ni-Fe-P-2g $FeMnO_3$ presents the smallest charge transfer resistance, indicating that the appropriate $FeMnO_3$ content could improve the charge-transfer capability of the electrode and therefore provide with better HER electrocatalytic performance. Furthermore, the HER reaction kinetics of the electrocatalyst is evaluated by the corresponding Tafel slopes (Fig. 5c). The Tafel slope of the Ni-Fe-P-$FeMnO_3$/NF is only 27.87 and 26.87 mV dec^{-1} lower than that of Ni-Fe-P/NF (45.07 mV dec-1), indicating the superior rapid HER kinetic activities on the Ni-Fe-P-$FeMnO_3$/NF electrode. Fig 5d displays the long-term durability test of the Ni-Fe-P-2g $FeMnO_3$/NF under the -10 mA cm^{-2} constant current density. It can be seen that the potential decreases hardly after 45000 s test in alkaline electrolyte, indicating that Ni-Fe-P-$FeMnO_3$/NF has superior HER durability. Fig. 5e shows the HER performance of the Ni-Fe-P-2g $FeMnO_3$/NF under the dealloying time of 20, 30 and 40 seconds. Compare with different dea lloying time, the Ni-Fe-P-2g $FeMnO_3$/NF after 30 seconds fast dealloying shows the best HER performance, illustrating the appropriate atomic ratio of Ni and Fe could improve the HER performance.

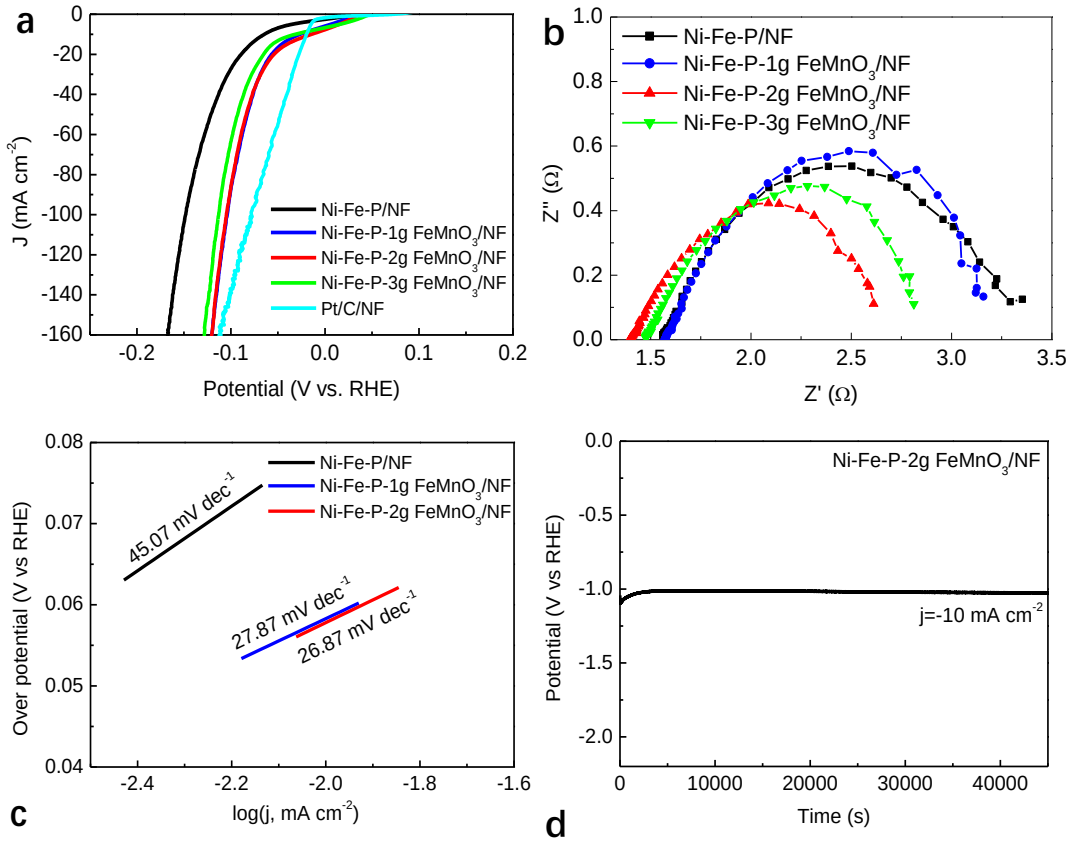

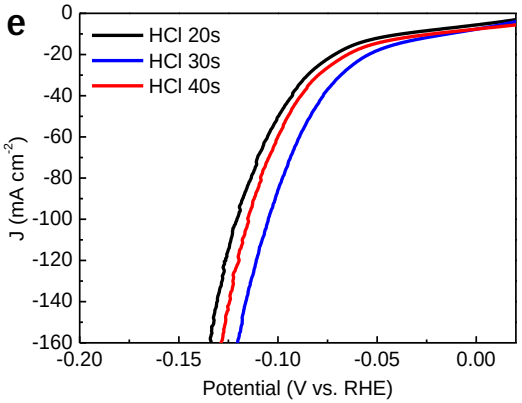

Fig. 4-5 (a) IR-corrected polarization curves of the Ni-Fe-P/NF, Ni-Fe-P-$FeMnO_3$/NF and Pt/C catalytic electrode towards HER, (b) Electrochemical impedance spectra, and (c) corresponding Taffel plots of the Ni-Fe-P/NF and Ni-Fe-P-$FeMnO_3$/NF. (d) The long-term durability test of the Ni-Fe-P-2g $FeMnO_3$/NF at -10mA cm^{-2} recorded for over 45000 s. (e)

IR-corrected polarization curves of the Ni-Fe-P-2g $FeMnO_3$/NF after different fast dealloying time.

The OER electrocatalytic activity was evaluated by polarization curves at 5 mV s^{-1} sweep rate. According to Fig 6a, the Ni-Fe-P-2g $FeMnO_3$/NF, Ni-Fe-P/NF and IrO_2/NF electrodes generate current density of 10 mA cm^{-2} at 1.449 V and 1.526 V (vs. RHE with iR compensation), respectively, and the corresponding overpotential is 219 mV and 296 mV, which is much lower than that of the IrO_2/NF catalyst (286 mV). Moreover, the Ni-Fe-P-2g $FeMnO_3$/NF exhibits a quite low overpotential of 297 mV at 50 mA cm^{-2}, which is much lower than that of Ni-Fe-P/NF (343 mV) and IrO_2/NF (363 mV). Fig. 6b gives the OER chronopotentiometric curve of Ni-Fe-P-2g $FeMnO_3$/NF at 10mA cm^{-2}. The electrocatalyst maintains in a remarkable to analyze its overall water splitting activity, the Ni-Fe-P-2g $FeMnO_3$/NF electrode was used as both cathode and anode to perform the activity test for its overall water splitting in alkaline electrolyte. For comparison, the Pt/C/NF and IrO_2/NF catalyst was used as cathode and anode respectively for the overall water splitting test. The Ni-Fe-P-2g $FeMnO_3$/NF and Pt/C/NF-IrO_2/NF electrode exhibits overpotential of 1.63 V and 1.56 V (vs. RHE with iR compensation) at 10 mA cm^{-2}, as shown in Fig 6c.

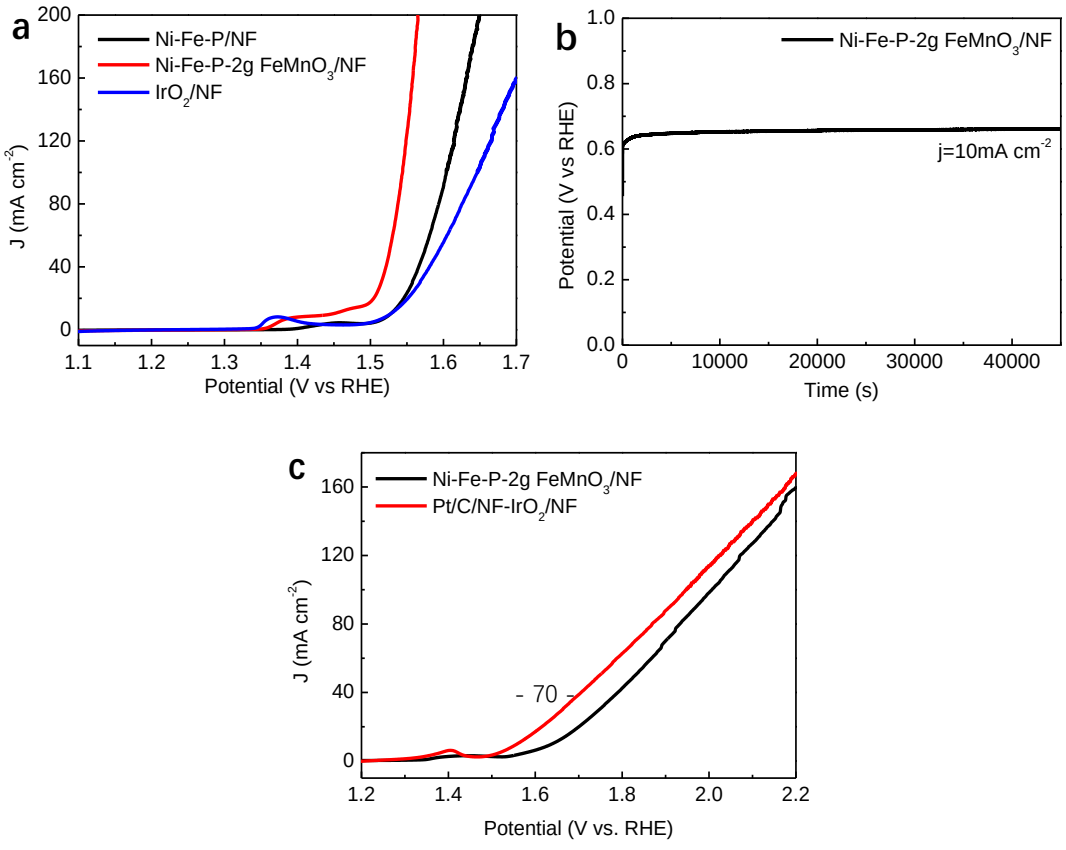

Fig. 4-6 (a) IR-corrected polarization curves of the Ni-Fe-P/NF and Ni-Fe-P-$FeMnO_3$/NF towards OER. (b) The long-term durability test of the Ni-Fe-P-2g $FeMnO_3$/NF at 10mA cm^{-2} recorded for over 45000 s. (c) Polarization curve of the Ni-Fe-P-2g $FeMnO_3$/NF for overall water splitting.

4.4 Possible mechanism of this system

Fig. 4-7 shows the mechanism of Ni-Fe-P-$FeMnO_3$/NF electrocatalyst for overall water splitting. The good performance of Ni-Fe-P-$FeMnO_3$/NF catalysts may be attributed to the following factors: (1) The EIS results shown in Fig. 4b reveal that the charge-transfer resistance of Ni-Fe-P-2g$FeMnO_3$/NF, was smaller than that of Ni-Fe-P, corresponding to a faster electron transfer and more facile HER kinetics at the electrode/electrolyte interface. (2) The flexible structure of perovskite oxide that can provide disorder-free channels of oxygen vacancies to improve the oxygen ions mobility. (3) The nano-perovskite particles are dispersed in the Ni-Fe-P matrix, which generates lots of lattice defects, thereby increasing the active sites. (4) The high catalytic performance of this system is also caused by the lattice defects produced by dealloying and the multivalent state of Mn element.

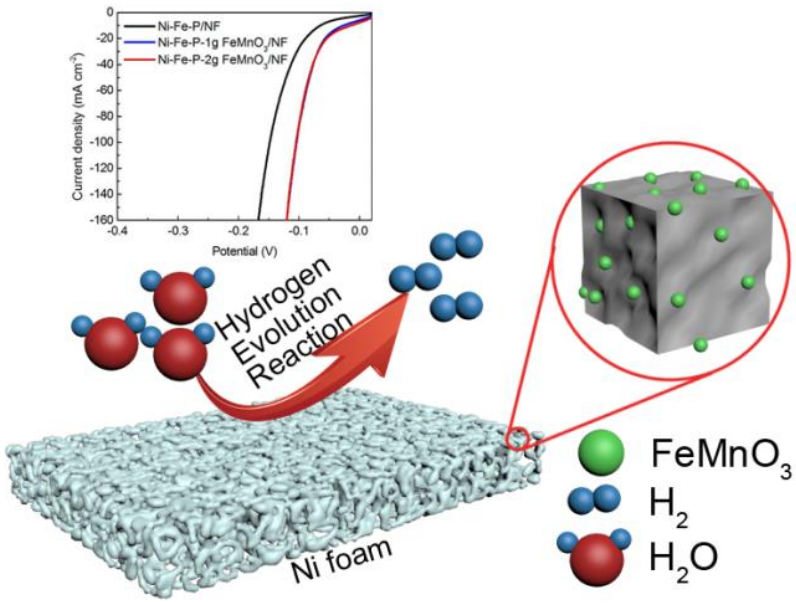

Fig. 4-7 Schematic illustration of the mechanism of Ni-Fe-P-$FeMnO_3$/NF electrocatalyst for overall water splitting.

4.5 Conclusion

In summarize, we have successfully fabricated a nanocomposite electrocatalyst Ni-Fe-P-$FeMnO_3$ on Ni foam with excellent electrocatalytic activity towards HER via simple methods of electroless plating and rapid dealloying. Since the assistant of the Ni foam substrate and synergistic effect of Ni-Fe-P, especially the addition of $FeMnO_3$, the Ni-Fe-P-$FeMnO_3$/NF achieves remarkable electrocatalytic performance of 16.62 mV at the current density of -10 mA cm^{-2} for HER, which is better than that of Pt/C noble metal catalyst. Moreover, the Ni-Fe-P-$FeMnO_3$/NF has remarkable OER activity as well, which requires only 297 mV and 219 mV of overpotential at 50 mA cm^{-2} and 10 mA cm^{-2}, respectively. It is worth mentioning that the OER performance of 10 mA cm^{-2} and 50 mA cm^{-2} is much lower than that of IrO_2 noble metal catalyst. Evidently, the overall water splitting activity of the Ni-Fe-P-$FeMnO_3$/NF electrode used as both cathode and anode performs a quite low potential of 1.63 V (vs. RHE) to reach 10 mA cm^{-2}. The outstanding electrocatalytic activity and long-term durability of the Ni-Fe-P-$FeMnO_3$/NF electrode make it become a promising electrode material for overall water splitting application.

4.6 Reference

[1] Z. W. Seh, J. Kibsgaard, C. F. Dickens, I. Chorkendorff, J. K. Nørskov, T. F. Jaramillo, Combining theory and experiment in electrocatalysis: Insight into materials design. Science 355 (2017) 4998-5003.

[2] Y. Liang, Y. Li, H. Wang, H. Dai, Strongly coupled inorganic/nanocarbon hybrid

materials for advanced electrocatalysis. J. Am. Chem. Soc. 135 (2013) 2013-2036.

[3] D. Strmcnik, P. P. Lopes, B. Genorio, V. R. Stamenkovic, N. M. Markovic, Design principles for hydrogen evolution reaction catalyst materials. Nano Energy 29 (2016) 29-36.

[4] W. Zhou, D.-D. Huang, Y.-P. Wu, J. Zhao, T. Wu, J. Zhang, D.-S. Li, C. Sun, P. Feng, X. Bu, Stable hierarchical bimetal-organic nanostructures as high performance electrocatalysts for the oxygen evolution reaction. Angew. Chem. Int. Ed. 58 (2019) 4227-4231.

[5] J. Greeley, T. F. Jaramillo, J. Bonde, I. B. Chorkendorff, J. K. Nørskov, Computational high-throughput screening of electrocatalytic materials for hydrogen evolution. Nat. Mater. 5 (2006) 909-913.

[6] N. M. Marković, B. N. Grgur, P. N. Ross, Temperature-dependent hydrogen electrochemistry on platinum low-index single-crystal surfaces in acid solutions. J. Phys. Chem. B 101 (1997) 5405-5413.

[7] W. Sheng, H. A. Gasteiger, Y. Shao-Hom, J. Hydrogen oxidation and evolution reaction kinetics on platinum: acid vs alkaline electrolytes. Electrochem. Soc. 157 (2010) B1529-B1536.

[8] Y. Lee, J. Suntivich, K. J. May, E. E. Perry, Y. Shao-Horn, Synthesis and activities of rutile IrO_2 and RuO_2 nanoparticles for oxygen evolution in acid and alkaline solutions. J. Phys. Chem. Lett. 3 (2012) 399-404.

[9] P. Xiao, M. A. Sk, L. Thia, X. Ge, R. J. Lim, J.-Y. Wang, K. H. Lim, X. Wang, Molybdenum phosphide as an efficient electrocatalyst for the hydrogen evolution reaction. Energy Environ. Sci. 7 (2014) 2624-2629.

[10] E. J. Popczun, J. R. McKone, C. G. Read, A. J. Biacchi, A. M. Wiltrout, N. S. Lewis, R. E. Schaak, Nanostructured nickel phosphide as an electrocatalyst for the hydrogen evolution reaction. J. Am. Chem. Soc. 135 (2013) 9267-9270.

[11] E. J. Popczun, C. G. Read, C. W. Roske, N. S. Lewis, R. E. Schaak, Highly active electrocatalysis of the hydrogen evolution reaction by cobalt phosphide nanoparticles.

Angew. Chem. Int. Ed. 53(2014) 5427-5430.

[12] H. B. Wu, B. Y. Xia, L. Yu, X.-Y. Yu, X. W. D. Lou, Porous molybdenum carbide nano-octahedrons synthesized via confined carburization in metal-organic frameworks for efficient hydrogen production. Nat. Commun. 6 (2015) 6512.

[13] W.-F. Chen, C.-H. Wang, K. Sasaki, N. Marinkovic, W. Xu, J, T, Muckerman, Y. Zhu, R. R. Adzic, Highly active and durable nanostructured molybdenum carbide electrocatalysts for hydrogen production. Energy Environ. Sci. 6 (2013) 943-951.

[14] A. V. Nikiforov, I. M. Petrushina, E. Christensen, N. V. Alexeev, A. V. Samokhin, N. J. Bjerrum, WC as non-platinum hydrogen evolution electrocatalyst for high temperature PEM water electrolysers. Int. J. Hydrog. Energy 37 (2012) 18591-18597.

[15] J.-X. Feng, H. Xu, S.-H. Ye, G. Ouyang, Y.-X. Tong, G.-R. Li, Silica-polypyrrole hybrids as high-performance metal-free electrocatalysts for the hydrogen evolution reaction in neutral media. Angew. Chem. Int. Ed. 56(2017) 8120-8124.

[16] M. Gong, W. Zhou, M.-C. Tsai, J. Zhou, M. Guan, M.-C. Lin, B. Zhang, Y. Hu, D.-Y. Wang, J. Yang, S. J. Pennycook, B.-J. Hwang, H. Dai, Nanoscale nickel oxide/nickel heterostructures for active hydrogen evolution electrocatalysis. Nat. Commun. 5 (2014) 4695.

[17] N. Danilovic, R. Subbaraman, D. Strmcnik, K.-C. Chang, A. P. Paulikas, V. R. Stamenkovic, N. M. Markovic, Enhancing the alkaline hydrogen evolution reaction activity through the bifunctionality of $Ni(OH)_2$/metal catalysts. Angew. Chem. Int. Ed. 51 (2012) 12495-12498.

[18] R. Subbaraman, D. Tripkovic, K.-C. Chang, D. Strmcnik, A. P. Paulikas, P. Hirunsit, M. Chan, J. Greeley, V. Stamenkovic, N. M. Markovic, Trends in activity for the water electrolyser reactions on 3d M (Ni, Co, Fe, Mn) hydr(oxy)oxide catalysts. Nat. Mater. 11 (2012) 550-557.

[19] A. B. Laursen, S. Kegnæs, S. Dahl, I. Chorkendorff, Molybdenum sulphides-efficient and viable materials for electro- and photoelectrocatalytic hydrogen evolution. Energy environ. Sci. 5 (2012) 5577-5591.

[20] D. Voiry, H. Yamaguchi, J. Li, R. Silva, D. C. B. Alves, T. Fujita, M. Chen, T. Asefa, V. B. Shenoy, G. Eda, M. Chhowalla, Enhanced catalytic activity in strained chemically exfoliated WS_2 nanosheets for hydrogen evolution. Nat. Mater. 12 (2013) 850-855.

[21] L. Birry, A. Lasia, Studies of the hydrogen evolution reaction on raney nickel-molybdenum electrodes. J. Appl. Electrochem. 34 (2004) 735-749.

[22] J. R. McKone, B. F. Sadtler, C. A. Werlang, N. S. Lewis, H. B. Gray, Ni-Mo nanopowders for efficient electrochemical hydrogen evolution. ACS Catal. 3 (2013) 166-169.

[23] C. Lupi, A. Dell'Era, M. Pasquali, Nickel-cobalt electrodeposited alloys for hydrogen evolution in alkaline media. Int. J. Hydrog. Energy 34 (2009) 2101-2106.

[24] E. Hu, Y. Feng, J. Nai, D. Zhao, Y. Hu, X. W. D. Lou, Construction of hierarchical Ni-Co-P hollow nanobricks with oriented nanosheets for efficient overall water splitting. Energy Environ. Sci. 11 (2018) 872-880.

[25] K. Xu, P. Chen, X. Li, Y. Tong, H. Ding, X. Wu, W. Chu, Z. Peng, C. Wu, Y. Xie, Metallic nickel nitride nanosheets realizing enhanced electrochemical water oxidation. J. Am. Chem. Soc. 137 (2015) 4119-4125.

[26] C. Tang, N. Cheng, Z. Pu, W. Xing, X. Sun, NiSe nanowire film supported on nickel foam: An efficient and stable 3D bifunctional electrode for full water splitting. Angew. Chem. Int. Ed. 54 (2015) 9351-9355.

[27] K. Sun, K. Wang, T. Yu, X. Liu, G. Wang, L. Jiang, Y. Bu, G. Xie, High-performance Fe-Co-P alloy catalysts by electroless deposition for overall water splitting. Int. J. Hydrog. Energy 44 (2019) 1328-1335.

[28] Y. Li, H. Zhang, M. Jiang, Q. Zhang, P. He, X. Sun, 3D self-supported Fe-doped Ni_2P nanosheet arrays as bifunctional catalysts for overall water splitting. Adv. Funct. Mater. 27 (2017) 1702513.

[29] K. Wang, K. Sun, T. Yu, X. Liu, G. Wang, L. Jiang, G. Xie, Facile synthesis of nanoporous Ni-Fe-P bifunctional catalysts with high performance for overall water

splitting. J. Mater. Chem. A 7 (2019) 2518-2523.

[30] S. H. Ahn, A. Manthiram, Direct growth of ternary Ni-Fe-P porous nanorods onto nickel foam as a highly active, robust bi-functional electrocatalyst for water splitting. J. Mater. Chem. A 5 (2017) 2496-2503.

[31] J. Luo, J.-H. Im, M. T. Mayer, M. Schreier, M. K. Nazeeruddin, N.-G. Park, S. D. Tilley, H. J. Fan, M. Grätzel, Water photolysis at 12.3% efficiency via perovskite photovoltaics and earth-abundant catalysts. Science 345 (2014) 1593-1596.

[32] C. G. Read, J. F. Callejas, C. F. Holder, R. E. Schaak, General strategy for the synthesis of transition metal phosphide films for electrocatalytic hydrogen and oxygen evolution. ACS Appl. Mater. Interfaces 8 (2016) 12798-12803.

[33] G. Valderrama, M. R. Goldwasser, C. U. Navarro, J. M. Tatibouët, J. Barrault, C. Batiot-Dupeyrat, F. Martínez, Dry reforming of methane over Ni perovskite type oxides. Catal. Today 107-108 (2005) 785-791.

[34] M. R. Goldwasser, M. E. Rivas, E. Pietri, M. J. Pérez-Zurita, M. L. Cubeiro, A. Grivobal-Constant, G. Leclercq, Perovskites as catalysts precursors: synthesis and characterization. J. Mol. Catal. A: Chem. 228 (2005) 325-331.

[35] A. Galal, N. F. Atta, S. M. Ali, Investigation of the catalytic activity of $LaBO_3$ (B = Ni, Co, Fe or Mn) prepared by the microwave-assisted method for hydrogen evolution in acidic medium. Electrochim. Acta 56 (2011) 5722-5730.

[36] C. Jin, X. Cao, L. Zhang, C. Zhang, R. Yang, Preparation and electrochemical properties of urchin-like $La_{0.8}Sr_{0.2}MnO_3$ perovskite oxide as a bifunctional catalyst for oxygen reduction and oxygen evolution reaction. J. Power Sources 241 (2013) 225-230.

[37] Y. Da, L. Zeng, C. Wang, C. Gong, L. Cui, A simple approach to tailor OER activity of $Sr_xCo_{0.8}Fe_{0.2}O_3$ perovskite catalysts. Electrochim. Acta 300 (2019) 85-92.

[38] Y. Wang, Z. Wang, C. Jin, C. Li, X. Li, Y. Li, R. Yang, M. Liu, Enhanced overall water electrolysis on a bifunctional perovskite oxide through interfacial engineering. Electrochim. Acta 318 (2019) 120-129.

[39] Z. Wang, C. Jin, J. Sui, C. Li, R, Yang, Phosphorus-doped $SrCo_{0.5}Mo_{0.5}O_3$ perovskites with enhanced bifunctional oxygen catalytic. Int. J. Hydrog. Energy 43 (2018) 20727-20733.

[40] X. Xu, Y. Chen, W. Zhou, Z. Zhu, C. Su, M. Liu, Z. Shao, A perovskite electrocatalyst for efficient hydrogen evolution reaction. Adv. Mater. 28 (2016) 6442-6448.

[41] H. Bin, Z. Yao, S. Zhu, C. Zhu, H. Pan, Z. Chen, C. Wolverton, D. Zhang, A high-performance anode material based on $FeMnO_3$/graphene composite. J. Alloy. Comp. 695 (2017) 1223-1230.

[42] M. Li, W. Xu, W. Wang, Y. Liu, B. Cui, X. Guo, Facile synthesis of specific $FeMnO_3$ hollow sphere/graphene composites and their superior electrochemical energy storage performances for supercapacitor. J. Power Sources 248 (2014) 465-473.

[43] L. Yang, Z. Guo, J. Huang, Y. Xi, R. Gao, G. Su, W. Wang, L. Cao, B. Dong, Vertical growth of 2D amorphous $FePO_4$ nanosheet on Ni foam: outer and inner structural design for superior water splitting. Adv. Mater. 29 (2017) 1704574.

[44] C. G. Morales-Guio, X. Hu, Amorphous molybdenum sulphides as hydrogen evolution catalysts. Acc. Chem. Res. 47 (2014) 2671-2681.

[45] U. Y. Qazi, C.-Z. Yuan, N. Ullah, Y.-F. Jiang, M. Imran, A. Zeb, S.-J. Zhao, R. Javaid, A.-W. Xu, One-step growth of iron-nickel bimetallic nanoparticles on FeNi alloy foils: Highly efficient advanced electrodes for the oxygen evolution reaction. ACS Appl. Mater. Interfaces 9 (2017) 28627-28634.

[46] C. Xuan, J. Wang, W. Xia, Z. Peng, Z. Wu, W. Lei, K. Xia, H. L. Xin, D. Wang, Porous structured Ni-Fe-P nanocubes derived from a Prussian blue analogue as an electrocatalyst for efficient overall water splitting. ACS Appl. Mater. Interfaces 9 (2017) 26134-26142.

[47] Y. Pan, Y. Liu, J. Zhao, K. Yang, J. Liang, D. Liu, W. Hu, D. Liu, Y. Liu, C. Liu, Monodispersed nickel phosphide nanocrystals with different phases: synthesis,

characterization and electrocatalytic properties for hydrogen evolution. J. Mater. Chem. A 2015, 3, 1656-1665.

[48] C. Xuan, Z. Peng, K. Xia, J. Wang, W. Xiao, W. Lei, M. Gong, T. Huang, D. Wang, Self-supported ternary Ni-Fe-P nanosheets derived from metal-organic frameworks as efficient overall water splitting electrocatalysts. Electrochimica Acta 258 (2017) 423-432.

[49] Y. Feng, Y. OuYang, L. Peng, H. Qiu, H. Wang, Y. Wang, Quasi-graphene-envelope Fe-doped Ni_2P sandwiched nanocomposites for enhanced water splitting and lithium storage performance. J. Mater. Chem. A 3 (2015) 9587-9594.

[50] Y. Y. Tong, C. D. Gu, J. L. Zhang, M. L. Huang, H. Tang, X. L. Wang, J. P. Tu, Three-dimensional astrocyte-network Ni-P-O compound with superior electrocatalytic activity and stability for methanol oxidation in alkaline environments. J. Mater. Chem. A 3 (2015) 4669-4678.

[51] Z. Zhang, S. Liu, J. Xiao, S. Wang, Fiber-based multifunctional nickel phosphide electrodes for flexible energy conversion and storage. J. Mater. Chem. A 4 (2016) 9691-9699.

Chapter 5: Conclusions and future works

5.1 Conclusions and summary

Photoelectrochemical (PEC) and electrochemical water splitting for hydrogen evolution are potential methods for energy shortage and environment pollution. In this thesis, a CuO_x/WO_3 thin-film based on p-n heterojunction proposed as a highly performance and stable photocathode. The CuO_x/WO_3 thin-film was deposited by magnetron reactive sputtering layer by layer, followed with slow rate annealing in O_2 ambient. This is an excellent method for high-quality and uniform composite thin-film deposition with large areas at a high growth rate. The optimized CuO_x/WO_3 thin-film photocathode after slow rate annealing at 500 °C in O_2 provides an obviously enhanced photoinduced current density of -3.8 mA cm^{-2} at a bias potential of -0.5 V (vs. Ag/AgCl), which value is 1.5 times higher than that of bared CuO_x thin-film. This highly enhanced photoelectrochemical performance is attributed to p-n heterojunction, which accelerates the photogenerated electrons and holes transfer to n-WO_3 and p-CuO_x, thereby accelerate the separation of photogenerated carries. In addition, WO_3 layer covered on the surface of CuO_x thin film can improve the stability of Cu_2O in electrolytes.

In order to solve the problem of strong light illumination required for PEC water splitting, a new type of highly active and cost-effective nanocomposite electrocatalyst Ni-Fe-P-$FeMnO_3$ on nickel foam (NF) supports is designed and prepared by electroless composite deposition and rapid dealloying. The nanocomposite electrocatalyst Ni-Fe-P-$FeMnO_3$/NF presents a more remarkable electrocatalytic performance than Pt/Pd noble metal catalysts towards hydrogen evolution reaction (HER), which demands a quite low overpotential of 16.62 mV at -10 mA cm^{-2} current density in 1 M KOH. The prepared Ni-Fe-P-$FeMnO_3$/NF electrocatalyst exhibits remarkable oxygen evolution reaction (OER) activity as well, which requires only 297

mV and 219 mV of overpotential at 50 mA cm^{-2} and 10 mA cm^{-2} current density, respectively. Moreover, the overall water splitting activity of Ni-Fe-P-$FeMnO_3$/NF as both anode and cathode achieves a low potential of 1.63 V (vs. RHE) at a current density of 10 mA cm^{-2}.

5.2 Suggestion for future works

As shown in chapter 3, the PEC performance of copper oxide photocathode was improved greatly after the p-n heterojunction was fabricated. However, to date, we have not realized PEC overall water splitting without any extra bias potential. Thus, in this application, we plan to utilize the all-solid Z-scheme principle to fabricate a FTO/metal oxide A/metal/metal oxide B PEC water splitting photocathode. If compound two kinds of metal oxide (take CuO and Cu_2O as an example), furthermore, find out a suitable composition method, to fabricate a Z-scheme (the working mechanism of Z-scheme photocatalyst shows in Fig. 5-1) photogenerated carriers transfer effect between the CuO and Cu_2O, inducing the photogenerated electrons of CuO to recombine with the photogenerated holes of Cu_2O, that provide an possible strategy to fabricate a PEC over all water splitting device.

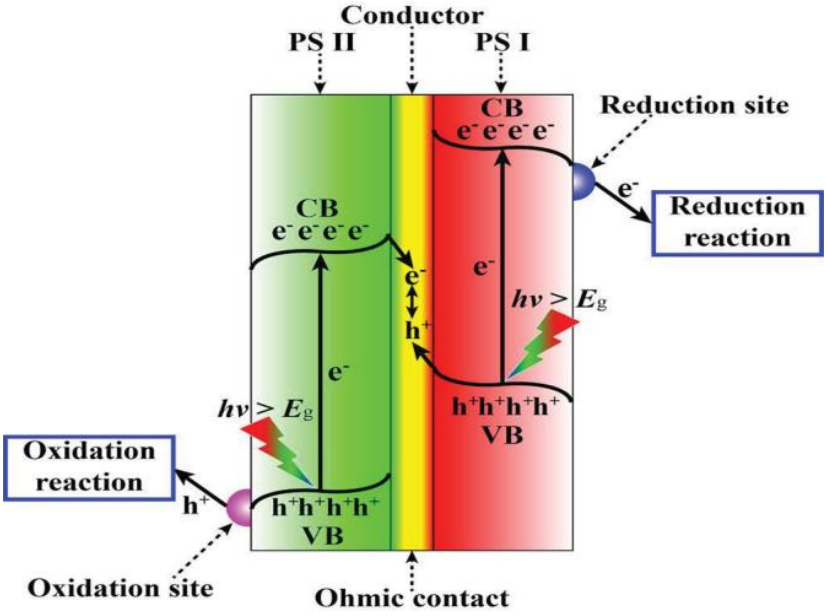

Fig. 5-1 Operation mechanism of all solid Z-scheme photocatalyst.

In this thesis, chapter 4, a high active electrocatalyst Ni-Fe-P-$FeMnO_3$/NF has been developed for overall water splitting. However, from the HER polarization curve, we can observe that the HER performance of Ni-Fe-P-$FeMnO_3$/NF is still worse than that of noble metal Pt/C. Thus, we will explore materials with better HER performance than perovskite to optimize the Ni-Fe-P/NF system.

Acknowledgements

On the completion of my thesis, I would like to express my gratitude to all those who have helped and supported me in completing the academic life.

First and foremost, I would like to express my sincere gratitude to my supervisor, Professor Jin-Ping Ao, for his invaluable guidance and encouragement extended throughout the study. He is respectable, responsible and resourceful scholar, who has provided me with valuable guidance in every stage of writing this thesis. Without his enlightening instruction, impressive kindness and patience, I could not have completed my thesis.

I would like to express my sincere gratitude to my father, Guangwen Xie, for his instructive suggestion and patient guidance assisted complete the thesis. His keen and vigorous academic observation enlightens me not only in this thesis but also in my future study.

Many thanks extend to the students Yuyu Bu, Taofei Pu, Lei Wang, Tong Zhang, Ruiling Wang, Yang Li, Taiki Hoshi, Shunsuke Nakao, Daiki Sengo, Yuuto Morishita, Masataka Tsuda, Kazuki Aoki, in Ao group, for their help and patience in my research and life.

I would like to gratefully acknowledge Department of Electrical and Electronic Engineering, Faculty of Engineering, Tokushima University for providing the resources and needs during the thesis. I would like to extend my appreciation to Technician Takahiro Kitajima and Technician Azuma Chiri for their unconditional help during this research.

Last and certainly not the least, I am forever indebted to my parents, who have been supporting me through all of the accomplishments of my academic life. Their indefinite love has made the things different in every aspect of my life.

Publication list

Scientific papers

[1] **Tian Xie**, Tao Zheng, Ruiling Wang, Taofei Pu, Xiaobo Li, Yuyu Bu, Jin-Ping Ao, A promising CuO_x/WO_3 p-n heterojunction thin-film photocathode fabricated by magnetron reactive sputtering. Int. J. Hydrog. Energy 44 (2019) 4062-4071.

[2] **Tian Xie**, Tao Zheng, Ruiling Wang, Yuyu Bu, Jin-Ping Ao, Fabrication of CuO_x thin-film photocathodes by magnetron reactive sputtering for photoelectrochemical water reduction. Green Energy & Environment 3 (2018) 239-246.

[3] **Tian Xie**, Tao Zheng, Jin-Ping Ao, Synthesis of copper oxide by reactive magnetron sputtering for photoelectrochemical water splitting. Advances in Engineering Research 170 (2018) 1055-1061.

[4] **Tian Xie**, Zunhang Lv, Tao Zheng, Kaihang Wang, Taofei Pu, Guangwen Xie, Luhua Jiang, Jin-Ping Ao, Perovskite nanoparticles promoted electrocatalysts Ni-Fe-P-$FeMnO_3$/NF for overall water splitting. Small, under review.

[5] Ruiling Wang, **Tian Xie**, Tong Zhang, Taofei Pu, Yuyu Bu, Jin-Ping Ao, Fabrication of FTO-$BiVO_4$-W-WO_3 photoanode for photoelectrochemical performance improving: based on the Z-scheme electron transfer mechanism. J. Mater. Chem. A 6 (2018) 12956-12961.

[6] Ruiling Wang, **Tian Xie**, Zhiyong Sun, Taofei Pu, Weibing Li, Jin-Ping Ao, Graphene quantum dot modified g-C_3N_4 for enhanced photocatalytic oxidation of ammonia performance. RSC Adv. 7 (2017) 51687-51694.

[7] Yuyu Bu, Zhiwei Chen, **Tian Xie**, Weibing Li, Jin-Ping Ao, Fabrication of C_3N_4 ultrathin flakes by mechanical grind method with enhanced photocatalysis and photoelectrochemical performance. RSC Adv. 6, (2016) 47813-47819.

[8] Lei Wang, Liuan Li, **Tian Xie**, Xinzhi Wang, Xinke Liu, Jin-Ping Ao, Threshold voltage tuning in AlGaN/GaN HFETs with p-type Cu_2O gate synthesized by magnetron reactive sputtering. Appl. Surf. Sci. 437 (2017) 98-102.

[9] Tong Zhang, Taofei Pu, **Tian Xie**, Liuan Li, Yuyu Bu, Xiao Wang, Jin-Ping Ao, Synthesis of thermally stable HfO_xN_y as gate dielectric for AlGaN/GaN heterostructure field-effect transistors. Chinese Phys. B 27 (2018) 078503.

[10] Taofei Pu, Xiaobo Li, Taowei Peng, **Tian Xie**, Liuan Li, Jin-Ping Ao, Influence of metal-insulator-semiconductor gate structure on normally-off P-GaN heterojunction field-effect transistors. J. Cryst. Growth 532 (2020) 125395.

[11] Xiaobo Li, Taofei Pu, Hoshi Taiki, Tong Zhang, **Tian Xie**, Shigeki Joseph Luke Fujiwara, Hiroshi Kitahata, Liuan Li, Sachio Kobayashi, Motoo Ito, Xianjie Li, Jin-Ping Ao, GaN Schottky barrier diodes with nickel nitride anodes sputtered at different nitrogen partial pressure. Vacuum 162 (2019) 72-77.

[12] Xiaobo Li, Taiki Hoshi, Liuan Li, Taofei Pu, Tong Zhang, **Tian Xie**, Xianjie Li, Jin-Ping Ao, GaN Schottky barrier diode with thermally stable nickel nitride electrode deposited by reactive sputtering. Mat. Sci. Semicon. Proc. 93, (2019) 1-5.

International conference presentations

[1] **Tian Xie**, Ruiling Wang, Yuyu Bu, Jin-Ping Ao, Fabrication and photoelectrochemical evaluation of Cu_xO thin film photocathodes grown by magnetron reactive sputtering. 10th International Symposium on Advanced Plasma Science and its Applications for Nitrides and Nanomaterials/11th International Conference on Plasma-Nano Technology & Science, Mar. 2018, Nagoya, Japan.

[2] **Tian Xie**, Yuyu Bu, Liang-Chiun Chao, Jin-Ping Ao, Fabrication of Cu_2O thin films by reactive magnetron sputtering for photoelectrochemical water splitting. 2nd International Forum on Advanced Technologies, Mar. 2016, Tokushima, Japan.

[3] **Tian Xie**, Tao Zheng, Jin-Ping Ao, Synthesis of copper oxide by reactive magnetron sputtering for photoelectrochemical water splitting. 2018 8th International Conference on Advanced Engineering Materials and Technology (ICAEMT 2018), Jul. 2018, Shenzhen, China.